

Towards accurate and automated detection and
quantification of localized methane point sources
on a global scale

Thesis by
Siraput Jongaramrungruang

In Partial Fulfillment of the Requirements for the
Degree of
Doctor of Philosophy

The logo for the California Institute of Technology (Caltech), featuring the word "Caltech" in a bold, orange, sans-serif font.

CALIFORNIA INSTITUTE OF TECHNOLOGY
Pasadena, California

2022
Defended July 20, 2021

© 2022

Siraput Jongaramrungruang
ORCID: 0000-0002-2477-2043

All rights reserved except where otherwise noted

To my beloved parents and mentor

ACKNOWLEDGEMENTS

There are many individuals who have encouraged and supported me along the way towards the completion of my PhD. While I may not be able to mention everyone here, I owe a debt of gratitude to all of them.

First, I count among my greatest fortunes to have Christian Frankenberg as my PhD adviser. Christian's expertise and character has deeply inspired me to grow and develop. Christian spent a lot of time helping answer questions and provided resources for me to successfully pursue my research goals. I treasure the time I got to observe and learn first-hand from Christian how one's curiosity can know no bounds. Our shared discussions and coding sessions that sometimes went into evenings are the golden memories of my PhD that I cherish. Christian, I am very grateful for your unlimited trust and support. I am determined to keep growing and support others in the same way you greatly supported me.

Second, I would like to express my appreciation to my thesis committee: Paul Wennberg, David Thompson, and Zachary Ross. Paul, thank you for providing scientific guidance and support. The opportunity to work and discuss my thesis work with you and the climate class that we pulled off together at the beginning of the pandemic was very rewarding. David, I am really thankful that you joined my thesis committee. Thank you for providing feedback and advice. Your enthusiasm and optimism regarding my research at each and every of our encounters have meant so much to me. Zach, your help and advice was integral for a key part of my research, leading up to the success of my candidacy exam and this thesis. In addition, I want to thank Simona Bordoni who advised me and provided a foundation in my first year at Caltech. Many colleagues from JPL also crucially contributed to my research, particularly Georgios Matheou, Andrew Thorpe, Brian Bue, Dan Cusworth, and Riley Duren. Thank you all so much.

Third, fellow members of the FraLab have made our group bright and enjoyable. Thank you Liyin, Newton, Rui, Philips, Yi, Yujie, Russ, Vincent, Troy, Deb, Polina, Costa, and Rupesh for the friendship and generosity we shared. Friends in the ESE program have made the PhD journey meaningful. I especially thank Zhao, Toby, Dan, Ana, Harrison, and Ho-Hsuan for all the help you have given me. My thanks also go to our staff, especially Nora and Julie for their behind-the-scene support. Thai friends at Caltech also supported me in adjusting to living here; thank you all.

During difficult times and hardships, the SGI community has been a reservoir of hope and courage. Jim, Sue, and Sunee, thank you for embracing me like your own family members. Noriko, Leo, Nobu, Sean, and Adin, thank you for your warmth and care. I vividly recall those moments when you cheerfully shared with me your experiences and encouragement throughout the past years.

Next, I would like to express my gratitude to my two dear friends with whom I share profound bonds. Mod, our choice to sit next to each other in middle school was one great turning point in my life. Thank you for being an inspiration academically and a comrade I can share sorrow and joy with. Tee, words cannot describe the path we have shared and will continue to advance along. I look forward to fulfilling our shared noble mission together with you and Mod.

Last but certainly not least, I am indebted to my parents, Nat and Duangporn, who provide love and support for me no matter the circumstances. Dad, thank you for working many long hours each day all these years to support me and mom regardless of what it does to your physical toll. I will never forget your vast heart. Mom, thank you for being so strong for our family and persevere through the past 10 years I have been abroad. I apologize for worrying you many times. This PhD is my small expression in response to the eternal belief and faith you have in me. From now, it is me who will support and protect both of you in return. Finally, I would like to express my utmost appreciation to Daisaku Ikeda whose life and philosophy has inspired me since childhood to respect my life and others and live with a great vow.

ABSTRACT

Methane (CH_4) is the second most important anthropogenic greenhouse gas with a significant impact on radiative forcing, tropospheric air quality, and stratospheric water vapor. Because methane has a much shorter lifetime compared to carbon dioxide (CO_2), reduction in methane emission is deemed a key target for climate mitigation strategies in upcoming decades. One crucial step in emission reduction is determining the location and emission rate of localized methane sources. Remote-sensing instruments using absorption spectroscopy have emerged as one promising solution for measuring atmospheric CH_4 concentration over large geographical areas. However, the identification and quantification of local point sources based on the observed methane column enhancement distribution has proven challenging due to uncertainties in the knowledge of local wind speed and retrieval errors arising from surface spectral interferences and instrument noise. In this thesis, it is shown how plume morphology based on a 2-D image of methane column enhancement can be used to quantify the source emission rate directly without relying on any ancillary data such as local wind speed measurements. Large eddies simulations (LES) are utilized to create realistic synthetic plume observations under various atmospheric conditions. Using this data, a deep learning model named MethaNet is trained to predict emission rates directly from 2-D methane plume images. The model achieves a level of performance for quantifying methane emission rates that is state-of-the-art for a method that does not rely on wind speed information. Obtaining methane column measurements with low precision error and bias is a key step for separating real plume enhancements from artefacts and enhancing the quantification performance. Here an instrument tradeoff analysis is presented to assess the effect of changing instrument specifications and retrieval parameters. It is shown how the retrieval errors can be mitigated with optimal spectral resolutions and a larger polynomial degree to approximate surface albedo variations in the retrieval process. The results in this thesis contribute towards building an enhanced monitoring system that can measure CH_4 enhancement fields and determine methane sources accurately and efficiently at scale.

PUBLISHED CONTENT AND CONTRIBUTIONS

- Jongaramrungruang, S. et al. (2021a). “MethaNet – An AI-driven approach to quantifying methane point-source emission from high-resolution 2-D plume imagery”. In: *Remote Sensing of Environment*, Under Review.
SJ and CF conceptualized and designed the research objectives. SJ performed the analysis and wrote the paper. GM ran the LES model and provided output. AT provided the AVIRIS-NG datasets. CF provided guidance on the overall design and support on scientific approaches and experimental setups. All co-authors contributed to the writing of the paper.
- Jongaramrungruang, S. et al. (2021b). “Remote sensing of methane plumes: instrument tradeoff analysis for detecting and quantifying local sources at global scale”. In: *Atmospheric Measurement Techniques*, Under Review.
SJ and CF conceptualized and designed the research objectives. SJ performed the analysis and wrote the paper. GM ran the LES model and provided output. AT provided the AVIRIS-NG datasets. CF provided guidance on the overall design and support on scientific approaches and experimental setups. All co-authors contributed to the writing of the paper.
- Jongaramrungruang, S. et al. (2019). “Towards accurate methane point-source quantification from high-resolution 2-D plume imagery”. In: *Atmospheric Measurement Techniques* 12.12. ISSN: 18678548. DOI: 10.5194/amt-12-6667-2019.
SJ and CF conceptualized and designed the research objectives. SJ performed the analysis, and wrote the paper. GM ran the LES model, and provided output. GM ran the LES model, provided output and guided the analysis. AT, RD, EK, and DT provided the AVIRIS-NG and HyTES datasets and supported the writing and data analysis.

TABLE OF CONTENTS

Acknowledgements	iv
Abstract	vi
Published Content and Contributions	vii
Table of Contents	vii
List of Illustrations	ix
List of Tables	xv
Chapter I: Introduction	1
1.1 Motivation: Why Methane ?	1
1.2 Remote Sensing Observations	3
1.3 Thesis Outline	5
Chapter II: Towards accurate methane point-source quantification from high-resolution 2-D plume imagery	7
2.1 Abstract	7
2.2 Introduction	8
2.3 Plume Observations and Instrument Specifications	10
2.4 Gaussian Plume Modeling and Its Limitations	13
2.5 Large Eddy Simulation Setup	15
2.6 Synthetic Measurement	16
2.7 Results	17
2.8 Discussion and Conclusion	31
Chapter III: MethaNet – an AI-driven approach to quantifying methane point-source emission from high-resolution 2-D plume imagery	34
3.1 Abstract	34
3.2 Introduction	35
3.3 Realistic Plume Simulation	38
3.4 Method	42
3.5 Results	47
3.6 Concluding Remarks	55
Chapter IV: Remote sensing of methane plumes: Instrument tradeoff analysis for detecting and quantifying local sources at global scale	58
4.1 Abstract	58
4.2 Introduction	59
4.3 Data and Methodology	63
4.4 Results and Discussion	71
4.5 Conclusion	88
Chapter V: Conclusions	92
Bibliography	96

LIST OF ILLUSTRATIONS

<i>Number</i>	<i>Page</i>
1.1 Globally-averaged, monthly mean atmospheric methane concentration based on measurements from the National Oceanic and Atmospheric Administration (NOAA, Dlugokencky, 2021). The red line and circles are globally averaged monthly mean values centered on the middle of each month. The black line shows the long-term trend.	2
2.1 Methane plume over a venting shaft in the Four Corners region, observed from four individual AVIRIS-NG airborne instrument overpasses (2.8 m spatial resolution) 7–9 min apart on 22 April 2015 between 16:19:02 and 16:45:06 UTC (a–d) compared with observations from HyTES overpasses (2.3 m spatial resolution) in the similar interval between 16:17:16 and 16:47:17 UTC (e–h). The background is from ©Google Earth imagery.	11
2.2 Column averaging kernels for two instruments, AVIRIS-NG (in blue) and HyTES (in orange), as a function of height. The altitude on the z axis is given above ground level. In the thermal case (HyTES), the flight altitude is an important factor for the CAK. The CAK of HyTES was computed for an altitude of about 3 km. For the shortwave range, however, the CAK of AVIRIS-NG is not impacted significantly by flight altitude.	13
2.3 (a–c) Gaussian plumes under wind speeds of 1, 4, and 10 m s^{-1} respectively, with Pasquill stability type A meaning very unstable. (d–f) Gaussian plumes under a wind speed of 4 m s^{-1} in the stability type A (very unstable), B (unstable), and C (slightly unstable). All cases are with a flux rate of 300 kg h^{-1} and detection threshold set to 500 ppm m^{-1} . The IME is calculated over the entire scene and is in kilograms. The wind speed shown in this Gaussian model is at plume levels.	15

2.4	(a–c) Snapshots of simulated plumes under wind speeds of 1, 4, and 10 m s^{-1} , respectively. (d–f) Time-averaged plumes from 60 time steps under the geostrophic wind speeds of 1, 4, and 10 m s^{-1} , respectively. All with a flux rate of 300 kg h^{-1} and detection threshold set to 500 ppm m^{-1} . All are based on AVIRIS-NG averaging kernels. The IME is calculated over the entire scene and is in kilograms. Note that the temporal averages do not reach a true ensemble average as sample sizes are finite (i.e., the average still exhibits fine structure).	18
2.5	(a–c) Snapshots from simulated plumes under 1, 4, and 10 m s^{-1} , respectively, when applying the AVIRIS-NG instrument column averaging kernel. (d–f) Snapshots from the exact same plumes as in (a–c), respectively, but applying the HyTES averaging kernel. The flux rates are all 300 kg h^{-1} and the detection threshold is set to 500 ppm m^{-1} . The IME is in kilograms.	19
2.6	Mean and standard deviation of the IME associated with a range of flux rates under various background wind speeds from 1 to 10 m s^{-1} . The detection threshold is 500 ppm m^{-1} .	21
2.7	Missing IME, shown as a percentage, for different ppm m^{-1} threshold values. Each curve corresponds to a prescribed source flux rate. The flux rates are incremented by a factor of 2.	22
2.8	A rotated plume snapshot from a run of 4 m s^{-1} background wind speed and 300 kg h^{-1} flux rate with its angular distribution of IME across the plume (right) and its Cartesian distribution of IME along the plume (top). The two black lines denote an angular bin of 0.5° that sweeps through the 2-D plume to construct the angular distribution.	23
2.9	Ensemble-averaged angular distributions of the plume, averaging over all available time steps at various flux rates. Different colors represent different wind speeds. Each distribution is normalized by its maximum value. The vertical bars represent 1 standard deviation of the normalized IME at a given angle across all snapshots.	24
2.10	Relationship between the wind speed and the associated cone width averaged over snapshots and flux rates. The dotted black curve represents the best fit by an exponential function. The shaded area represents 1 standard deviation from the mean plume angular width for each wind speed.	25

2.11	Relationship between flux rate and wind speed for 50 kg IME. The shaded area represents 1 standard deviation from the mean flux rate at each given wind speed.	26
2.12	Comparison between the prescribed flux rate in the model run and the predicted flux rate based on our method of using the IME and the angular width of plume in a given scene. The error bar represents uncertainties associated with the prediction of an individual point source.	27
2.13	Comparison between the predicted and the actual total flux of 30 plumes from 3000 bootstrap rounds.	28
2.14	An observed AVIRIS-NG scene in a controlled-release experiment from a natural gas pipeline located at Victorville, CA (34.8° , -117.3°), on 11 October 2017 with the flux rate of $89 \pm 4 \text{ kg h}^{-1}$	29
2.15	Relationship between the IME and flux rate under different sensible and latent heat fluxes of 200 and 400 W m^{-2} (blue), and 220 and 220 W m^{-2} (orange), compared to the original simulation sensible and latent heat fluxes of 400 and 40 W m^{-2} (green). All cases are under the wind speed of 4 m s^{-1} . The detection threshold was 500 ppm m^{-1}	30
3.1	A map showing detected methane sources from the California Methane Source Finder project. Background image shows AVIRIS-NG flight lines conducted in 2016 and 2017 (white stripes) and locations of detected CH_4 sources (purple circles). The inset images show examples of methane plume enhancement from AVIRIS-NG observations over (a) a landfill, (b) dairy manure area, (c) an oil and gas facility, and (d) a natural gas storage field.	39
3.2	Examples of simulated CH_4 plume images from the LES experiments with 1, 3, 5, 7, or 9 m s^{-1} geostrophic wind speeds (in x-direction) that drive the dynamics of the plumes. Columns represent different random snapshots from each experiment.	41
3.3	An example of a plume image from a simulated plume superposed on a realistic retrieval noise background based on an AVIRIS-NG observation over agricultural area.	42
3.4	An illustration of a data pipeline for pre-processing plume images to be used in training, validation, and test sets.	44
3.5	The MethaNET CNN architecture.	46

3.6	A plot showing a comparison between true fluxes and predicted fluxes by MethaNet when trained using only odd wind speeds to predict unseen plumes under even wind speeds. A dashed line shows a 1:1 reference line.	48
3.7	Examples of plume images with prediction errors higher than average for plumes over (a) agricultural area under the wind speed case of 2 m s^{-1} , (b) desert area, 10 m s^{-1} , (c) agricultural area, 6 m s^{-1} , and (d) urban area, 8 m s^{-1}	49
3.8	A plot showing a comparison between true fluxes and predicted fluxes by MethaNet trained from all LES runs with realistic background noise to predict unseen plumes in test set. A solid line shows a 1:1 reference line.	51
3.9	A plot similar to figure 3.8, but with the synthetic plume images that instead contain lower and uncorrelated noise, which is drawn from Gaussian distribution with a zero mean and a standard deviation of 250 ppm-m . A solid line shows a 1:1 reference line.	52
3.10	Controlled release experiment conducted at Victorville, CA. The scenes represent 3 overpasses with a controlled flux rate of 39 kg h^{-1}	53
3.11	A plot showing the accuracy of MethaNet predictions for a classification task on plumes of different emission rates, calculated within each flux range.	54
3.12	Examples of false positives and false negative predictions from MethaNet in the classification task.	54
4.1	Example of systematic outliers from a retrieved AVIRIS-NG scene (right) compared with an RGB image (left).	62
4.2	A schematic for reflected sunlight from the sun through the atmosphere to a spectrometer in space.	64
4.3	Albedo spectral variations near $2.3 \text{ }\mu\text{m}$ from distinct surface reflectances in our database.	66
4.4	A schematic showing the setup for a methane plume over different surface tiles, each of which contains one surface albedo from our database.	71
4.5	Simulated reflected solar radiance through a plume of 200 kg h^{-1} , over a concrete surface as observed by instruments of different FWHM in the two fitting windows of $1.6 \text{ }\mu\text{m}$ (left) and $2.3 \text{ }\mu\text{m}$ (right). The grey background is the originally calculated spectra at 0.01 nm	72

4.6	Scatter plot showing the relative values of reflectance at 1.6 vs 2.3 μm for different surface types. Each point is a distinct surface, and the color shows the type to which it belongs. Cross marks represent three example surfaces that we used in the comparison analyses. . . .	73
4.7	A plot showing precision errors from CH_4 retrieval in the 1.6 μm band (dotted) and the 2.3 μm band (solid) over three distinct surfaces (colored), using instruments with different FWHM.	74
4.8	(A) The observed spectra through the exact same CH_4 source over two different surfaces, construction concrete and vegetation, as observed by an instrument with FWHM of 1.5 nm, and their best spectral fit. (B) Their associated spectral residuals and an expected $1\text{-}\sigma$ noise level for the instrument measurement.	76
4.9	Plots showing a range of biases that occur over 100 randomly sampled surfaces when different FWHM, SSI, and polynomial degrees are used.	77
4.10	(A) Precision error as a function of instrument FWHM for different numbers of polynomial degrees used in the retrieval (with exposure time of 20 ms). (B) Precision error as a function of instrument FWHM for different exposure times (with polynomial degree of 25). .	79
4.11	A nadir view of a simulated CH_4 plume from the LES with a prescribed flux rate of 200 kg h^{-1} . The background wind speed is 4 m s^{-1} along the x-axis.	80
4.12	Retrieved CH_4 column over 30 different surfaces with varying instrument scenarios. The first row shows the results for an instrument with FWHM of 1.5 nm, while the second row shows the results for an instrument with FWHM of 5.0 nm. Both the first and second rows have $\text{SSI}=\text{FWHM}/2.5$. The third row shows the results for an instrument with FWHM of 5.0 nm and $\text{SSI}=\text{FWHM}$. The biases drop significantly as polynomial degrees increase.	82
4.13	A plot showing the values of reduced χ^2 from the retrieval of different instrument FWHM and polynomial degrees. As the polynomial degree becomes higher, the reduced χ^2 decreases, implying a better spectral fit.	83
4.14	The increase in precision errors when the polynomial degrees of 50, 25, and 11 are used as compared to the polynomial degree of 5 case. The increase is computed for a given FWHM and SSI according to each row.	84

4.15	RGB and 2.2 μm albedo images of a realistic surface distribution in the Durango area, Colorado from LANDSAT.	85
4.16	Retrieved CH_4 column over a well pad in the Durango area, Colorado area with varying instrument FWHM and polynomial degrees in the retrieval. The realistic surface distribution is based on LANDSAT data. The use of the polynomial degree of 25 and FWHM of 1.5 nm can reduce biases and precision error over this scene.	86
4.17	A plot similar to Figure 4.16, but at 30m resolution. Retrieved CH_4 column over a well pad in the Durango area, Colorado area with varying instrument FWHM and polynomial degrees in the retrieval. The realistic surface distribution is based on LANDSAT data. The use of the polynomial degree of 25 and FWHM of 1.5 nm can reduce biases and precision errors across the scene.	87
4.18	Retrieved CH_4 column over a well pad in the Durango area, Colorado area for plumes of various emission rates. The spatial resolution is 30 m, the instrument FWHM is 1.5 nm, and the polynomial degree in the retrieval is 1.5. The realistic surface distribution is based on LANDSAT data. Column enhancement in the vicinity of CH_4 plume is increasingly visible as the source emission rate becomes larger. . .	88
4.19	Ratio of retrieved CH_4 excess column divided by the posterior precision error, over a simulated scene in the Durango area, Colorado area for plumes of various emission rates. The spatial resolution is 30 m, the instrument FWHM is 1.5 nm, and the polynomial degree in the retrieval is 25. The realistic surface distribution is based on LANDSAT data. Ratios higher than 4 imply a probability of lower than 1 in 15000 that the pixel enhancement happens by random noise.	88

LIST OF TABLES

<i>Number</i>		<i>Page</i>
3.1	A table showing the number of synthetic CH ₄ scenes used in training, validation, and test sets in two training scenarios.	45
4.1	A table for default parameter settings in our simulations.	68

Chapter 1

INTRODUCTION

1.1 Motivation: Why Methane ?

Methane (CH₄) is one of the most dominant anthropogenic greenhouse gases in the Earth climate system. Since preindustrial time, atmospheric methane concentration has nearly tripled to almost 1900 ppb (Dlugokencky, 2021; Saunio et al., 2020). Its rising atmospheric concentration, coupled with its strong molecular absorption of Earth's emitted thermal infrared radiation, makes methane the second strongest anthropogenic greenhouse gas overall, after carbon dioxide (CO₂). In addition, CH₄ enhances both tropospheric ozone and stratospheric water vapor, both of which contribute to additional indirect radiative forcing. Because the atmospheric lifetime of CH₄ (≈ 9 years) is orders of magnitude smaller than that of CO₂ (≈ 100 – 500 years), reduction in current CH₄ emissions can lead to a decrease or stabilization of its concentration in the atmosphere more rapidly, i.e. on decadal timescales. CH₄ is thus recognized as an effective target for reduction and mitigation strategies to achieve short- and medium-term reductions of global warming (Montzka et al., 2011a; Prather et al., 2012; Shindell et al., 2012).

Despite its well-appreciated significance, our understanding of the global and regional CH₄ budget remains uncertain due to inadequate knowledge in the quantification of CH₄ emissions from various source types (Houweling et al., 2017; Turner et al., 2017). Discrepancies between the bottom-up and top-down approaches have not been reconciled and the uncertainties in emissions can reach 40-60 % at a regional level (Saunio et al., 2016; Turner et al., 2019). These uncertainties in the emission quantifications have led to ongoing debates regarding the cause of the global methane trend, in which we saw a hiatus of methane concentration increase between 2000 and 2007, followed again by a continuous rise since then (Figure 1.1). Many studies have tried to attribute what could be the cause of this trend, but no clear agreement has been reached (Bergamaschi et al., 2013; Bousquet et al., 2011; Kort et al., 2016; Rigby et al., 2017; Turner et al., 2017). Regardless of the ambiguity in the trend attribution, there is no disagreement regarding the fact that methane concentrations currently exhibit a global continuous rise. Projections of anthropogenic methane emissions suggested that significant reductions of methane

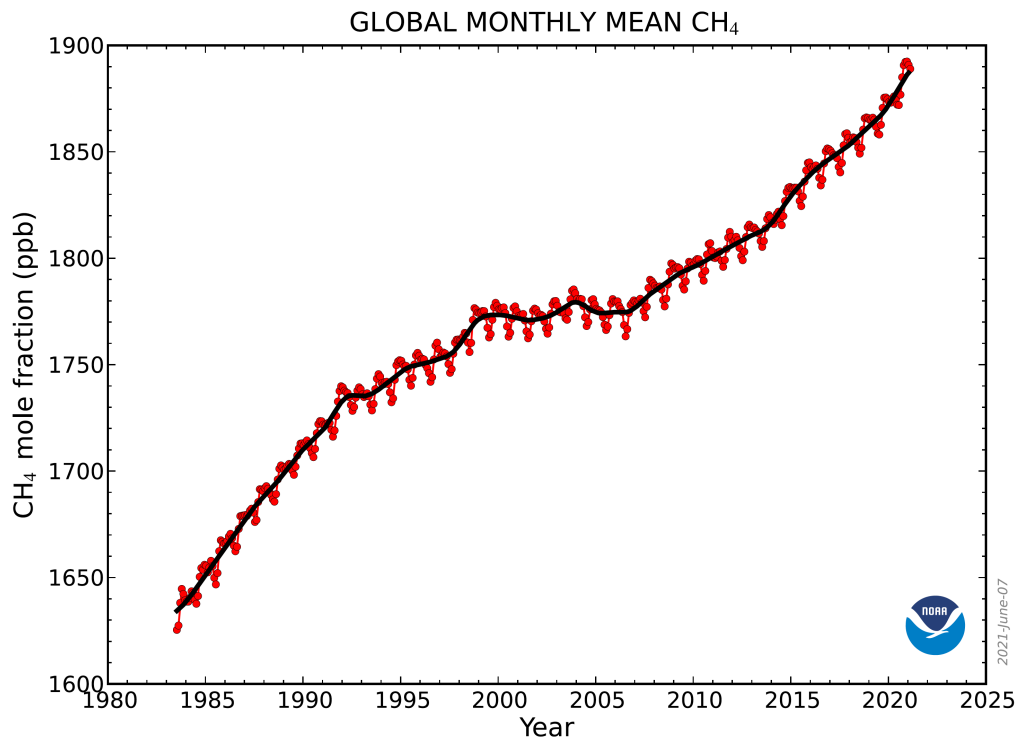


Figure 1.1: Globally-averaged, monthly mean atmospheric methane concentration based on measurements from the National Oceanic and Atmospheric Administration (NOAA, Dlugokencky, 2021). The red line and circles are globally averaged monthly mean values centered on the middle of each month. The black line shows the long-term trend.

emissions are integral to accomplish the 1.5–2 C° target of the Paris Agreement (Collins et al., 2013; Nisbet et al., 2019). As CH₄ reduction plays a significant role in climate mitigation efforts, one crucial step in emission reduction is determining the location and emission rate of methane sources, since we can only manage what we measure. This is underpinned in the 2018 NASA Decadal Survey, which calls out the identification and understanding of CH₄ source emissions as one of the top priorities in the efforts to improve future climate projections, and help lead the way in emission reduction (Sciences and Medicine, 2018).

Because anthropogenic methane emission contributes to about 60 % of total global emission and is a direct consequence from human activities, anthropogenic sources are most relevant targets in planning mitigation strategies. Fossil fuels account for roughly 34 % of the anthropogenic emission, agriculture and waste for 57 %, and biomass and biofuel burning for around 9 % (Saunois et al., 2016). These

anthropogenic methane emission sources come in two broad categories as point sources and diffusive sources based on the physical properties of surface features from which methane is emitted. In this thesis, we are mostly concerned with methane emissions from point sources since they are prevalent among some of the most important emission sectors such as coal mining and oil and gas industry (Brandt et al., 2014; Duren et al., 2019), and also common in emissions from agriculture and landfill (Duren et al., 2019). As point sources are often well-defined and local in nature, they represent a scenario where direct mitigation actions can readily be taken after emissions such as leakage from faulty equipment are detected and quantified. Improved measurement of localized CH₄ point sources is integral to implementing and prioritizing mitigation efforts in the most effective manner since policy and remedy actions often take place at local scales. Furthermore, identifying and quantifying CH₄ point sources with reduced uncertainties would permit demystifying the processes that affect CH₄ concentration in the troposphere. Not only will this aid the explanation of mechanisms driving current CH₄ trends, but it will also enhance future climate projection and modelling efforts of the global carbon cycle and ecosystem.

1.2 Remote Sensing Observations

One approach to measure CH₄ emission sources is using surface monitoring networks, which provide accurate and precise in-situ measurements of CH₄. However, they are sparse in coverage across large geographical areas and mostly representative of large-scale background concentrations. They may not be available over areas with significant emissions. Oil and gas facilities sites, for example, often have limited access for measurements resulting in their emissions accounted for by inventories-based approach that is likely underestimated and not real-time (Brandt et al., 2014; Hsu et al., 2010; Kort et al., 2008). Remote-sensing instruments using absorption spectroscopy have emerged as one promising solution for measuring atmospheric CH₄ concentration over large geographical areas. In the past decade, advancements in the space-based CH₄ retrieval techniques from satellite observations such as the SCanning Imaging Absorption SpectroMeter for Atmospheric CHartographY (SCIAMACHY) and Greenhouse gases Observing SATellite (GOSAT) have enabled a top-down constraint on global CH₄ emissions (Frankenberg et al., 2005a; Frankenberg et al., 2011; Kort and Frankenberg, 2014; Kuze et al., 2009). However, due to their coarse spatial resolutions (≈ 50 km), their measurements do not distinguish magnitudes of different anthropogenic sources – information critical for

accurately identifying the causes of changes in atmospheric CH₄ concentration and its consequences. The TROPOspheric Monitoring Instrument (TROPOMI) with a spatial resolution of a few kilometers has been shown to be capable of identifying regions of high emissions (Gouw et al., 2020; Hu et al., 2018), but the measurements are not yet at a level where local sources can be identified and mitigated directly.

One potential solution to this scale gap is using an airborne instrument based on the same techniques as in satellite remote sensing to quantify CH₄ plumes, but which has a much higher spatial resolution such as the next-generation Airborne Visible/Infrared Imaging Spectrometer (AVIRIS-NG, Thorpe et al., 2017). This is based on the insight that methane column enhancements at high spatial resolution (a few meters) can be so high that the retrieval of the absorbing feature can be done even with moderate spectral resolution (5–10 nm). Using absorption features of CH₄ in the short-wave infrared around 2.3 μm , column integrated CH₄ concentration can be retrieved at a spatial resolution well below 5 m. This enables the generation of 2-D methane column enhancement map, which is then used for the detection and quantification of CH₄ point sources. Previous studies have utilized this technique for several field campaigns in California and the Four Corners regions, where a total of more than 500 strong point sources have been detected (Duren et al., 2019; Frankenberg et al., 2016). On a few occasions during those campaigns, emissions from pipe leakages were detected. Once they were reported to their facilities, these leakages were fixed and those emissions were no longer found on a follow-up flight. This exemplifies a promising venue for effective direct methane mitigation. However, there are two key bottlenecks that need to be overcome in order to apply this concept towards building a global monitoring system to measure CH₄ point sources across the planet. The first bottleneck is that high uncertainties exist in quantifying point source emission rates from the observed column enhancement in the source vicinity. These uncertainties can be up to 100% for individual plumes, and are mainly driven by uncertainties in wind speed data involved in the flux inversion calculations (Duren et al., 2019). Systematic covariances in the flux inversion biases across individual source estimates can also propagate to aggregated regional estimates. Thus, we have to focus on bias-free flux inversions, realizing that certain precision errors from individual plumes are unavoidable. Assuming, for instance, a single wind speed from reanalysis data for a specific flight campaign date would directly propagate into estimates of regional total fluxes since a potential wind-speed bias would be identical for all individual plumes. Randomizing biases for single plumes is thus a prerequisite to minimize biases for aggregated emissions estimates.

The second bottleneck is that the identification of emission locations based on the retrieved column enhancement distribution are confounded by the occurrences of retrieval artefacts that often correlate with specific surface features. These artefacts on the retrieved column enhancement map greatly impact the ability to identify and quantify actual CH₄ plumes. These two issues make it difficult for the detection and quantification of local sources to be determined in an automated and accurate manner.

In this thesis, we tackle these two most significant persisting problems, with the primary focus on developing novel methods that allow the detection and quantification of CH₄ point sources to be made accurately based on the 2-D retrieved CH₄ column enhancement field, which we refer to as plume images.

1.3 Thesis Outline

In regards to the aspect of quantifying CH₄ plumes, we first explored the relationship between the source emission rate and the corresponding spatial distribution of column enhancement under different atmospheric conditions. In Chapter 2, we used large eddy simulations (LESs, Matheou and Bowman, 2016) to simulate the plume dynamics at high spatial resolution (5 m) with prescribed source rates under various background wind speeds and typical surface latent and sensible heat fluxes. The LES enables a realistic simulation of how methane concentrations from a point source evolve in space and time. Using 3-D LES model output for each snapshot, we simulated synthetic 2-D airborne measurements by applying respective instrument averaging kernels. Based on these synthetic measurements, we show in this chapter that the plume spatial distribution as observed in a 2-D CH₄ column enhancement image can be used to deduce the underlying wind speed. This deduced wind speed, together with the integrated methane enhancement (IME) over the entire plume, allows us to quantify the source emission rate directly from a plume image without relying on any ancillary data such as local wind speed measurements. In Chapter 3, we took a step further from Chapter 2 and built a customized deep learning model based on convolutional neural networks (CNN) architecture to learn the mapping between a given retrieved plume image and its emission rate. We applied it to a large training dataset of methane plumes from LES output at various flux rates, wind speeds, added realistic measurement noise, offsets, and rotations. We trained our model, named MethaNet, to predict flux rates directly from 2-D methane plume images. This is the first time that CNN has been used for a regression task to quantify methane plume emission from 2-D high-resolution imagery. We demonstrated that

MethaNet can achieve a level of performance for quantifying methane emission rate that is a state-of-the-art achievement for a model that does not rely on wind speed information. Our analyses in Chapter 3 suggested that plume images with low and uncorrelated retrieval noise lead to enhanced model performance by enabling the model to differentiate an actual plume from retrieval artefacts due to surface biases and random noise. Chapter 4 deals with an instrument tradeoff analysis to understand how precision error and bias in the retrieval of methane column enhancement changes as a result of using different instrument spectral resolutions, optical performance and detector exposure times by using a realistic instrument noise model. In this chapter, we also formally analyzed the impact of spectrally complex surface albedo features on retrievals using the Iterative Maximum A Posteriori-Differential Optical Absorption Spectroscopy (IMAP-DOAS) algorithm. We built an end-to-end modelling framework that can simulate observed radiances from reflected solar irradiance through a simulated CH₄ plume over several natural and man-made surfaces. Our analysis shows that complex surface features can alias into retrieved methane abundances, explaining the existence of retrieval biases in current airborne methane observations. We demonstrated how the impact from surface interferences can be mitigated with higher spectral resolution and a larger polynomial degree to approximate surface albedo variations. Chapter 5 provides the overall conclusions of the thesis.

*Chapter 2***TOWARDS ACCURATE METHANE POINT-SOURCE
QUANTIFICATION FROM HIGH-RESOLUTION 2-D PLUME
IMAGERY**

Jongaramrungruang, S. et al. (2019). “Towards accurate methane point-source quantification from high-resolution 2-D plume imagery”. In: *Atmospheric Measurement Techniques* 12.12. ISSN: 18678548. DOI: [10.5194/amt-12-6667-2019](https://doi.org/10.5194/amt-12-6667-2019).

2.1 Abstract

Methane is the second most important anthropogenic greenhouse gas in the Earth climate system, but emission quantification of localized point sources has proven challenging, resulting in ambiguous regional budgets and source category distributions. Although recent advancements in airborne remote sensing instruments enable retrievals of methane enhancements at an unprecedented resolution of 1–5 m at regional scales, emission quantification of individual sources can be limited by the lack of knowledge of local wind speed. Here, we developed an algorithm that can estimate flux rates solely from mapped methane plumes, avoiding the need for ancillary information on wind speed. The algorithm was trained on synthetic measurements using large eddy simulations under a range of background wind speeds of 1–10 m s⁻¹ and source emission rates ranging from 10 to 1000 kg h⁻¹. The surrogate measurements mimic plume mapping performed by the next-generation Airborne Visible/Infrared Imaging Spectrometer (AVIRIS-NG) and provide an ensemble of 2-D snapshots of column methane enhancements at 5 m spatial resolution. We make use of the integrated total methane enhancement in each plume, denoted as integrated methane enhancement (IME), and investigate how this IME relates to the actual methane flux rate. Our analysis shows that the IME corresponds to the flux rate nonlinearly and is strongly dependent on the background wind speed over the plume. We demonstrate that the plume width, defined based on the plume angular distribution around its main axis, provides information on the associated background wind speed. This allows us to invert source flux rate based solely on the IME and the plume shape itself. On average, the error estimate based on randomly generated plumes is approximately 30 % for an individual estimate and less than 10 % for an aggregation of 30 plumes. A validation against a natural gas controlled-release

experiment agrees to within 32 %, supporting the basis for the applicability of this technique to quantifying point sources over large geographical areas in airborne field campaigns and future space-based observations.

2.2 Introduction

Methane is the second most important anthropogenic greenhouse gas in Earth's atmosphere, with additional indirect impacts as it affects both tropospheric ozone and stratospheric water vapor. Despite its significance, our understanding of global and regional CH₄ budgets has remained inadequate due to the fact that the strength and distribution of CH₄ emissions from various source types are not well-constrained (Houweling et al., 2017; Turner et al., 2017). Estimates of CH₄ emissions from point sources (e.g., at facility scale) are particularly uncertain, since space-based observations lack sufficiently fine spatial resolutions while in situ measurements are too sparse and mostly representative of large-scale background concentrations. Improved estimates of the CH₄ emissions at this point-source scale are critical in guiding emission mitigation efforts.

Recent developments in airborne imaging spectroscopy techniques to quantify CH₄ plumes have opened the way for CH₄ measurements at a sufficiently high spatial resolution needed to differentiate various local sources within regional scales (Frankenberg et al., 2016; Hulley et al., 2016; Thompson et al., 2015; Thorpe et al., 2016; Thorpe et al., 2017; Tratt et al., 2014). A recent airborne campaign in the Four Corners region retrieved column methane enhancements at a resolution of 3 m (Frankenberg et al., 2016), enabling the observation of the plume shape in the direct vicinity of the point source. During the campaign, many plumes of various sizes ranging from a few tens of meters to hundreds of meters were detected across the region, with the majority of their source emission rates between 10 and 1000 kg (CH₄) h⁻¹ (Frankenberg et al., 2016). This allows for an effective way to remotely identify and locate CH₄ emissions from point sources such as pipeline leaks or oil and gas facilities. The retrievals provide the quantification of a column enhancement (e.g., in molecule cm⁻² above background), which can be integrated across the entire methane plume to derive the total amount of methane within the plume, denoted as integrated methane enhancement (IME, either in molecule or mass units, Frankenberg et al. (2016)). In addition, the instrument observes the fine structure of the plume at an unprecedented spatial resolution. However, the flux inversion from the observed plumes to the actual emission rate at the source remains complicated due to the dependence on tropospheric boundary layer conditions such as wind speed

and atmospheric stability during the overpass. To interpret the relationship between the observed plumes and flux rates, previous studies have relied on Gaussian plume inversion models (Gorelick et al., 2016; Krings et al., 2013; Rayner et al., 2014; Nassar et al., 2017; Schwandner et al., 2017) or an airborne in situ approach using a mass balance calculation based on the enhancement downwind of the source (Cambaliza et al., 2015; Conley et al., 2016; Gordon et al., 2015; Jacob et al., 2016; Lavoie et al., 2015). Frankenberg et al. (2016) used a simple linear scaling between the IME and flux rate, which allowed for a straightforward derivation of fluxes from the observed IME given an averaged wind speed across a large region for the campaign over several days. Varon et al. (2018) estimated the flux rate as the IME divided by the residence time of methane in the plume calculated based on the effective length of the plume from its area and the effective wind speed inferred from 10 m wind speed by in situ measurement or meteorological reanalysis data. All of these methods rely on knowledge of local wind speed, which is acquired through either in situ wind measurements or the estimation from meteorological forecast or reanalysis data. The former can be costly and time consuming without prior knowledge of source locations, while the latter can be inaccurate due to the rapid changes of a local plume over a much shorter temporal and spatial scale (minutes, hundreds of meters) than the typical atmospheric reanalysis products (a-few-hourly average, tens of kilometers).

In this work, we aim to improve our understanding of how the inferred emission rates change under different atmospheric conditions, e.g., the errors due to a lack of accurate wind measurements. To investigate this relationship and associated errors, we used large eddy simulations (LESs, Matheou and Bowman (2016)) to simulate the plume dynamics at high spatial resolution (5 m) with prescribed source rates under various background wind speeds and typical surface latent and sensible heat fluxes. Using 3-D LES model output for each snapshot, we simulated synthetic 2-D airborne measurements by applying the respective averaging kernels. Based on these synthetic measurements, we developed an algorithm to deduce the wind speed from the plume's spatial distribution and investigate the degree to which the flux rate can be inverted from only the remotely sensed CH_4 retrievals. This allowed us to perform an end-to-end test of errors in inverted methane fluxes in both the absence and presence of ancillary information on the actual wind speed.

This work was inspired by the use of IME to quantify methane single-point sources from field campaigns using airborne instruments. These plumes generally are of

small-to-medium sizes (< 2 km). The concept, nevertheless, can be applicable to larger sources as well as toward measurement of localized sources from space in the coming decade for satellite retrievals at a much finer spatial resolution.

Section 2.3 illustrates the plume observations and the instrument specifications. Section 2.4 will give a brief overview of Gaussian plume modeling. The setup of the LES and application of instrument operators to simulate airborne measurements are described in Sections 2.5 and 2.6, respectively. Section 2.7 shows simulated plumes under different atmospheric scenarios and the relationship between observed IME and actual emission rates. The error analysis of flux inversion based on the IME method is also provided. The final section provides a discussion and conclusion.

2.3 Plume Observations and Instrument Specifications

Figure 2.1 shows examples of observed methane plumes using the next-generation Airborne Visible/Infrared Imaging Spectrometer (AVIRIS-NG) and the Hyperspectral Thermal Emission Spectrometer (HyTES) during the Four Corners flight campaign (Frankenberg et al., 2016). The match filter method (Thompson et al., 2015) and clutter matched filter (CMF) were used to retrieve the scenes from AVIRIS-NG and HyTES, respectively. In this case, the aircraft repeatedly flew over a coal mine venting shaft, with approximately 10 min revisit time. Evidently, the plume is changing in time and exhibits fine-scaled features due to atmospheric turbulence. Quantifying the source rate from detected plumes using atmospheric simulations to understand their behavior and variations in space and time is the main subject of this work. In order to compare our simulations with actual observations, we need to take the measurement characteristics of the remote sensing instrument into account. This relates to both measurement precision, which determines detection thresholds which mark and define the detected plume, as well as vertical sensitivity, which affects what parts of the plume structure can actually be observed. Depending on the techniques being used, both can vary widely.

The left column in Fig. 2.1 shows scenes that are retrieved from the AVIRIS-NG instrument, which measures reflected solar radiation between 0.35 and $2.5 \mu\text{m}$ at 5 nm resolution and sampling (Hamlin et al., 2011; Thompson et al., 2015). To first order, it has a uniform vertical sensitivity (averaging kernel) of 1 at each height (see Fig. 2.2). Another instrument that was used in the Four Corners campaign is HyTES, which enables the detection of CH_4 plumes due to its absorptions in the thermal infrared around $7.65 \mu\text{m}$ (Hulley et al., 2016). Its varying sensitivity in the

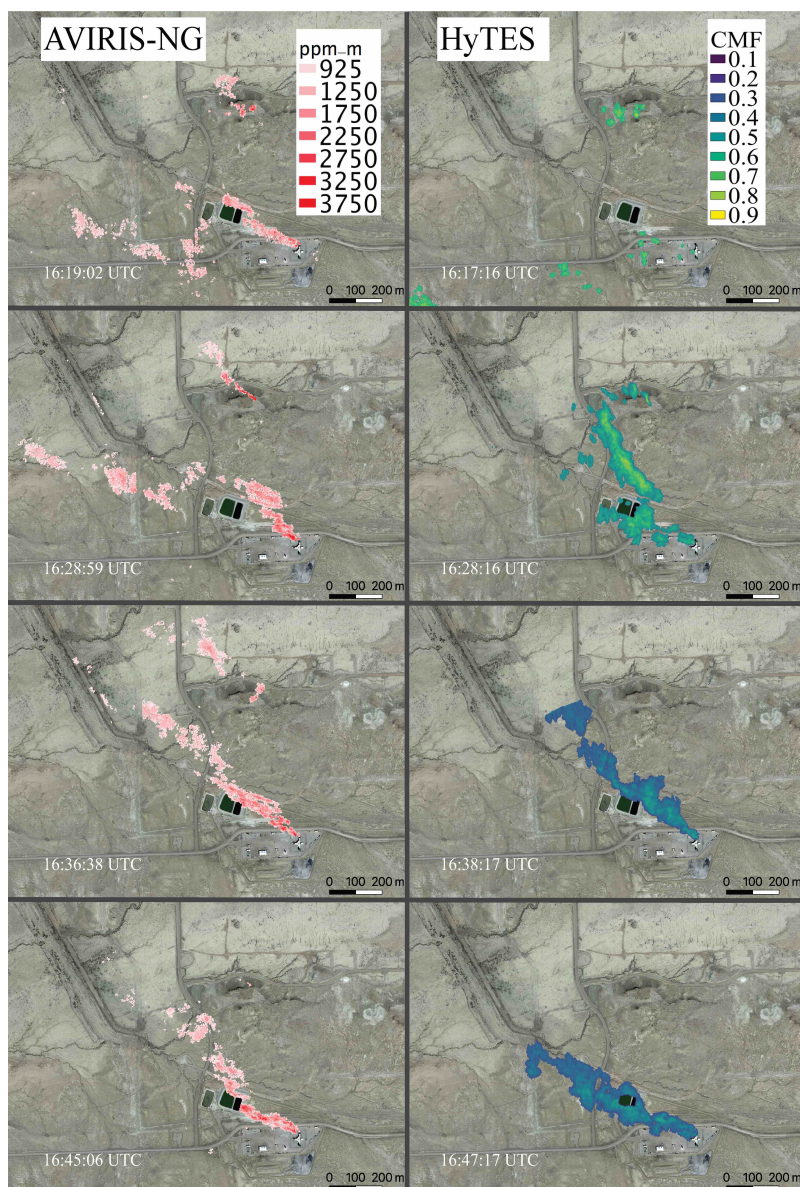


Figure 2.1: Methane plume over a venting shaft in the Four Corners region, observed from four individual AVIRIS-NG airborne instrument overpasses (2.8 m spatial resolution) 7–9 min apart on 22 April 2015 between 16:19:02 and 16:45:06 UTC (a–d) compared with observations from HyTES overpasses (2.3 m spatial resolution) in the similar interval between 16:17:16 and 16:47:17 UTC (e–h). The background is from ©Google Earth imagery.

vertical can be calculated as the derivative of the retrieved total column amount with respect to the change in a particular layer. These vertical sensitivities are formally called column averaging kernels. They inform us on how well methane deviations from the prior at each height can be measured, which determines whether they will

be visible in retrieved column enhancements. Mathematically, we can express this relationship as

$$E(i, j) = \sum_k (\Delta x \Delta y \Delta h) \cdot C(i, j, k) \cdot \text{CAK}(k), \quad (2.1)$$

where $E(i, j)$ is the observed total column enhancement (mass or molecules) at the horizontal grid cell (i, j) . Δx , Δy , and Δh are grid sizes in \hat{i} , \hat{j} , and \hat{k} , respectively; C is the concentration (mass or molecules per volume); and $\text{CAK}(k)$ denotes the column averaging kernel evaluated at level k . Technically, the CAK can also be a function of location (i, j) , but for the purpose of producing synthetic measurements from our simulations in this work, we apply the CAK only as a function of height.

Figure 2.2 illustrates the difference between the column averaging kernels that we use to model AVIRIS-NG and HyTES synthetic measurements. The distinct column averaging kernels of both instruments hold significant importance, each with its advantages and disadvantages. The column averaging kernel of AVIRIS-NG is approximately uniform across all vertical levels, which implies that the retrieved column enhancement accurately reflects the actual column enhancement. On the other hand, the sensitivity of HyTES is almost zero near the surface, but increases with height, becoming even larger than 1 at a certain height. This means that the instrument is almost blind to methane near the ground, but amplifies the actual methane amount at certain heights in the column. This distinction is evident in Fig. 2.1 where the observed methane plume remains more consistent from AVIRIS-NG scenes, whereas more variations appear in the HyTES scenes potentially due to changes in plume vertical structures. It should also be noted that the HyTES averaging kernel strongly depends on the temperature profile as well as the surface temperature, which can vary within and between scenes. In contrast, averaging kernels using shortwave reflected light are less variable.

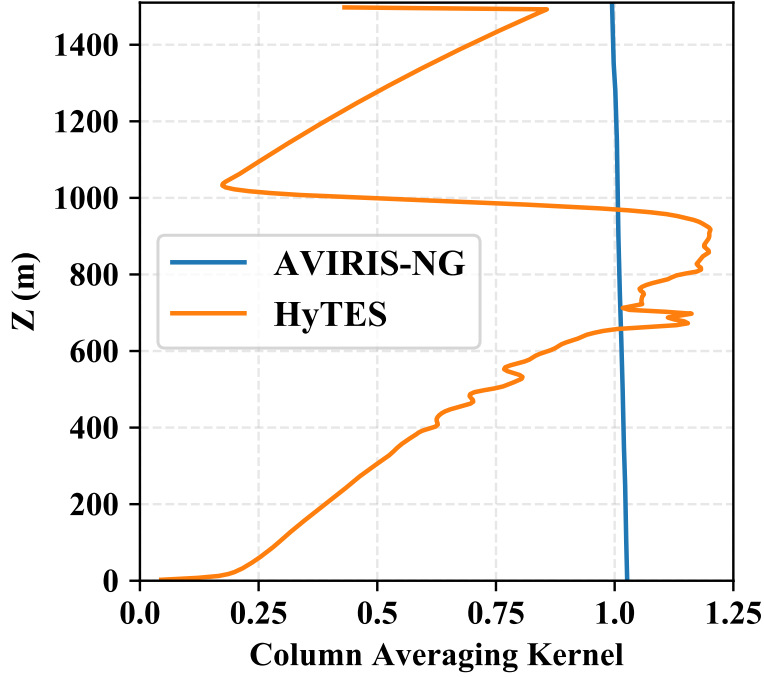


Figure 2.2: Column averaging kernels for two instruments, AVIRIS-NG (in blue) and HyTES (in orange), as a function of height. The altitude on the z axis is given above ground level. In the thermal case (HyTES), the flight altitude is an important factor for the CAK. The CAK of HyTES was computed for an altitude of about 3 km. For the shortwave range, however, the CAK of AVIRIS-NG is not impacted significantly by flight altitude.

2.4 Gaussian Plume Modeling and Its Limitations

The simplest way to simulate plumes is Gaussian plume modeling, which assumes a steady and uniform wind U along the x axis and orthogonal spreading of the plume in crosswind (y axis) and vertical (z axis) directions. The spreading of the plume depends on the dispersion functions $\sigma_y(x)$ and $\sigma_z(x)$. The dispersion functions depend on the atmospheric stability (Pasquill, 1961). For instance, convective conditions favor vertical dispersion, whereas in a stable atmosphere, the plume primarily disperses in the horizontal directions (Briggs, 1973; Matheou and Bowman, 2016; Sutton, 1931). The three-dimensional Gaussian plume equation is given by (Matheou and Bowman, 2016)

$$C(x, y, z) = \frac{1}{2\pi\sigma_y(x)\sigma_z(x)} \cdot \frac{Q}{U} \cdot \exp\left[-\frac{y^2}{2\sigma_y^2(x)}\right] \sum_{m=0}^{\infty} \left(\exp\left[-\frac{(z-2mz_i)^2}{2\sigma_z^2(x)}\right] + \exp\left[-\frac{(z+2mz_i)^2}{2\sigma_z^2(x)}\right] \right), \quad (2.2)$$

where $C(x, y, z)$ is the (equilibrium) concentration at each point in the three-dimensional space within the atmospheric boundary layer with inversion height z_i . The model assumes a reflective boundary condition where the parameter m multiplied by z_i indicates the height at which the reflection occurs and the summation over this parameter m represents the equivalent concentration within 0 to z_i . Q is the source flux rate at the origin. The variances $\sigma_y(x)$ and $\sigma_z(x)$ are given by empirical relations based on atmospheric stability following the Pasquill classification (Matheou and Bowman, 2016; Pasquill, 1961).

By integrating Eq. (2.2) in the z direction, the methane column enhancement can be modeled in analytical form as

$$\bar{C}(x, y) = \frac{1}{\sqrt{2\pi}\sigma_y(x)} \cdot \frac{Q}{U} \cdot \exp\left[\frac{-y^2}{2\sigma_y^2(x)}\right]. \quad (2.3)$$

Based on this model, we can vary the source rate, wind speed, and stability category to simulate the 2-D integrated concentration field. We then apply a device detection threshold to illustrate how the synthetic Gaussian plume column enhancement may change under distinct atmospheric conditions. Examples of the simulated Gaussian plumes with a flux rate of 300 kg h^{-1} are shown in Fig. 2.3. The left column of Fig. 2.3 shows the Gaussian plumes under different wind speeds for a fixed stability category, while the right column demonstrates those under a fixed wind speed at 4 m s^{-1} but different stability regimes.

The wind speed U influences the column enhancement, which, based on Eq. (2.1), is proportional to the ratio Q/U . Thus, the Gaussian plume model suggests a strong dependence of the IME on wind speed, which in turn does not explicitly affect the shape of the plume. One way of quantifying a plume shape is using an aspect ratio in the x - y plane. In the Gaussian plume model, the aspect ratio of the plume only changes when the stability switches from one category to another. Thus, the wind speed is only implicitly linked to the shape of the plumes by affecting the stability categories and changing the crosswind variances (as can be seen in Eq. 2.3).

The stability categories in this model, nonetheless, are based on empirical formulae. In reality, the wind speed can influence the shape and distribution of the plumes more directly through advection of the tracer along the flow. The actual plume observations from the Four Corners campaign (Fig. 2.1) demonstrate that the plumes are of turbulent nature – at times being discontinuous – and cannot be modeled as Gaussian when only one plume snapshot in time is recorded. Therefore, we utilize

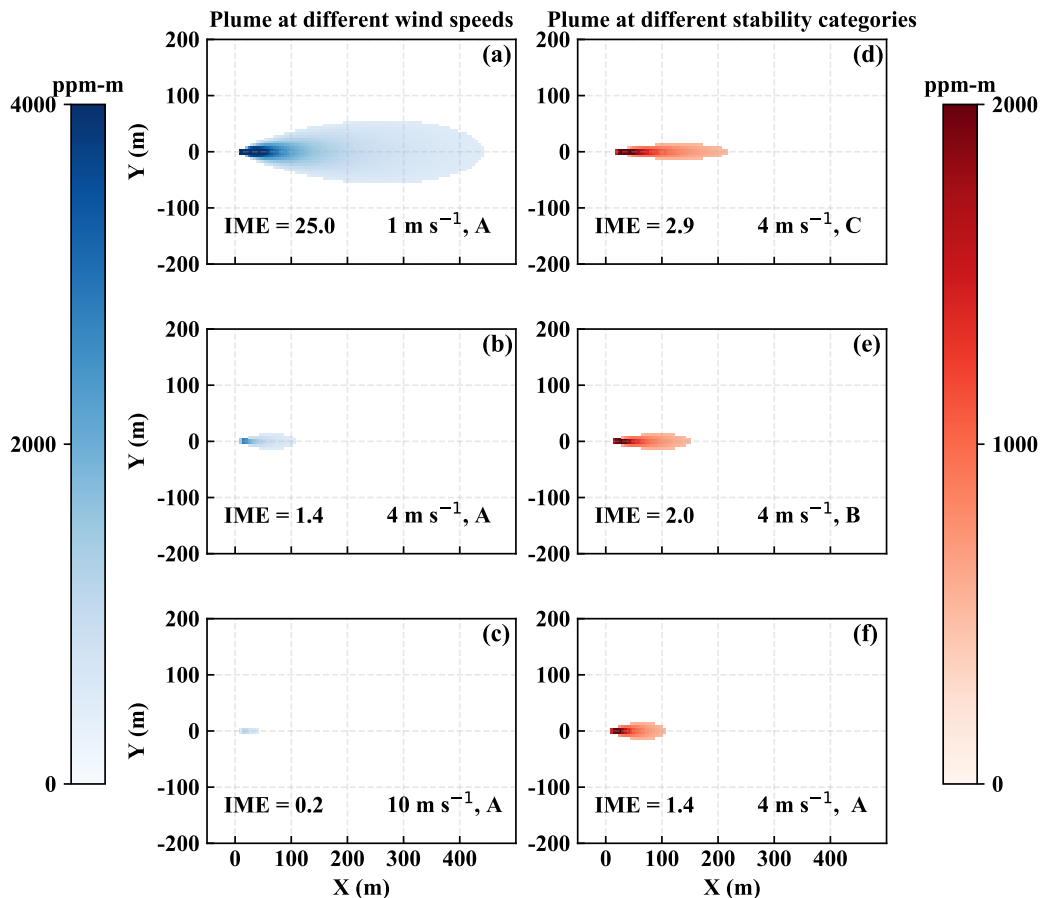


Figure 2.3: (a–c) Gaussian plumes under wind speeds of 1, 4, and 10 m s⁻¹ respectively, with Pasquill stability type A meaning very unstable. (d–f) Gaussian plumes under a wind speed of 4 m s⁻¹ in the stability type A (very unstable), B (unstable), and C (slightly unstable). All cases are with a flux rate of 300 kg h⁻¹ and detection threshold set to 500 ppm m⁻¹. The IME is calculated over the entire scene and is in kilograms. The wind speed shown in this Gaussian model is at plume levels.

an LES model, which yields a realistic realization of the turbulent flow and the methane plume, to quantify the effect of wind speed on the plume structure.

2.5 Large Eddy Simulation Setup

Realistic modeling of CH₄ plumes is a prerequisite for this study. We use LES to model the time-resolved three-dimensional CH₄ distribution in the boundary layer under different atmospheric conditions at resolutions currently available from aircraft measurements (1–5 m). The LES model setup for the simulation of plumes emanating from point sources is as described in Matheou and Bowman (2016). Further details of the model formulation, including the turbulence parameterization,

are in Matheou et al. (2014). A methane surface point source with a specific emission rate in a cloud-free convective atmospheric boundary layer is simulated. The buoyancy of methane is currently being ignored – a good approximation for the present methane concentrations away from the source.

The atmospheric boundary layer is initialized with a mixed layer inversion free troposphere with an initial inversion height $z_i = 800$ m. The initial potential temperature and specific humidity in the mixed layer are $\theta = 298$ K and $q_t = 6.6$ g kg⁻¹. The lapse rate is $\Delta\theta/\Delta z = 0.12$ K m⁻¹. The flow in the boundary layer is driven by a constant geostrophic wind in the x direction, u_g . Different values of the geostrophic wind from 1 to 10 m s⁻¹ are used. The surface sensible and latent heat fluxes are 400 and 40 W m⁻². These values are based on typical field campaign data. Additional simulations with other sensible and latent heat fluxes are also performed later in Sect. 6.4. Surface momentum fluxes are estimated using Monin–Obukhov similarity theory (MOST).

The model domain is $10.24 \times 2.56 \times 1.5$ km³ in the x , y , and z direction, and the grid resolution is uniform and isotropic $\Delta x = \Delta y = \Delta h = 5$ m. The model computational time step is 1 s. Following 1 h of model spin-up, where fully developed three-dimensional turbulence is established in the boundary layer, the three-dimensional concentration at each location at 1 min intervals (snapshots are written out at every minute) is used to construct the synthetic observations. Furthermore, the 10 and 2 m wind speeds are extracted from the model output to compare with the large-scale geostrophic wind value in each run.

2.6 Synthetic Measurement

With the output from the LES simulations, we can create synthetic measurement of a plume instance that would enable simulation of observations from any instrument. The procedure is that we apply vertical integration as described by Eq. (2.1) to the 3-D concentration at a given time step, using the column averaging kernel of the instrument of interest. We apply the column averaging kernel of AVIRIS-NG as well as that of HyTES to produce synthetic measurements for these instruments. The detection thresholds of the AVIRIS-NG and HyTES instruments can potentially be dependent on the surface properties such as surface reflectance and surface temperature, respectively. However, given the typical scale of the plumes of our interest, we assume an average uniform detection threshold across the scene. Here, we use a constant threshold of 500 ppm m⁻¹ (or about $1.34 \cdot 10^{18}$ molecules cm⁻²),

which is a common value for AVIRIS-NG. As for HyTES, we used the same threshold to exemplify the differences due to averaging kernels only, as opposed to thresholds. This allows us to understand to what extent each instrument can detect CH₄ plumes under various wind speeds.

2.7 Results

The output from the LES run provides a more realistic simulation, compared to the Gaussian model, of the plume dynamics as shown in Fig. 2.4 for AVIRIS-NG synthetic measurements. The left column of Fig. 2.4 shows single snapshots of the plume, while the right column shows the time-averaged plume snapshots over 60 time steps, spanning a duration of 60 sequential minutes in total, under distinct background wind speeds but with a constant flux rate. Based on this simulation, we see that the plume varies rapidly in shape and orientation from snapshot to snapshot due to turbulence. The temporal averages in the right column also still exhibit some structure as we only averaged 60 individual snapshots. Overall, the simulated plumes from the LES closely resemble actual plumes from remotely sensed observation as shown in Fig. 2.1. The instantaneous plumes exhibit non-Gaussian behavior; sometimes the plume can even be discontinuous as eddies can rupture the plume structure. However, we found that the total enhancement across the scene (the IME) remains rather constant over time for a given wind speed and flux rate, making it a reliable variable for performing the flux inversion of the source. In addition, we also found that the plumes have distinct features in both magnitude and spatial characteristics for different wind speeds, which are evident in the plume snapshots as well as their ensemble means shown in Fig. 2.4.

Figure 2.5 illustrates the differences between the synthetic measurements for AVIRIS-NG and HyTES over the same plume for three different wind speed conditions. Because the column averaging kernel of the HyTES is close to zero near the ground, the synthetic measurements for HyTES miss parts of the plume near the surface and detect only the parts of the plume that have risen high enough. This is consistent with the averaging kernels shown in Fig. 2.2. This is especially apparent for the case of high wind speed where the majority of the CH₄ is advected horizontally, resulting in a plume remaining near the ground. The result in Fig. 2.5 is in accord with the comparison between the observed AVIRIS-NG and HyTES scenes in Fig. 2.1 during the first overpass. This potentially indicates that the plume at this time remains mostly near the ground, which may not always happen in the same way for the coal mine venting shaft, which is emitting above the ground surface. The insensitivity of

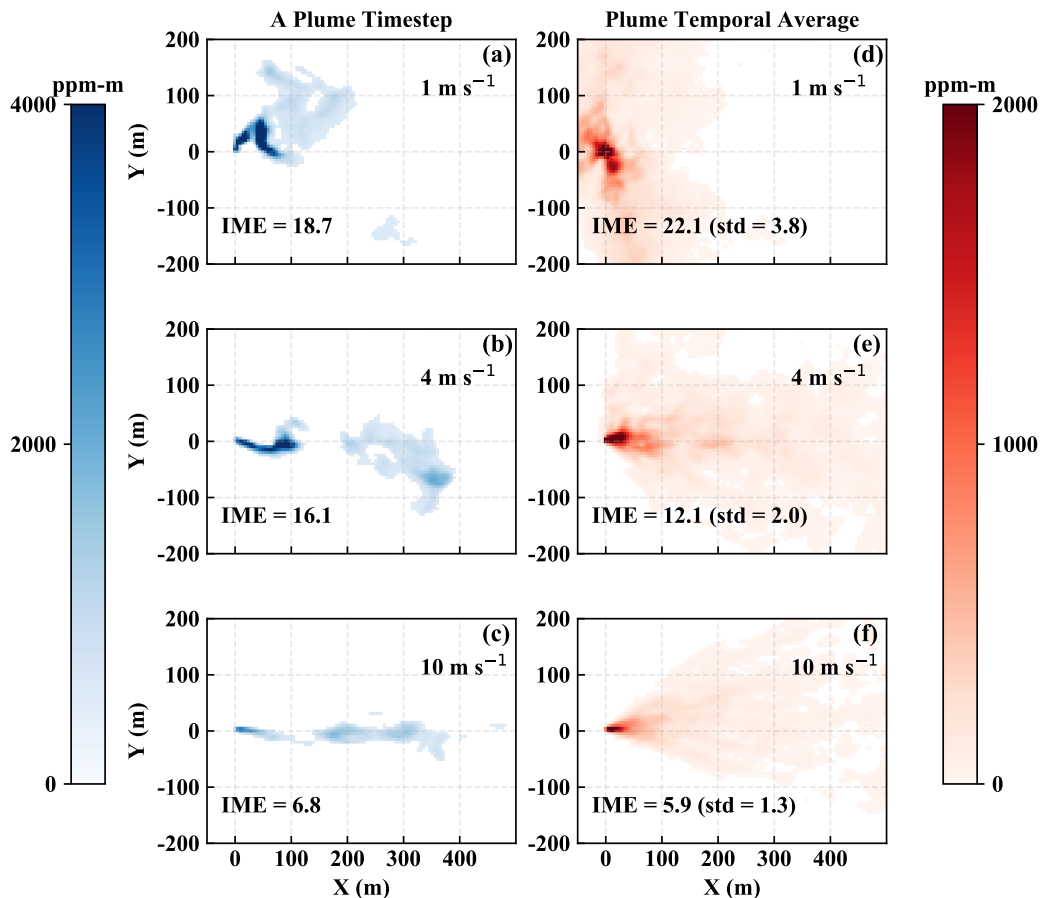


Figure 2.4: (a–c) Snapshots of simulated plumes under wind speeds of 1, 4, and 10 m s⁻¹, respectively. (d–f) Time-averaged plumes from 60 time steps under the geostrophic wind speeds of 1, 4, and 10 m s⁻¹, respectively. All with a flux rate of 300 kg h⁻¹ and detection threshold set to 500 ppm m⁻¹. All are based on AVIRIS-NG averaging kernels. The IME is calculated over the entire scene and is in kilograms. Note that the temporal averages do not reach a true ensemble average as sample sizes are finite (i.e., the average still exhibits fine structure).

HyTES near the ground makes it complicated to locate the source accurately, and there are additional uncertainties in the methane retrievals associated with averaging kernels that vary with environmental conditions (Kuai et al., 2016). The advantage of the HyTES instrument, on the other hand, is the fact that in principle it can operate at night when there is no sunlight, which is a prerequisite for the AVIRIS-NG instrument. For AVIRIS-NG, the total column CH₄ enhancement in each pixel is also better constrained given the averaging kernel is approximately one throughout the column. For these reasons, we proceed to focus only on AVIRIS-NG results in the current study, while we will study the information content of joint measurements

in the future.

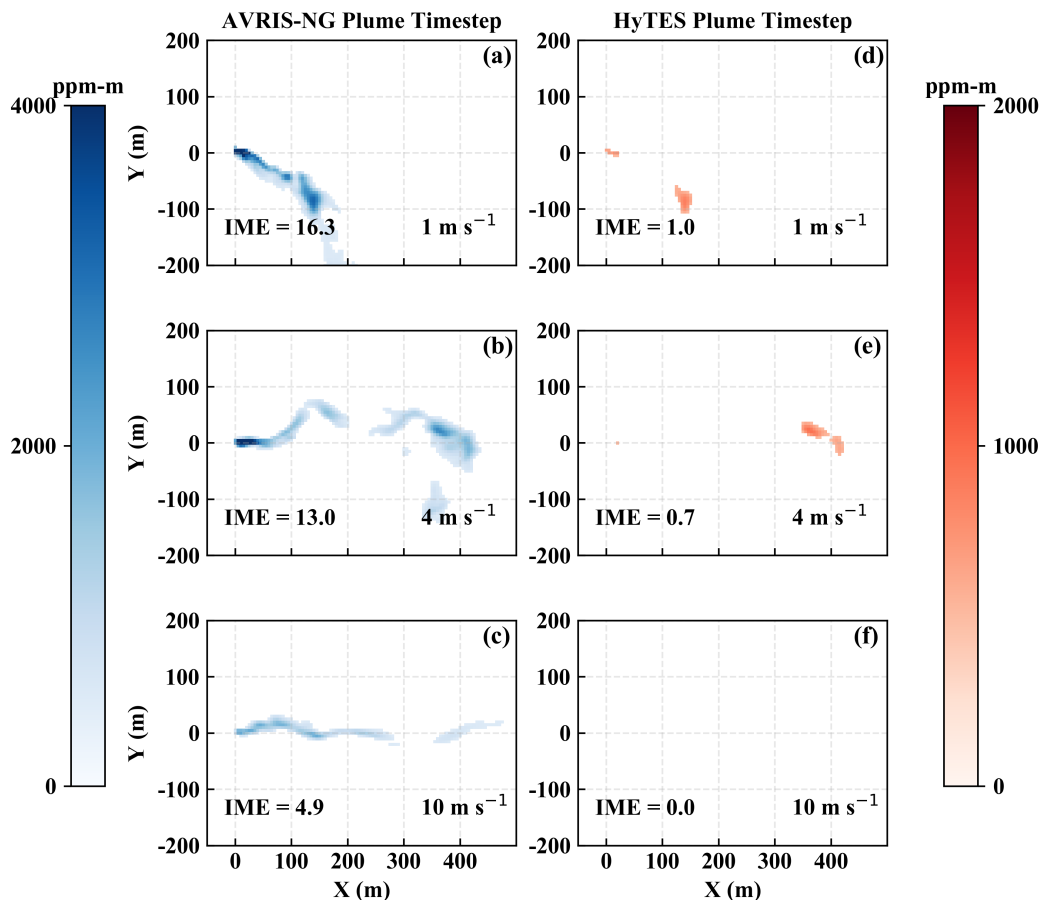


Figure 2.5: (a–c) Snapshots from simulated plumes under 1, 4, and 10 m s^{-1} , respectively, when applying the AVIRIS-NG instrument column averaging kernel. (d–f) Snapshots from the exact same plumes as in (a–c), respectively, but applying the HyTES averaging kernel. The flux rates are all 300 kg h^{-1} and the detection threshold is set to 500 ppm m^{-1} . The IME is in kilograms.

Multiple LES runs from a combination of typical point-source flux rates and wind speeds enable us to quantify the relationship between the actual source rate and the resulting IME for a given wind speed. This gives us the first step to invert the flux rate. Furthermore, we show how different wind speeds affect this relationship for the flux inversion. The output from the LES gives us not only the IME but also the spatial distribution of the plume snapshots that correspond to a given pair of flux rate and wind speed. We analyze how the morphology of the plumes is linked with the underlying background wind speeds. This helps us understand how we can use the remotely sensed airborne imagery of the plume to predict the wind, and thus ultimately the flux rate, together with its associated errors.

In our analysis, we primarily refer to the wind speed in each scene from our model runs by using the geostrophic wind speed, as opposed to the instantaneous wind at 2 m (U_2) or 10 m (U_{10}) above ground which is usually used in literature. For reference, the average U_{10} across the horizontal domain in our run ranges approximately from 0.4 to 0.7 of the background geostrophic wind speed in the run. The main reason is that our output snapshots from each LES run is written out every minute; thus we only have the information of the U_{10} and the plume structure at every minute, which can change rapidly in direction and magnitude. However, the overall structure of the plume at any given instance could be influenced by the average wind cumulatively from the past minute. The constraint on the output that we have makes it ambiguous to choose what values of near-surface winds should be applied when making the prediction of the flux rate from the spatial structure of a plume snapshot. We thus resort to using a background wind speed, which, in turn, is one of the key governing drivers for U_{10} itself. While using the large-scale background wind speed might not be as accurate as the ideal case of having continuous U_{10} output, it provides a robust correlation with the overall pattern of the plume. In other words, in the following, we are using the shape of the plume to predict the value of background geostrophic wind speed that underlies the wind that has driven CH_4 from the point source into the detected plume over that geographical location, and we use that background wind speed to quantify the source rate.

Source Flux Rate and the IME

For each wind speed and flux rate, we have 60 snapshots of methane plumes from the LES model output, with a temporal interval of 1 min. We can thus directly compute the mean and the standard deviation of the IME across these snapshots. Although the shape of a plume can vary strongly in time, the IME is relatively stable, varying only within approximately 20 % among snapshots under the same wind speed and flux rate. This emphasizes the benefit of using the IME to characterize methane in the scene because the total sum of the gas in the scene remains approximately the same regardless of the advection of methane from one pixel to another with time. This can potentially induce less uncertainty compared to other mass balance approaches where the measurements are commonly location dependent. The mean values corresponding to various background wind speeds and flux rates are plotted in Fig. 2.6. The uncertainties reflect the standard deviations of the IME within all 60 temporal snapshots.

The plot of the IME and flux rate at different wind speeds reveals two noticeable

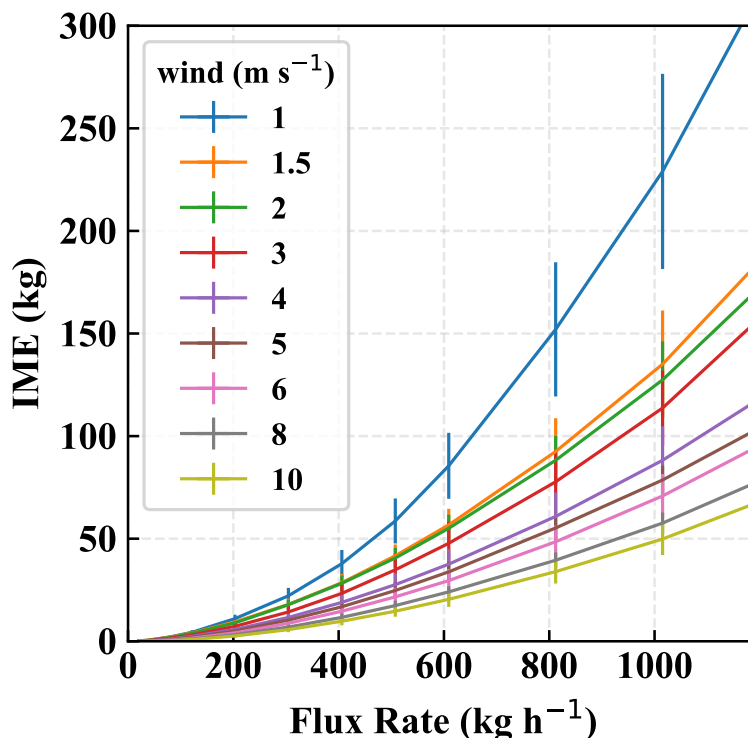


Figure 2.6: Mean and standard deviation of the IME associated with a range of flux rates under various background wind speeds from 1 to 10 m s^{-1} . The detection threshold is 500 ppm m^{-1} .

findings: as expected, there is a significant dependence of the relationship between the IME and flux rate on wind speed; but there is also a nonlinearity, which has been ignored in previous studies. The nonlinearity can be explained from the fact that we impose a detection threshold to mask out the plume. In the absence of a detection threshold, the scaling between flux rate and IME would be perfectly linear, as was assumed in Frankenberg et al. (2016). However, as the fraction of pixels with methane enhancement below the detection threshold varies with flux rate and wind speed, the truncated IME below the threshold can induce a considerable nonlinearity. The stronger the flux rate, the higher the number of pixels above the threshold used to calculate the IME. Figure 2.7 illustrates this connection by showing the percentage of the total enhancement that is missed because of specific thresholds. We use three different flux rates (90, 180, 360 kg h^{-1}) to illustrate the nonlinearity. We can see that when the flux rate drops by a factor of 2, the missing amount does not necessarily decrease by the same factor. How the IME is scaled up with the flux rate depends on the spatial distribution of the plume: if the methane is

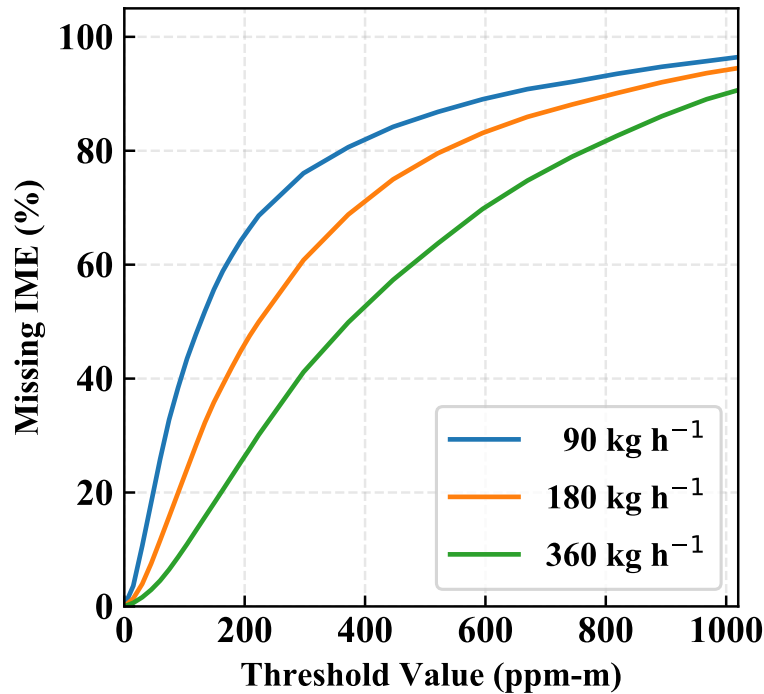


Figure 2.7: Missing IME, shown as a percentage, for different ppm m^{-1} threshold values. Each curve corresponds to a prescribed source flux rate. The flux rates are incremented by a factor of 2.

concentrated in a small area, then it is more likely that a stronger flux rate will make the column enhancements exceed the threshold, as opposed to when the plume is more dispersed, in which case some pixel enhancements will be too diluted to be detected even at a strong flux rate. This is the primary reason why the IME varies with the flux rate with different degree of nonlinearity at different wind speeds as found in Fig. 2.6. The background wind speed is the integral component that drives the spatial distribution of the plume and correlates the IME with the flux rate. This means that in order to achieve a reliable flux inversion, both the IME and the effective wind speed over the scene of the point source must be known.

The key question in our study is the following: can we predict the underlying background wind speed associated with the observed plume by its spatial characteristics rather than by relying on ground measurements or reanalysis data? This is investigated in the following section.

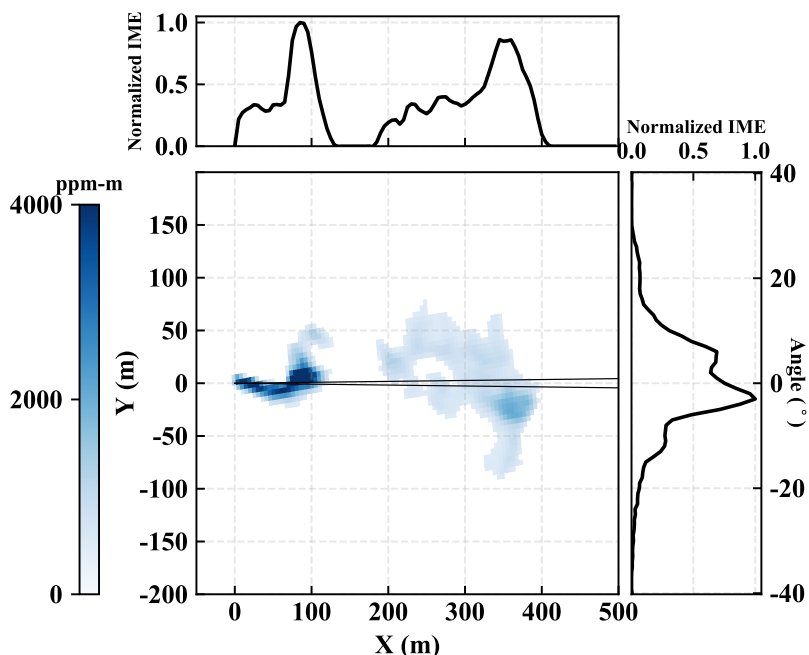


Figure 2.8: A rotated plume snapshot from a run of 4 m s^{-1} background wind speed and 300 kg h^{-1} flux rate with its angular distribution of IME across the plume (right) and its Cartesian distribution of IME along the plume (top). The two black lines denote an angular bin of 0.5° that sweeps through the 2-D plume to construct the angular distribution.

Wind Speed and Plume Morphology

As can be seen in Fig. 2.4, the spatial distribution of the plumes varies under different wind speeds. Visually, the shape of simulated CH_4 plumes provides qualitative intuition on the origin, wind direction, and relative strength of the background wind speed. At a higher wind speed, plumes tend to be more elongated, whereas at a lower wind speed, plumes tend to be more spread out around the origin. We quantify the characteristics of the plume by first constructing an angular mass distribution for each snapshot: we count the mass within the angular bin size of 0.5° sweeping across the scene with the center at the origin. We then find the angle at which the mass of methane splits into a 50% ratio and define that as the main axis of that plume snapshot. The plume snapshot is then rotated such that its main axis aligns with the x coordinate. We can then plot the angular distribution across the plume as well as the Cartesian distribution along the plume, as illustrated in Fig. 2.8, for every single snapshot. This procedure allows us to find the ensemble-averaged plume distributions for a particular wind speed where the ensemble members consist of the rotated snapshots from all available time outputs in the model runs at various flux

rates in the range of our interest, $10\text{--}1000\text{ kg h}^{-1}$.

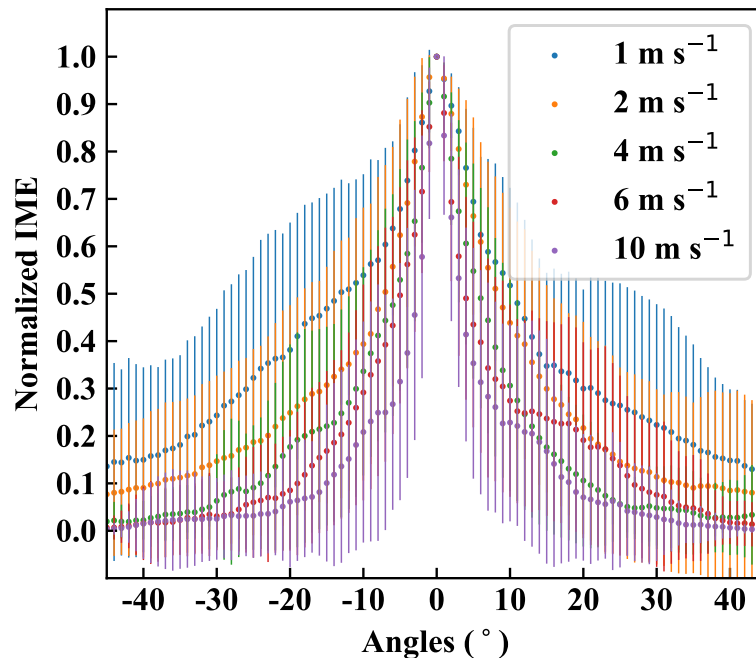


Figure 2.9: Ensemble-averaged angular distributions of the plume, averaging over all available time steps at various flux rates. Different colors represent different wind speeds. Each distribution is normalized by its maximum value. The vertical bars represent 1 standard deviation of the normalized IME at a given angle across all snapshots.

Figure 2.9 shows that the angular distributions of the plume can be distinguishable under different wind speeds. Evidently, the angular distribution of the plume at highest wind speed of 10 m s^{-1} is narrower than the rest on average, and the angular spreading becomes increasingly wider for lower wind speeds. Motivated by this finding based on the average distribution, we quantified the relationship between the angular spreading of the plume and the wind speed. For each snapshot, we calculated the cone width of the plume defined as the angles between the 10th and the 90th percentiles from its angular mass distribution. The mean and the standard deviation of the cone width corresponding to a given wind speed were then computed from an ensemble of 60 temporal snapshots and various flux rates. The result of this analysis is plotted in Fig. 2.10 and shows a monotonically decreasing cone width with respect to wind speed. Our choice of parameterization in Fig. 2.10 is an exponential fit, which adequately captures the present relationship without overfitting. This result illustrates that the cone width is a metric that can differentiate wind speeds based

on using only the spatial distribution of the plume. This finding, together with the variation of IME with flux rate (Fig. 2.6), can therefore provide flux inversion without the need for ground measurements. The next section describes steps for estimating the flux rates and their associated uncertainties.

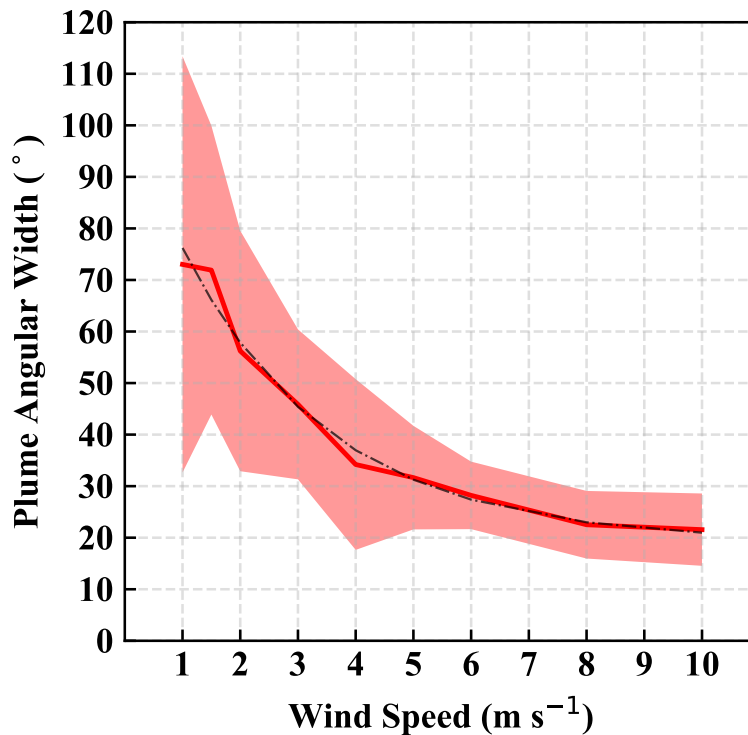


Figure 2.10: Relationship between the wind speed and the associated cone width averaged over snapshots and flux rates. The dotted black curve represents the best fit by an exponential function. The shaded area represents 1 standard deviation from the mean plume angular width for each wind speed.

Flux Inversion and Error Analysis

Based on the IME and plume morphology of any given scene, we can estimate the flux rate. First, according to Fig. 2.6, for a given value of the IME observed in the scene, we can find what the possible range of fluxes is for each wind speed from the lower and upper estimate of 1 standard deviation. We can then parameterize this relationship between the flux rate and the wind speed for this particular value of the IME. An example for the case of the observed IME of 50 kg is demonstrated in Fig. 2.11. Secondly, based on the spatial distribution of the plume in the scene, we can follow the procedure to construct the angular mass distribution. Based on Fig. 2.10, using an angular width measured from the plume, we can predict the wind

speed from the fitted curve. The associated uncertainties of the wind speed are approximated by the lower and upper estimate of 1 standard deviation. We assume that, by projecting a value of plume width onto the corresponding range of wind speeds within 1 standard deviation range, we obtain uncertainties for predicted wind speed that approximately represent 1 standard deviation error for the wind speed distribution. The wind speed and its uncertainty can hence be translated into the estimate of the mean flux rate as well as the corresponding uncertainties from the relationship of the flux rate and wind speed, as in Fig. 2.11.

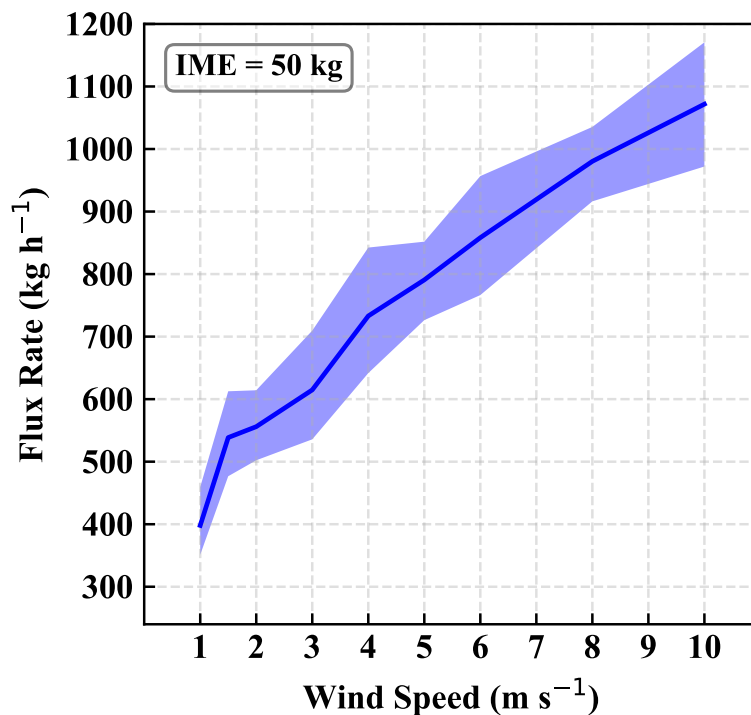


Figure 2.11: Relationship between flux rate and wind speed for 50 kg IME. The shaded area represents 1 standard deviation from the mean flux rate at each given wind speed.

With this approach, we selected 90 random snapshots with random prescribed flux rates and wind speeds. We predict the flux rate from the IME and the spatial distribution of each of plume scene and compare it to its actual prescribed value, as shown in Fig. 2.12. The average of the percentage differences (in absolute terms) between the predicted value and the actual value for single-point-source predictions is approximately 30%. The χ^2 value from the predictions in Fig. 2.12 is 3.84, suggesting that the error variance may tend to be slightly underestimated for an individual-point-source prediction.

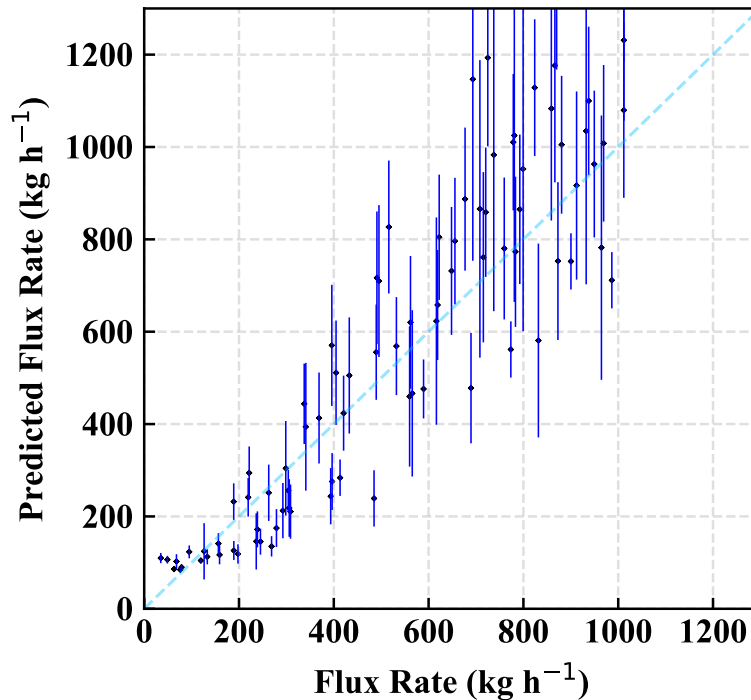


Figure 2.12: Comparison between the prescribed flux rate in the model run and the predicted flux rate based on our method of using the IME and the angular width of plume in a given scene. The error bar represents uncertainties associated with the prediction of an individual point source.

Nevertheless, the results shown in Fig. 2.12 demonstrate that this method permits estimation of the total emission flux rate. Most importantly, accounting for nonlinearities and variable wind speed helps to avoid systematic biases. Thus, the method employed here can minimize systematic errors that could be induced by assumptions on wind speed. To verify this point, we performed an aggregation analysis by bootstrapping 30 plumes out of 500 plumes of various flux rates and wind speeds, with 3000 repetitions. The sample size of 30 is chosen arbitrarily, but is large enough to represent a situation for the estimation of total fluxes from a region. The comparison between the predicted and the actual total flux aggregated over 30 plumes is shown in Fig. 2.13. The predictions lie close to the actual aggregated fluxes, as demonstrated by the concentration of points near the one-to-one line in Fig. 2.13, implying that there are no significant systematic biases in our method. The mean of absolute differences from all these aggregates is 5.1 % with a standard deviation of 3.9 %, while the average of all differences (negative and positive) results in 2.9 % with the standard deviation of 5.9 %.

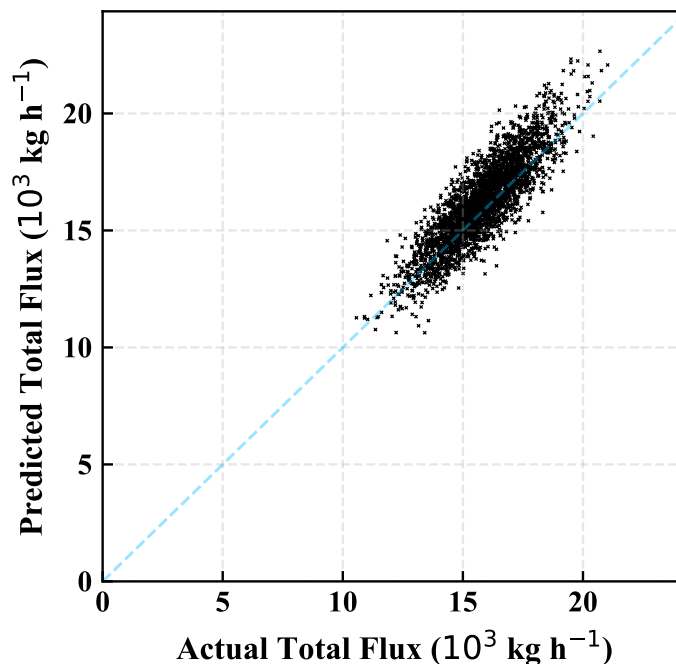


Figure 2.13: Comparison between the predicted and the actual total flux of 30 plumes from 3000 bootstrap rounds.

To further demonstrate the validity of this method, we applied it to a controlled-release experiment from a natural gas pipeline located at Victorville, CA (34.8° , -117.3°), on 11 October, 2017, with a flux rate of $89 \pm 4 \text{ kg h}^{-1}$. Based on a sample of the actual AVIRIS-NG scene over the source location (Fig. 2.14), we calculated the IME and constructed the angular distribution of the plume to obtain its width to deduce the wind speed. The geostrophic wind speed is predicted to be $3.3 \pm 1.2 \text{ m s}^{-1}$, compared to the surface sonic wind at the source measured at 1.6 m s^{-1} . This is consistent given that geostrophic wind is typically about 1.4–2.5 times higher than the surface wind speed in the LES output. We used this deduced wind speed to predict the flux rate and its associated error as described at the beginning of this section. The value that we predict is $118 \pm 30 \text{ kg h}^{-1}$, consistent with the actual release flux within the error estimate.

Furthermore, we applied our method to multiple overflight AVIRIS-NG scenes from Fig. 2.1. The fitted flux rates are within a consistent range: 1275, 1033, 1397, and 926 kg h^{-1} , respectively. The mean of these estimates is thus 1158 kg h^{-1} , and the standard deviation is 187 kg h^{-1} .

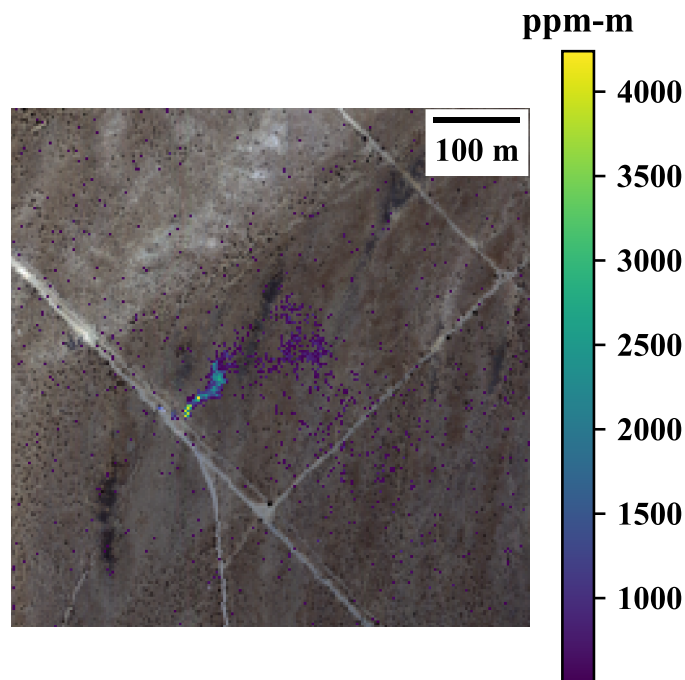


Figure 2.14: An observed AVIRIS-NG scene in a controlled-release experiment from a natural gas pipeline located at Victorville, CA (34.8° , -117.3°), on 11 October 2017 with the flux rate of $89 \pm 4 \text{ kg h}^{-1}$.

Sensitivity Analysis for Different Heat Fluxes

In our LES simulations for this study, we primarily set the sensible and latent heat fluxes to the typical condition during the Four Corners field campaign. Changing the condition of these surface heat fluxes can potentially affect the vertical structure of the simulated plumes and the dynamics of the plumes in time. Nevertheless, our method involves the column-integrated enhancement, and hence is not significantly impacted by the surface heat fluxes. To verify this point, we performed the sensitivity analysis by running additional LES experiments with a different combination of sensible and latent heat fluxes (SH and LH, respectively): (1) $\text{SH} = \text{LH}$ (220 W m^{-2}) and (2) SH (200 W m^{-2}) $<$ LH (400 W m^{-2}). These two additional scenarios contrast with the typical condition that was previously used, i.e., SH (400 W m^{-2}) $>$ LH (40 W m^{-2}), and cover a common range of surface heat flux conditions. The background wind speed is kept the same as 4 m s^{-1} . The results from our runs are demonstrated in Fig. 2.15, where the relationship between the IME and flux rate is found to be approximately the same, remaining within 1 standard deviation error from the original scenario in the previous analyses. This implies that the uncertain-

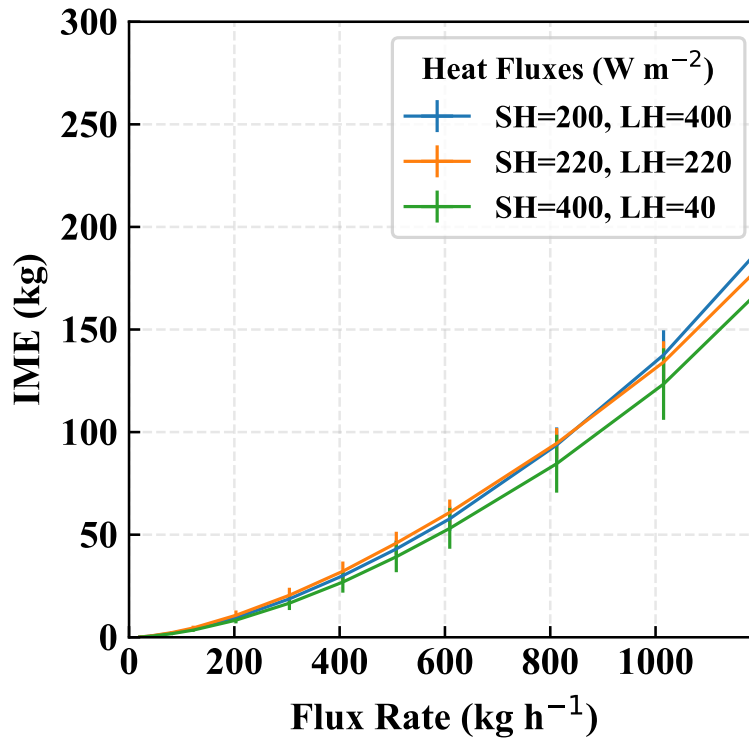


Figure 2.15: Relationship between the IME and flux rate under different sensible and latent heat fluxes of 200 and 400 W m^{-2} (blue), and 220 and 220 W m^{-2} (orange), compared to the original simulation sensible and latent heat fluxes of 400 and 40 W m^{-2} (green). All cases are under the wind speed of 4 m s^{-1} . The detection threshold was 500 ppm m^{-1} .

ties associated with the change in these conditions will not significantly impact our method and are captured well with the range of errors we have analyzed.

2.8 Discussion and Conclusion

In this study, we showed that Gaussian plume modeling cannot be used for a meaningful comparison with observed methane plumes from a point source. Thus, large eddy simulations (LESs) were used to generate realistic synthetic measurements of methane plumes under different background wind speeds and source flux rates. This allowed a comparison of the performances of two considered instruments, one measuring in the shortwave infrared (AVIRIS-NG) and the other in the thermal infrared (HyTES), resulting in widely different vertical sensitivities towards methane enhancements. The AVIRIS-NG was found to provide an unambiguous identification and quantification of the methane source as it is sensitive to methane throughout the air column. While the HyTES instrument has the potential for nighttime observations, variations in the integrated methane enhancements depended highly on vertical plume structure, rendering the interpretation more challenging. While we attempt to make use of the vertical information in the future, we focus this study on results from the AVIRIS-NG synthetic plume measurements. Using the IME method and a large ensemble, we derived the relationship between the detected IME of a plume and its source flux rate. This relationship is found to be nonlinear because of the device detection threshold, which causes a variable fraction of the true IME to fall below the detection limit. In addition, the inversion of IME to an accurate flux rate depends strongly on the wind speeds during the measurements. This finding is expected and confirms the significance of wind speeds on the methane point-source flux estimations from remote sensing data. To study whether we can gain additional information from the plume shape itself, we performed an analysis on a large ensemble of plume snapshots from wide-ranging source flux rates and wind speeds. We found that the angular width of the plume negatively correlates with the wind speed, allowing us to constrain the effective wind speed from the shape itself. The angular width is defined based on the plume angular distribution around its main axis and is found to be effectively independent of the source rates.

Using the relationship between the IME and the flux rates for different wind speeds together with the connection between plume shape and the wind speed, we can disentangle the source flux rate based on an observed snapshot of the plume which provides both the IME and the spatial distribution. Our error analysis of this method applied on randomly generated snapshots of various flux rates in the range of $10\text{--}1000\text{ kg h}^{-1}$ showed an error of around 30 % on average for an individual point-source estimate. Given that point sources are highly uncertain and also fluctuate in time, this single measurement error appears acceptable. More important

than single measurement precision is accuracy for larger ensemble averages, which informs regional emission estimates. Thus, we also performed an error analysis for aggregated flux estimates from 30 plumes. We used bootstrap sampling and found the aggregation error estimate to be in the range of less than 10 %. This provides a significant improvement from other preexisting approaches that rely on wind data, for which reliable meteorological reanalysis data might not be available at high spatial resolution everywhere.

Furthermore, our method is validated by the application of this method on an actual scene from a controlled-release experiment from a natural gas pipeline in 2017, which demonstrated an error of 32 % from the controlled flux rate of 89 kg h^{-1} , a notable accuracy given the simplicity of our algorithm that does not require wind speed data. This provides added value in quantifying methane-point-source emissions especially in locations where atmospheric reanalysis products and surface meteorological observations are not available.

It should be noted that altering the device detection threshold level in our synthetic modeling to higher values does impact the robustness of the correlation between the plume width and the wind speed. In this study, we set the threshold to 500 ppm m^{-1} to match the capabilities of the current instrumentations. Future instruments with improved gas sensitivity (Thorpe et al., 2016) will likely improve our ability to estimate emission rates. Repeat overflights that result in multiple snapshots of the same source can also further reduce uncertainties from transient variations of the plume due to turbulence. Another aspect is that our current LES does not yet model direct emission that could be released at a height above the ground. Incorporating this feature into our future analysis may provide even more realistic methane plume simulations. Despite these limitations, this current study is a first step proving the potential of the method.

In this study, we have demonstrated the ability to estimate flux rates of methane point sources based solely on the remotely sensed column methane enhancement without the need for ground measurements or weather reanalysis data. This method could be applied to recent large-scale flight campaigns to improve previous emission rate estimates. This also has immediate implications for future AVIRIS-NG flight campaigns, in particular over parts of the world lacking available wind data. The methodology described in this study could also be applied to anticipated satellites that will provide methane measurements at finer spatial resolutions than currently available. A path towards an improved understanding of the regional methane budget

as well as insights into methane source distributions by categories is made possible.

METHANET – AN AI-DRIVEN APPROACH TO QUANTIFYING METHANE POINT-SOURCE EMISSION FROM HIGH-RESOLUTION 2-D PLUME IMAGERY

This paper is under review in:

Jongaramrungruang, S. et al. (2021). “MethaNet – An AI-driven approach to quantifying methane point-source emission from high-resolution 2-D plume imagery”. In: *Remote Sensing of Environment*, Under Review.

3.1 Abstract

Methane (CH_4) is one of the most important anthropogenic greenhouse gases with a significant impact on the Earth’s radiation budget and tropospheric background ozone. Despite a well-constrained global budget, quantification of local and regional methane emissions has proven challenging. Recent advancements in airborne remote sensing instruments such as from the next-generation Airborne Visible/Infrared Imaging Spectrometer (AVIRIS-NG) provide 2-D observations of CH_4 plume column enhancements at an unprecedented resolution of 1–5 m over large geographic areas. Quantifying an emission rate from observed plumes is a critical step for understanding local emission distributions and prioritizing mitigation efforts. However, there exists no method that can predict emission rates from detected plumes in real-time without ancillary data reliably. In order to predict methane point-source emissions directly from high resolution 2-D plume images without relying on other local measurements such as background wind speeds, we trained a convolutional neural network model called MethaNet. The training data was derived from large eddy simulations of methane plumes and realistic measurement noise over agricultural, desert, and urban environments. Our model has a mean absolute percentage error for predicting unseen plumes under 17%, a significant improvement from previous methods that require wind information. Using MethaNet, a validation against a natural gas controlled-release experiment agrees to within the precision error estimate. Our results support the basis for the applicability of using deep learning techniques to quantify CH_4 point sources in an automated manner over large geographical areas, not only for present and future airborne field campaigns, but also for upcoming space-based observations in this decade.

3.2 Introduction

Methane (CH_4) is one of the most important anthropogenic greenhouse gases in the Earth climate system. Since preindustrial time, the global atmospheric methane concentration has nearly tripled to almost 1900 ppb (Dlugokencky, 2021; Saunio et al., 2020). Its rising atmospheric concentrations coupled with the strong radiative forcing per molecule makes methane the second strongest anthropogenic greenhouse gas overall, after carbon dioxide (CO_2) (IPCC, 2013). In addition, CH_4 enhances both tropospheric ozone and stratospheric water vapor, both of which contribute to additional indirect radiative forcing. Due to its much shorter lifetime compared to that of CO_2 , methane emissions could be a target for reduction efforts to help mitigate climate impacts on a significantly shorter timescale (Montzka et al., 2011b; Prather et al., 2012; Shindell et al., 2012). In fact, the 2018 NASA Decadal Survey has indicated the identification and understanding of methane emissions as one of the top priorities in the efforts to improve future climate projection, and help lead the way in emission reduction (Sciences and Medicine, 2018).

Despite relatively extensive studies on the total global CH_4 emissions approximation, regional and local emission estimates have been more challenging due to uncertainties in the understanding of individual emissions processes and categories, and lack of sufficiently fine resolution observations that can also simultaneously cover large geographical areas. This hinders the ability to conduct mitigation efforts in the most effective manner since policy and remedy actions often take place at regional and local scales. Since point sources are prevalent among some of the most important emission sectors such as coal mining and oil and gas industry (Brandt et al., 2014; Duren et al., 2019), improved measurements of CH_4 point sources are integral to improving understanding of local and regional emissions in terms of emission rates and categories distribution.

In the past decade, advancements in space-based CH_4 retrieval techniques from satellite observations such as the SCanning Imaging Absorption SpectroMeter for Atmospheric CHartographY (SCIAMACHY) and the Greenhouse gases Observing SATellite (GOSAT) have enabled a top-down constraint on global CH_4 emissions (Frankenberg et al., 2005a; Frankenberg et al., 2011; Kort and Frankenberg, 2014; Parker et al., 2011; Parker et al., 2015; Turner et al., 2015). However, due to their coarse spatial resolutions, their measurements do not distinguish magnitudes of different anthropogenic sources – information critical for accurately identifying the causes of changes in atmospheric CH_4 concentration and its consequences. The

TROPOspheric Monitoring Instrument (TROPOMI) with a spatial resolution of a few kilometers has been shown to be capable of identifying regions of high emissions, but the measurements are not yet at a level where local sources can be identified and mitigated directly (Gouw et al., 2020; Hu et al., 2018). Surface monitoring networks, on the other hand, provide accurate and precise in situ measurements of CH₄, but are sparse in coverage. Oil and gas facilities sites with significant emissions, for example, often have limited access for measurements resulting in their emissions accounted for by inventories-based approach that are likely underestimated (Brandt et al., 2014; Hsu et al., 2010; Kort et al., 2008).

One potential to fill this gap is airborne imaging absorption spectrometry, using the same techniques as in satellite remote sensing to quantify CH₄ plumes (Thorpe et al., 2017). This technique has opened the way for quantitative CH₄ measurements at sufficiently high resolution needed to differentiate various local sources over large areas at regional scale (Duren et al., 2019; Frankenberg et al., 2016). Using absorption features of CH₄ in the short-wave infrared around 2.3 μm , column integrated CH₄ concentration can be retrieved at a spatial resolution well below 5 m. This enables the generation of 2-D methane column enhancement maps, which are used for the detection of CH₄ point sources from airborne spectrometers such as the next-generation Airborne Visible/Infrared Imaging Spectrometer (AVIRIS-NG) (Cusworth et al., 2021; Thorpe et al., 2014; Thorpe et al., 2017). By now, studies have utilized this technique for several field campaigns in California and the Four Corners regions, where a total of more than 500 strong point sources have been detected (Duren et al., 2019; Frankenberg et al., 2016). Despite the progress in the detection algorithm of methane plumes, high uncertainties still exist in converting the observed concentration fields to source flux rates due to varying boundary layer conditions (turbulence and wind speed), presence of spectral interferences, and sensitivity of the flux inversion to complex plume structures. These uncertainties can be up to 100 % for individual plumes (Duren et al., 2019). Systematic covariances in the biases across individual source estimates can also propagate to aggregated regional estimates. Thus, we have to focus on bias-free flux inversions, realizing that certain precision errors from individual plumes are unavoidable. Assuming, for instance, that a single wind speed from reanalysis data for a specific flight campaign date would directly propagate into estimates of regional total fluxes since a potential wind-speed bias would be identical for all individual plumes. Randomizing biases for single plumes is thus a pre-requisite to minimize biases aggregated emissions estimates.

Many flux inversion methods have been proposed such as the Gaussian plume inversion (Bovensmann et al., 2010; Krings et al., 2013), source pixel estimate (Jacob et al., 2016), cross-sectional flux estimate (Cambaliza et al., 2015; Cambaliza et al., 2014; Conley et al., 2016), and residence time of methane plume enhancement (Duren et al., 2019; Varon et al., 2018). All of these techniques, however, require the knowledge of an effective local wind speed. This hinders fast and accurate flux inversions since in situ wind measurements cannot be planned when the location of the plume is not known a priori. One alternative to acquire wind data is from weather station or reanalysis data, but these are only available at spatial and temporal resolution that is too coarse. Reliance on this wind data may cause a correlated bias in all individual plume flux estimates. In the near field, plumes often exhibit fine structures at a few tenths to hundreds of meters with its dynamics changing within seconds to minutes whereas wind data is typically provided at lower resolution, such as from a 3-km resolution as an hourly average (Benjamin et al., 2016). Due to these limitations, accurate flux inversions of point sources have been challenging. Any improvement in flux inversion depends on the ability to constrain the effective wind speed during which the plume is developed locally. Jongaramrungruang et al. (2019) tackled this challenge by utilizing the 2-D plume morphology to constrain corresponding wind speed and thus flux rate. The study provided evidence that the morphology of methane plumes, as observed from remote sensing images, contains useful information about the background wind speed during the flight overpass, which, in turn, is a critical component of predicting accurate flux estimates. In that work, a plume angular width was constructed as a simple metric to represent the geometry of observed methane plumes. Essentially, the complex 2-D pattern of the plume was simply reduced into one dimension, which was an ad hoc choice. It was an intuition-based approach that limited the exploitation of details in the fine structure.

However, the full spatial structure of the plume morphology can potentially be utilized such that emission rates are predicted at even higher accuracy, as well as in a more automated and objective manner. Modern machine learning techniques are designed for problems like this task. Convolutional Neural Network (CNN) is a model architecture that has shown tremendous success in image recognition tasks (He et al., 2016; Krizhevsky et al., 2012; Simonyan and Zisserman, 2015; Szegedy et al., 2014). It has been shown to be capable of learning relevant spatial patterns from an image with location invariant features similar to how a human brain understands an image. Here, we built a customized CNN model and applied it to a large training

dataset of methane plumes from Large Eddy Simulation (LES) (Matheou et al., 2014) output at various flux rates, wind speeds, added realistic measurement noise and synthetic random noise, offsets, and rotations. We trained our model, named MethaNet, to predict flux rates directly from 2-D methane plume images. To our knowledge, this is the first time that CNN has been used for a regression task to quantify methane plume emission from 2-D high-resolution imagery.

Section 3.3 illustrates the workflow for simulating realistic 2-D plume images. The methodology on preparing the training and validation dataset, and the details on a CNN architecture are given in Section 3.4. Model performance and error analyses are provided in Section 3.5, followed by concluding remarks in the final section.

3.3 Realistic Plume Simulation

Figure 3.1 shows examples of representative methane plumes from different sectors such as a natural gas storage facility, an oil well, a landfill, and a dairy manure area. Each plume image represents the total CH₄ column enhancement; in each pixel, the enhancement is obtained as a retrieval product using algorithms such as Iterative Maximum a Posteriori – Differential Optical Absorption Spectroscopy (IMAP-DOAS) (Frankenberg et al., 2005b) or matched filter retrieval (Thompson et al., 2015) on the observed radiance measurements. These plumes were observed under different surface and background wind speed conditions. It is evident that they vary in shape and absolute methane enhancements. Sources of various emission rates observed under varying wind speeds would lead to a diverse set of plume spatial distributions. To train a model capable of quantifying an emission rate from a given 2-D image, a realistic modelling of CH₄ plumes is a prerequisite as observed plumes are clearly not Gaussian. The training data consists of synthetic plume images with source emission rates as labels.

The LES was used to generate the time-resolved three-dimensional CH₄ distribution in the boundary layer. This enables a realistic simulation of how methane concentrations from a point source evolve in space, given various wind speeds. The full description of the LES model setup for CH₄ plume emanating from a point source can be found in Matheou and Bowman (2016), with the model parameterization and initialization detailed in Jongaramrungruang et al. (2019). The flow in the boundary layer is driven by a constant geostrophic wind in the x direction, influencing the dynamics of the atmospheric turbulences in the boundary layer resulting in various distinct plume shapes. The dynamics and stability regime of the plumes can be

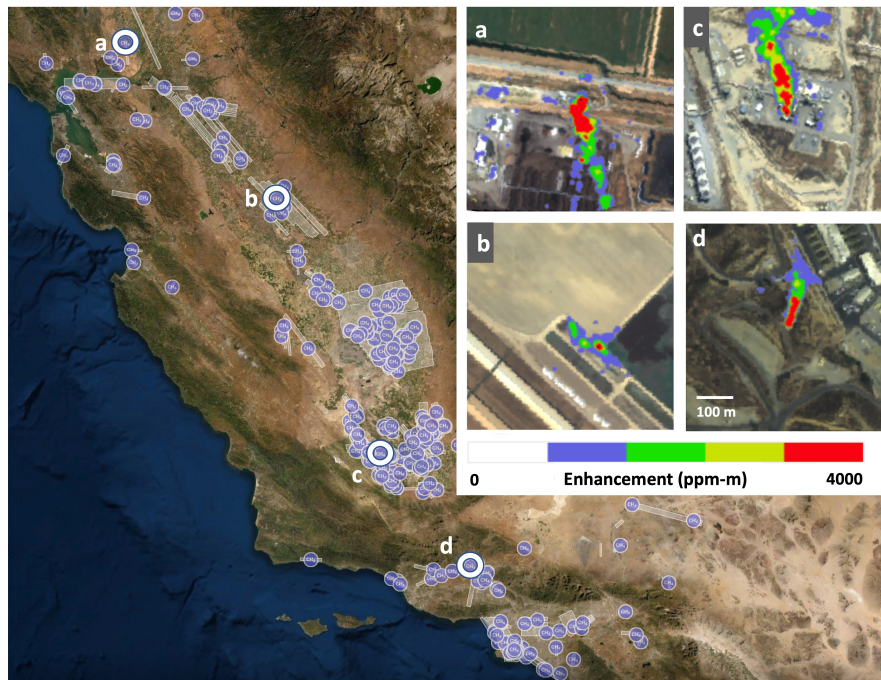


Figure 3.1: A map showing detected methane sources from the California Methane Source Finder project. Background image shows AVIRIS-NG flight lines conducted in 2016 and 2017 (white stripes) and locations of detected CH_4 sources (purple circles). The inset images show examples of methane plume enhancement from AVIRIS-NG observations over (a) a landfill, (b) dairy manure area, (c) an oil and gas facility, and (d) a natural gas storage field.

driven by wind speed as well as other factors such as surface sensible and latent heat fluxes. Previous studies such as Varon et al. (2018) and Jongaramrungruang et al. (2019) have shown that wind speed is the main factor influencing distinct spatial patterns of total CH_4 column as well as the relationship between the total methane amount within a distinct plume and the associated methane flux rate. Since the format of our training data will be an image of total column enhancement in each pixel, we primarily focus on conducting LES experiments with different geostrophic wind speeds ranging from 1 to 10 m s^{-1} , while keeping the surface sensible and latent heat fluxes at 400 W/m^2 and 40 W/m^2 , respectively. This was based on a typical field condition when the Four-Corners campaign was conducted. In each experiment, the 3-D concentration field was extracted every 10 seconds, excluding a 1h period of spin-up time. From the 3-D LES fields per time step, we can create synthetic 2-D enhancement images, similar to actual observations from a given remote sensing instrument. In the case of the AVIRIS-NG, the 3-D field is integrated vertically, weighted with the column averaging kernel of the instrument retrieval, which is near

unity. We outputted a total of 7,000 simulated plumes from our LES experiments. Some examples of simulated 2-D plume enhancement images from our LES runs for various wind speeds are shown in Figure 3.2. Each pixel in the 2-D image is a snapshot in time, representing the CH_4 enhancement expressed in ppm-m which is a typical unit used in the methane detection literature (10 ppm-m is about 1 ppb in XCH_4). The LES snapshots cover a variety of plume morphology that resembles plume observations from field campaigns. As a reference, typical instantaneous winds at 10 m (U_{10}) above the ground during the observation conditions across the California study (Duren et al. 2019) were $0.4 - 9.2 \text{ m s}^{-1}$. In our LES experiments, the values of U_{10} range from 0 to 11.8 m s^{-1} . We believe that these LES experiments cover the majority of possible 2-D plume structures in typical scenarios, but could be easily extended to cover more unique locations.

Any given 2-D image of enhancements at a reference flux rate can be scaled by an arbitrary factor to represent various emission rates. This is a good assumption since the self-buoyancy of methane is negligible once mixed, making enhancements for a model run a linear function of the flux. This allows us to efficiently create synthetic plumes originating from sources spanning orders of magnitudes in flux rates. In this work, we focus on plume emission rates between 0 and 2000 kg h^{-1} , which are the range in which the majority of typical methane point sources were observed in Duren et al. (2019) and Frankenberg et al. (2016). Each of these 2-D images was then augmented by continuous random rotations between -170° to 170° and translations between -30 to +30 pixels, to generate a diverse set of possible plume orientations and center locations. Additionally, superimposed on each image is a noise matrix with the same size as the plume image. The illustration of this synthetic plume generation is shown in Figure 3.3. A simulated realistic plume image consists of two key elements: the LES output that mimics a noise-free realistic spatial distribution of the true total column enhancement at each location, and the measurement noise from a realistic retrieval, as is feasible using AVIRIS-NG. This measurement noise can consist of precision error and bias during the retrieval process from radiance observation to total column enhancement estimates. Since building a full forward model to create an observed radiance from a reflected sunlight and compute the corresponding noise level from the detector is outside the scope of our study, we instead used observational scenes from AVIRIS-NG flight lines that actually contain only background variations with no real plume, but possibly exhibit enhancement within the scenes, to represent potential random and systematic noise within the measurements. Oftentimes, the noise is correlated with

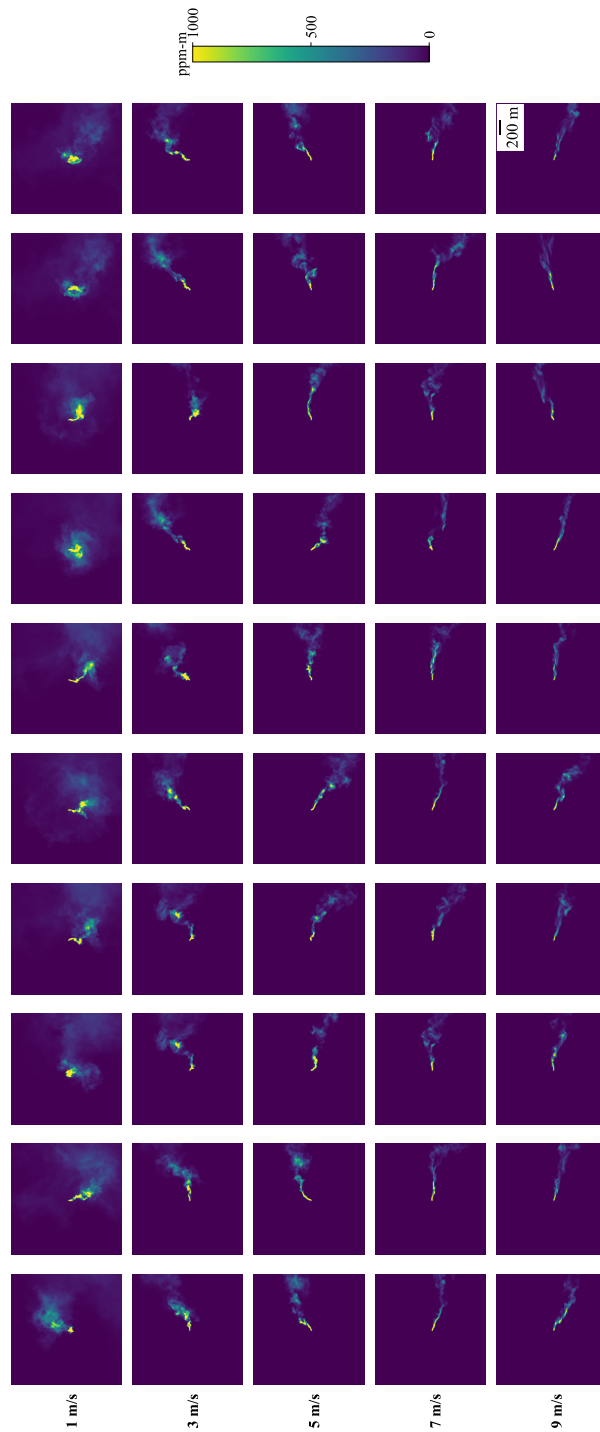


Figure 3.2: Examples of simulated CH₄ plume images from the LES experiments with 1, 3, 5, 7, or 9 m s⁻¹ geostrophic wind speeds (in x-direction) that drive the dynamics of the plumes. Columns represent different random snapshots from each experiment.

surface features such as a lineated road that is unlikely to be part of a real plume. These AVIRIS-NG scenes are what we refer to as realistic background noise. In our work, we applied the realistic retrieval noise obtained from scenes over a variety of surfaces, including urban, desert, and agricultural areas. It is worth noting that using realistic noise is very important as noise over pixels can be correlated and related to surface-methane interferences that cannot be fully eliminated with the current sensors and retrieval processes, as the low spectral resolution such as 5 nm in AVIRIS-NG is still prone to subtle surface interferences. This noise is thus not random Gaussian but exhibits correlated features among adjacent pixels that could potentially be perceived as false positive plumes, representing a challenge for the machine learning problem.

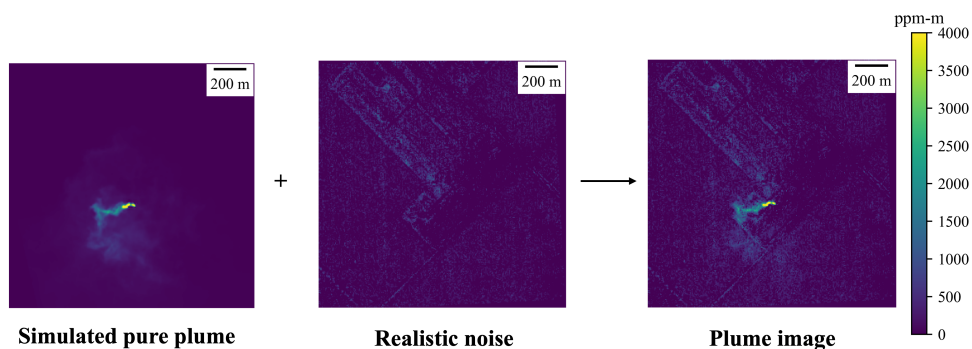


Figure 3.3: An example of a plume image from a simulated plume superposed on a realistic retrieval noise background based on an AVIRIS-NG observation over agricultural area.

3.4 Method

In this section, we outline the setup for training, validation, and test data, as well as provide details on the CNN model architecture used in this work.

Training, Validation, and Test Data

Building a successful neural network model generally requires large data samples. These data are separated into training, validation, and test sets that share a similar distribution, but are distinct from one another. Our training data is a set of images of plumes of different sizes and shapes under various wind speeds and background noise. It is used to learn parameters of a model. The validation data is another set of different images of plumes used to evaluate the performance of our trained model on unseen plumes. It provides a benchmark on how well our model generalizes, which

enables us to tune hyperparameters and choose the best-found model. The test set is the other set of images kept unseen from the very beginning and takes no part in the training and selection of the model. It is only at the very end after a model has been selected when we apply the selected model on images of plumes in the test set to report the final performance of our model. In our study, we randomly assigned 3000 background noise scenes into three buckets, each to be used exclusively in each of the three sets to ensure no data contamination among them.

In our problem, we constructed our training, validation, and test data using two different approaches. In the first setup, the training set only consisted of plume images from the LES runs with wind speeds 1, 3, 5, 7, 9 m s^{-1} . The validation and test set were based on plume images from the LES runs with wind speeds 2, 4, 6, 8 m s^{-1} , which we call scenario 1. This setup enables us to assess the performance of a model that learns features from plumes under certain background wind speeds, and predicts on plumes that are driven by different wind speeds. In another setup, denoted scenario 2, we used plume images from all LES experiments, and randomly assigned images for training, validation, and test data, respectively. In this latter approach, the model learns from plumes under all possible wind speeds such that it can be used to predict plumes under any wind speed condition in the real world. Thus, we also used this model to make a prediction on a few available actual plume observations from a controlled release experiment. We note that in the process of preparing our data, the original LES simulated plume images were assigned exclusively into each training, validation, and test set. No identical snapshot from the LES was used across the sets. The same applies to the AVIRIS-NG noise scenes in our study.

These steps help ensure that the data in the training, validation, and test sets are independent of one another. Within each of these sets, a random augmentation (such as scaling, rotation, and translation) was applied to each plume image. Each augmented plume image was added by a random noise scene (from their corresponding set), which independently also underwent a random augmentation process for rotation, reflection, and translation. Figure 3.4 illustrates the data pipeline for building a training, validation, and test sets. Based on the original 7000 LES plume outputs, we separated approximately 80 % of the scenes into the training set, each of which was augmented into 50 new training images. The remaining 20 % of the LES plume outputs were separated into the validation set (15 %) and the test set (5 %). Each of the images in these two sets was augmented into 10 new validation and test images.

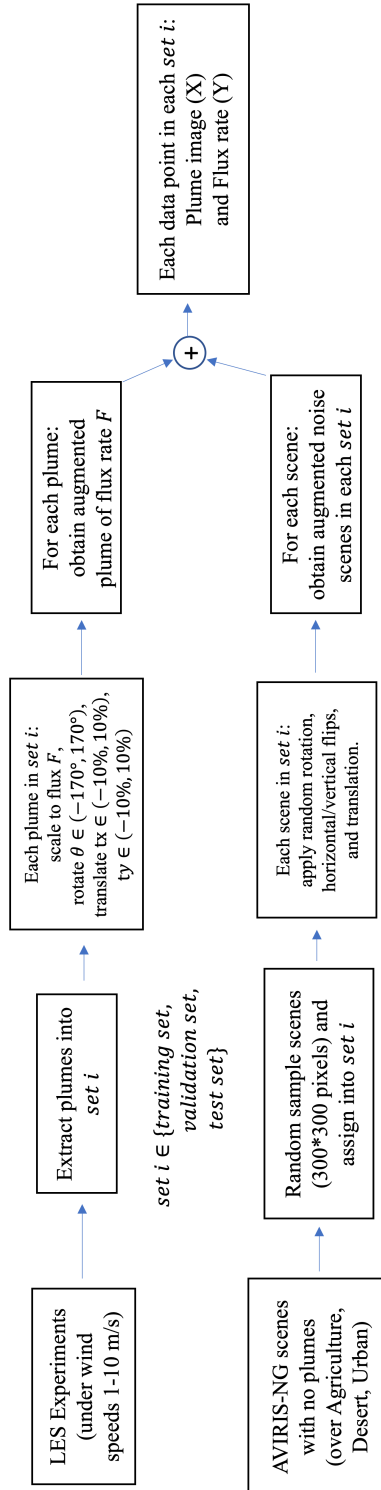


Figure 3.4: An illustration of a data pipeline for pre-processing plume images to be used in training, validation, and test sets.

This is the data setup for scenario 2. In the case of scenario 1, where we trained a model on only “odd” wind speeds, we took half of those already augmented images from the scenario 2 training set that corresponds to “odd” wind speed LES runs to train the model. For the validation and test sets, we used half of those scenes within the validation and test sets from scenario 2 that corresponds to “even” wind speed LES runs. Table 1 summarizes the number of scenes in each data set, according to each scenario.

	Scenario 1	Scenario 2
Training	139500	279000
Validation	5350	10700
Test	1750	3500

Table 3.1: A table showing the number of synthetic CH₄ scenes used in training, validation, and test sets in two training scenarios.

Convolutional Neural Network (CNN) Architecture

Machine learning methods have been used extensively in many fields to predictive problems. One particular model in machine learning that has found a great success in computer vision tasks is CNN (He et al., 2016; Krizhevsky et al., 2012; Simonyan and Zisserman, 2015; Szegedy et al., 2014). It has been the primary building block for tasks such as face recognition, image classification, autonomous driving. Because of its versatility, recently it has been adopted in tackling environmental science-related problems such as gas leak classification and wild fire classification based on remote-sensing images (Kumar et al., 2020; Pan et al., 2020; Wang et al., 2020). However, most of the CNN applications in environmental science have been primarily limited to classification problems. Here, for the first time, we applied CNN to predict methane quantification directly from a 2-D image as a regression task. We develop a customized CNN model based on a basic building block where a convolutional layer is followed by a non-linear activation function, and then by a max pooling layer. This building block is repeated multiple times before combining with a few fully-connected layers. The final layer is an output layer that determines the type of prediction for either classification (a probability for each class) or regression (a scalar value).

Figure 3.5 shows the architecture of our model. In our case, we found an image dimension of 300×300 pixels to be suitable, as it covers a range of 1.5×1.5 km², which can fully capture typical plume dimensions of less than 1 km, but could be

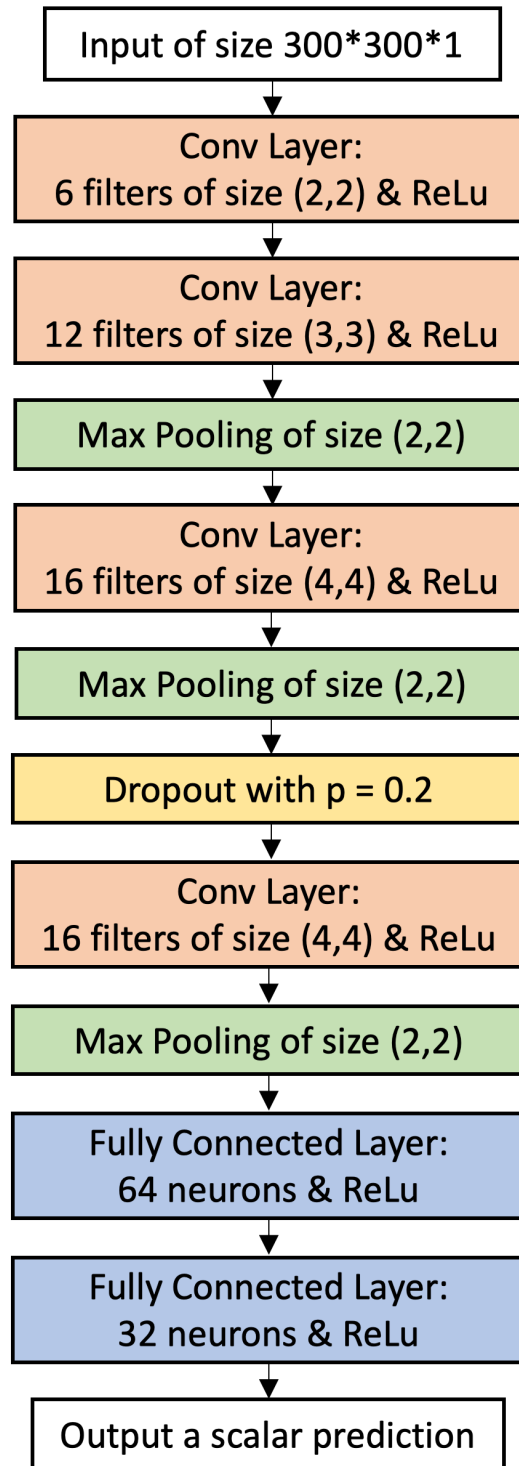


Figure 3.5: The MethaNET CNN architecture.

extended as needed. The input image has only 1 channel representing a value of

retrieved CH₄ enhancement (this value is not bounded by 255 as typical in RGB). We applied a masking threshold of 500 ppm-m to each plume image. This has been chosen as a conservative threshold, close to what we expect as single-measurement precision error from AVIRIS-NG.

The architecture of MethaNet consists of 4 convolutional layers, each with different numbers of filters and sizes. In these layers, the input image is convolved with those filters to provide output for the next layer. Rectified Linear Unit (ReLU) is applied as a non-linear activation function after the convolution. Max pooling layers are also applied after some convolutional layers. A dropout layer is included as a regularization to reduce overfitting. After these combined layers, the output is then flattened and passed to a fully-connected layer with 64 neurons, again with ReLU activation. This is followed by another fully-connected layer with 32 neurons and a ReLU. Finally, the output layer contains one neuron with a scalar output for a regression task to quantify the methane emission rate from the input image.

Although we primarily focused on building this model architecture for a regression task, it is worth noting that this network can be modified for a classification task by changing the output layer to be a softmax layer which has 2 neurons followed by a softmax activation function (i.e. $\sigma(x_i) = \frac{\exp x_i}{\sum_{j=1}^2 \exp x_j}$, where x is an input vector of 2 elements in our case). This layer outputs a probability of whether this image contains a plume or not. We conduct an additional experiment to demonstrate this aspect later in Section 3.5.

3.5 Results

In this section, we show the performance of the CNN model on predicting methane emission rates, according to the two different scenarios for preparing training, validation and test data outlined in Section 3.4. The results are shown in the following subsection. We also provide an analysis on the lower bound of the emission rate at which the model is still able to identify plumes from noise correctly. Performance of the regression model on actual observational scenes from a controlled release experiment, as well as the performance of the model in case of a classification task are given in the subsequent subsections.

Regression Results

Training on “Odd” Winds and Predicting on “Even” Winds

First, the CNN is trained according to the scenario 1 in which our training data comes solely from the LES runs with 1, 3, 5, 7, and 9 m s^{-1} (odd) background wind speeds, while the plumes in the validation, and test sets are derived from the LES with only 2, 4, 6, 8, and 10 m s^{-1} (even) wind speeds. The comparison between the true and predicted fluxes from the test set are shown in Figure 3.5. Generally, predictions align well with the true values as indicated by the concentration of points close to the 1:1 reference line. The mean absolute percentage error of the predictions is 29 % across all plumes. Figure 3.7 shows examples of plume images with high prediction errors. For plumes with emission rates above 40 kg h^{-1} , our model can predict fluxes with a mean absolute percentage error of around 21 %.

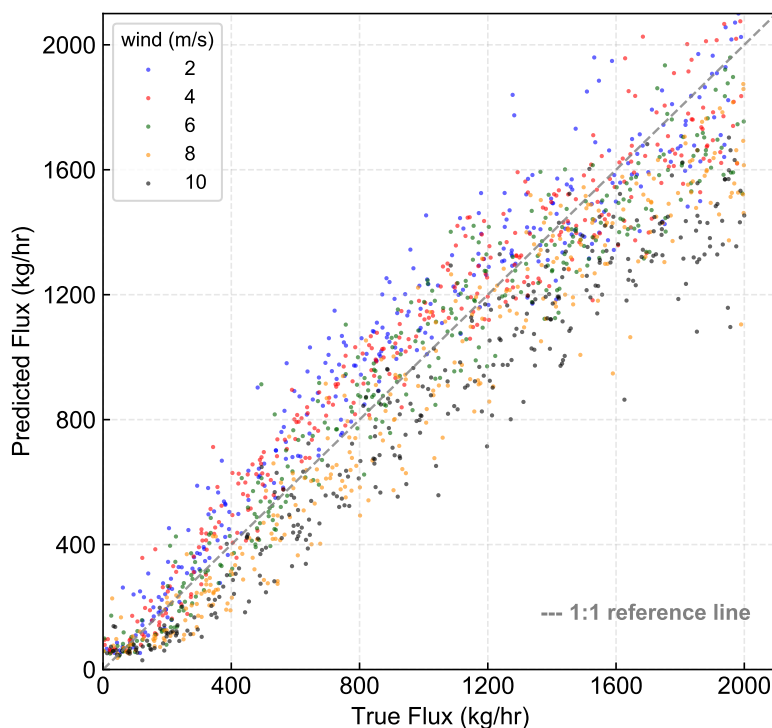


Figure 3.6: A plot showing a comparison between true fluxes and predicted fluxes by MethaNet when trained using only odd wind speeds to predict unseen plumes under even wind speeds. A dashed line shows a 1:1 reference line.

We computed the mean absolute percentage errors for each case of 2, 4, 6, 8, and 10 m s^{-1} wind speeds for plumes above 40 kg h^{-1} . They are 21 %, 17 %, 14 %, 19 %, and 23 %, respectively. Predictions for plumes in the case of 10 m s^{-1} wind speed

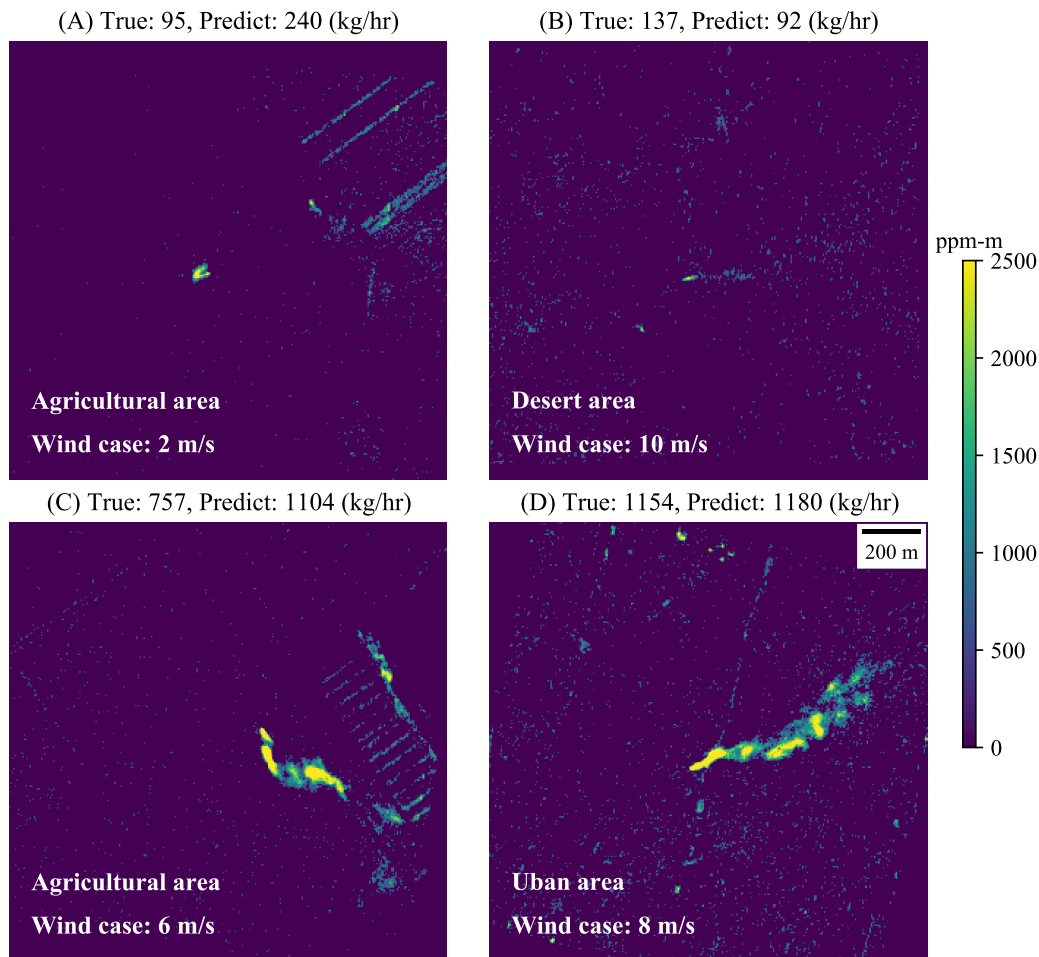


Figure 3.7: Examples of plume images with prediction errors higher than average for plumes over (a) agricultural area under the wind speed case of 2 m s^{-1} , (b) desert area, 10 m s^{-1} , (c) agricultural area, 6 m s^{-1} , and (d) urban area, 8 m s^{-1} .

have larger errors and tend to underestimate the true flux rates, likely because the model in this scenario was trained on only odd wind speeds omitting the 10 m s^{-1} case. At 10 m s^{-1} wind speeds plumes have more elongated structures, which were seen less often in the training data compared to typical structures under lower wind speed regimes (see Figure 3.2). We observed outliers for some plumes at very low fluxes, especially under 40 kg h^{-1} , across all wind speed regimes. Inspection of the scenes with low fluxes and high prediction errors reveals that these scenes have bright surface features (high correlated noise levels), which interfere with how the network perceives and predicts the actual fluxes from the images. For these scenes, it is hard for even human eyes to distinguish plumes from the noise. Thus, it is hard for the model to perform well on scenes with such an extreme case.

The range of errors by other methods such as mentioned in Varon et al. (2018) for plumes above 40 kg h^{-1} , when reanalysis wind data is used, is 15–65 %. The performance of MethaNet at approximately 21 % is comparable to this performance, but it completely removes the need for wind speed data during prediction. Overall, it is evident that our model can predict the emission rate of methane plumes accurately without the need for wind speed information. The implication of this result in scenario 1 also means that our model is capable of learning plumes under unseen wind speeds. That means that our discretization in the LES wind speed prescription (1, 2, 3, 4, 5, 6, 7, 8, 9, and 10 m s^{-1}) is fine enough. For instance, by learning the plume shapes and spatial distribution from plumes generated in the LES run with odd wind speeds such as 1 and 3 m s^{-1} , the model can learn the relationship of the plume 2-D structures and the associated emission rate from its point source under the even wind speed of 2 m s^{-1} . This reassures us that when we train the model on all the available 10 LES runs, our model will be able to learn and predict plumes under all wind speed regimes. This is a significant part in deploying the model for a real application during field campaigns. The performance of the model trained on all wind speeds is the subject of the next section.

Training and Predicting on All Winds

Here, the same model architecture as described in the previous subsection is trained based on scenario 2. In this scenario, the model learns from plumes under all wind speeds, and is validated and tested with a hold-out set of plumes, unseen from the beginning. This hold-out data represents a diverse set of plumes that could be detected in real world observations. The performance of the model prediction is shown in Figure 3.8. The model performance improves from that of scenario 1; it now has the mean absolute percentage error of 22 % across all plumes and about 17 % for prediction of plumes above 40 kg h^{-1} . The improvement of prediction at low flux rates under 40 kg h^{-1} is noticeable. This is likely due to the fact that the model can learn from a larger number of data points with more diverse variations, compared to scenario 1. To our knowledge, this level of performance at a mean absolute percentage error of 17 % is a state-of-the-art achievement for a model that does not rely on wind speed information.

From Figure 3.7, we see how correlated noise can interfere with the scenes, often leading to poor predictive ability. To show how improved measurements and retrievals can enhance this approach even further, we investigate the model perfor-

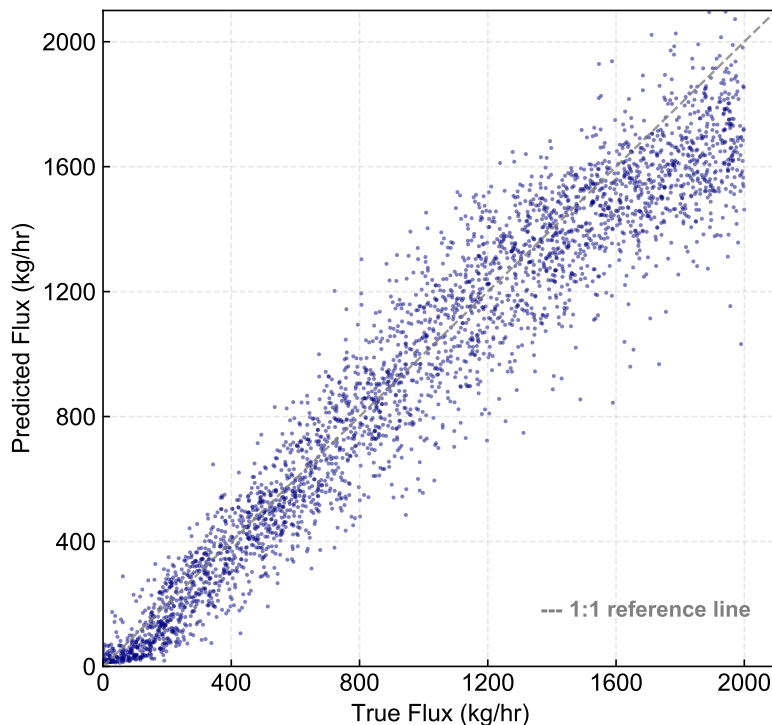


Figure 3.8: A plot showing a comparison between true fluxes and predicted fluxes by MethaNet trained from all LES runs with realistic background noise to predict unseen plumes in test set. A solid line shows a 1:1 reference line.

mance when the noise level becomes smaller and, more importantly, random without any spatial correlation structure. In this investigation, the background noise matrix as illustrated in Figure 3.3 is drawn from a Gaussian distribution with a zero mean and the standard deviation of 250 ppm-m, which is at the lower end of the range of a typical standard deviation in the realistic background scenarios (247-550 ppm-m). This result is shown in Figure 3.9 where we found that the performance of the model improves with a lower mean absolute percentage error of 17 % across all plumes and only 16 % for plumes above 40 kg h^{-1} . This hints to the importance of reducing the instrument precision error and correlated noise that comes from potential surface interferences to achieve lower bias in the methane point source quantification.

In addition to assessing the performance of this model in our test data set, we applied the model to an actual observation from a controlled release experiment. The analysis is given in the next section.

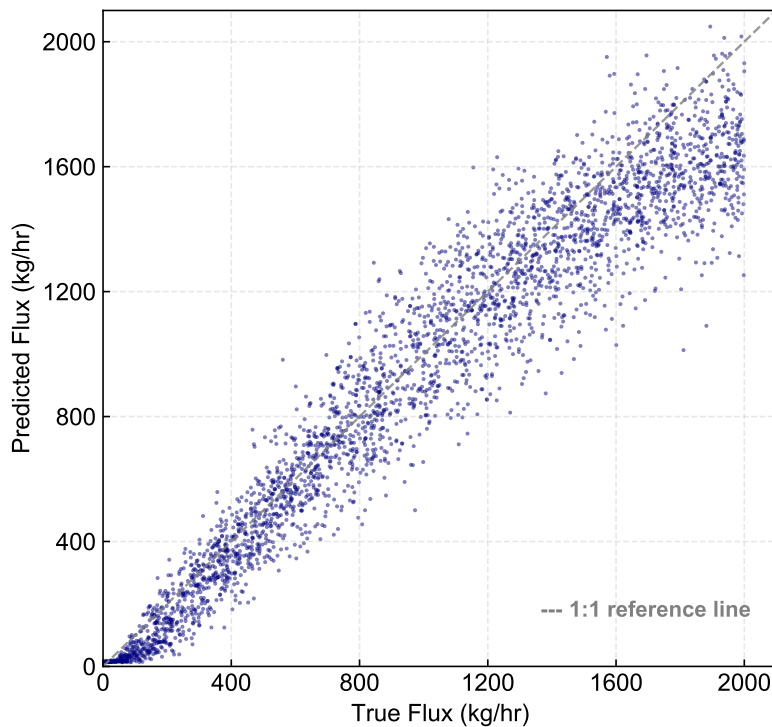


Figure 3.9: A plot similar to figure 3.8, but with the synthetic plume images that instead contain lower and uncorrelated noise, which is drawn from Gaussian distribution with a zero mean and a standard deviation of 250 ppm-m. A solid line shows a 1:1 reference line.

Results Predicting a Controlled Release Experiment

To further demonstrate the validity of this method, we applied our model to actual 2-D scenes of a methane column enhancement retrieved using a match filter retrieval algorithm from AVIRIS-NG radiance observations at 5 nm in the 2.1-2.3 microns band. This is obtained from a controlled-release experiment from a natural gas pipeline located at Victorville, CA (34.8, -117.3), during 15–17 June, 2017, with a flux release of $39 \pm 5 \text{ kg h}^{-1}$. The three snapshots of the same plume from this source is shown in Figure 3.10 with their corresponding surface sonic wind measurements during the overpasses. Based on each snapshot, we feed the 2-D image into our trained model and directly obtain a prediction of emission rate of the source in a one-shot manner. The predicted flux rates are 33, 26, and 32 kg h^{-1} for panel (A), (B), and (C). The mean and standard deviation is 31 and 3, respectively. This is consistent with the actual rate within one standard deviation. The mean prediction is approximately 20% deviated from the true value.

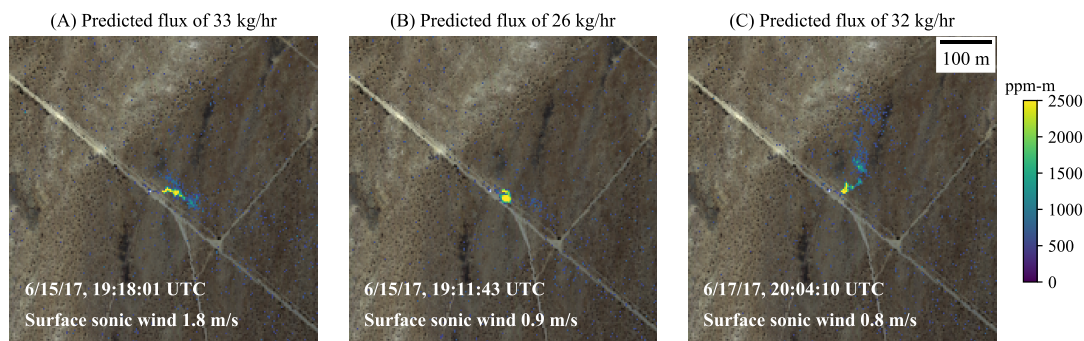


Figure 3.10: Controlled release experiment conducted at Victorville, CA. The scenes represent 3 overpasses with a controlled flux rate of 39 kg h^{-1} .

Detection

A step towards future automated quantification of localized sources at global scales is to filter out which images can be fed into the quantification routines. To further examine to what extent the MethaNet approach can distinguish small plumes that are interfering with high levels of noise, we modified the MethaNet for a related but potentially simpler task as a classification model to predict whether a scene contains a plume. This is achieved by changing the output layer of the MethaNet to be a softmax layer that outputs the probability for each of the two classes (contains plume or no plume). Scenes with no plumes are those scenes that have zero flux rates and only contain the background noise. We prepared the training, validation, and test data for the classification by fixing the plume flux rates to be zero half of the time in the plume augmentation step (as described in Section 3.4) before the noise scenes were added. Here, we train the model to just predict whether there is a plume or not. The classification accuracy for the test scenes with plumes of different emission rates is shown in Figure 3.11 (blue line). Above 100 kg h^{-1} , the model can predict the plume in the scene with an accuracy of more than 90 %, providing a basis that the model is able to see the structure of the plume. The classification accuracy drops to just above 50 % for plumes with emission rates around $50\text{-}60 \text{ kg h}^{-1}$, implying that at this level of emission, the plumes are no longer well distinguished from noise that exists in our retrieval background noise data. This range of emission rates is consistent with what we have found from the regression task in the previous subsections. The overall false positive rate is 12 %. Examples of false positives and false negative predictions from MethaNet in the classification task are shown in Figure 3.12.

From both Figure 3.7 and Figure 3.12, we see how correlated noise can interfere with

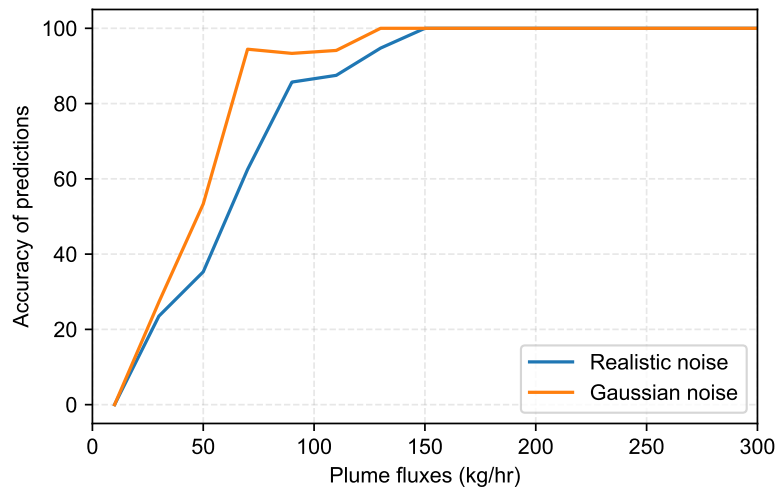


Figure 3.11: A plot showing the accuracy of MethaNet predictions for a classification task on plumes of different emission rates, calculated within each flux range.

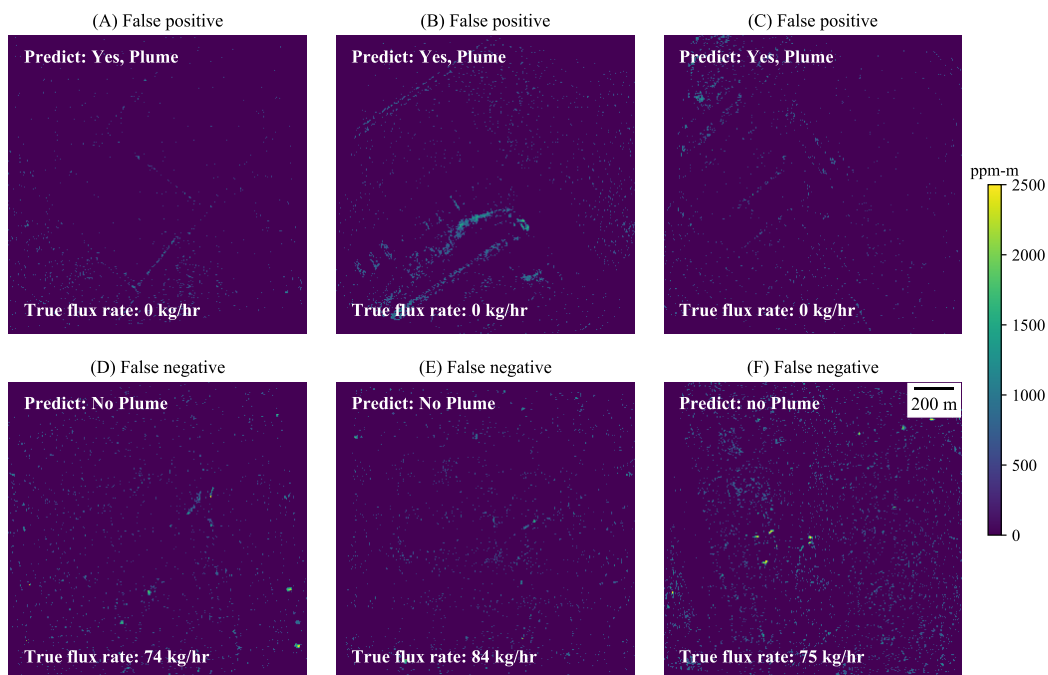


Figure 3.12: Examples of false positives and false negative predictions from MethaNet in the classification task.

the scenes, often leading to poor predictive ability. To emphasize how improved measurements and retrievals could lead to an increased model performance, we once again investigated the case when the background noise as illustrated in Figure 3.3 is drawn from a Gaussian distribution with a zero mean and the standard deviation of

250 ppm-m, which is at the lower end of the range of a typical standard deviation in the realistic background scenarios (247-550 ppm-m). This result is shown in Figure 3.11 (orange line), where we observe that the performance of the model improves noticeably for small plumes under 100 kg h^{-1} . We found that the accuracy of detection improved by around 10-20 % for flux rates between 40-75 kg h^{-1} . This finding underlines the point that our model can much better differentiate the plume from background noise when the noise is low and uncorrelated, i.e. random. Systematic structures that occur in the realistic noise impacts both the detection and quantification accuracy by appearing as misleading enhancements. This implies that to achieve even better performance in the future, it is vital to develop an instrument or a retrieval method that can reduce retrieval precision error and minimize retrieval biases from interferences with surface properties. Increasing spectral resolution would be an obvious way of better disentangling narrow atmospheric gas absorption features from broader solid/liquid reflectance features at the surface (Thorpe et al., 2016).

3.6 Concluding Remarks

In this study, we demonstrate a novel approach using deep learning to quantify methane gas emission based on high-resolution airborne imagery. Our method shows that an accurate estimate of methane emission rates can be directly obtained from CH_4 enhancement images without the need of simultaneous wind speed measurements. Our Convolutional Neural Network model can train the mapping between 2-D plume images and their corresponding source emission rates under various wind speed conditions. The training data are derived from realistic plume simulation using LES and realistic retrieval noise from AVIRIS-NG field observations. Our simulated CH_4 images represent a diverse set of realistic plumes of various emission rates between 0-2000 kg h^{-1} in different landscapes ranging from urban and desert to agriculture areas.

Our error analysis based on the model prediction of a hold-out set of unseen scenes shows an error of around 17 % on average for plumes with emission rates above 40 kg h^{-1} . For smaller plumes with emission rates under 40 kg h^{-1} , the model appears to be less accurate under a situation where the background noise is higher and spatially correlated. Under such scenarios, the small methane enhancements can interfere with the systematic background noise. If we also account for small plumes, the model can still predict with an error of approximately 22 %. This level of error is a significant improvement from other approaches, while it completely

removes the dependence on meteorological wind speed data which might not be reliable or available at high spatial resolution everywhere. An independent test on a controlled release experiment data over Victorville, CA, also validates a consistent prediction performance for MethaNet in real observations.

We further investigate the limit of small emission rates at which our model becomes unable to separate an actual plume from background noise. This is carried out by adjusting the output of our network for a simpler task, which is to make a binary prediction whether an image contains a CH₄ plume. Our analysis illustrates that below around 50-60 kg h⁻¹, the model struggles to classify the plume with an accuracy of less than 50%. Thus, the emission rate at around 50 kg h⁻¹ appears to be a threshold under which the MethaNet model will start to deteriorate. Inspection over these scenes of small plumes in the presence of surface retrieval noise reveals that it is very hard even for human eyes to distinguish whether a plume exists in the scene or the enhancement is due to background surface interferences. Correlated noise in the scenes with high prediction errors seems to come from surface interferences in the methane retrievals. A possible solution to make the model robust against this noise could be to incorporate other spectral channels such as RGB and incorporate this as part of the input to the network. The extra channels may potentially help the model differentiate areas of high correlated noise from the actual plume.

It should be noted that our LES modelling has the assumption that the topography is flat in our simulation domain. Different topographies of the areas from which CH₄ plumes are emitted such as on a hill or near surface obstacle (e.g. rocks or trees) could alter the spatial distribution of the plume. Another assumption in our LES is that our current emissions are at the ground level; the model does not yet incorporate direct emission that could be released at a height above the ground. Incorporating these additional features in the future could make our model even more applicable across a wider range of emission conditions, but it is currently outside the scope of this study. However, given that most typical areas of significant CH₄ emissions are in the flat areas such as oil fields, our approach has the potential for applications in common real-world scenarios. While we trained our CNN model on predicting plume emission rates from observations at a spatial resolution of 5 m from an airborne instrument such as AVIRIS-NG, our general modelling framework can be applicable to observations at different spatial resolution and instrument sensitivity. For a new instrument at different spatial resolution, the model should be retrained using new training data by applying the new instrument column averaging

kernel to the LES 3-D output to generate a new dataset of 2-D plume scenes that would be observed under such an instrument. The error characteristics of the new instrument measurements should also be incorporated to inform the choice of noise characteristics in the simulated plume images used in the training process. This modelling framework can also be applied to CO₂ with a change in the values of column averaging kernel used to simulate the total column enhancement that would be observed by a remote sensing instrument.

We have shown that this model can be applied to quantifying methane point-source emission in a quick and automated manner based directly on plume images alone. While the range of methane emissions prescribed in this study was between 0 and 2000 kg h⁻¹, we believe that the same approach can be applied to train plume images with other flux ranges as the plume enhancement in such case will be even more prominent compared to the background noise. In addition, our study found that low uncorrelated random noise from the retrieval process can greatly improve the predictions of smaller methane plumes. This hints to an important aspect, namely the need to develop instruments and/or methods to minimize and randomize retrieval noise. As many retrieval biases are related to surface interferences, a better instrument spectral resolution would help disentangling atmospheric absorption features from surface spectral features. With the level of performance of MethaNet, we believe it could be applied to recent large-scale flight campaigns to improve previous emission rate estimates. This also has immediate implications for future AVIRIS-NG flight campaigns. The methodology described in this study could also be applied to anticipated satellites such as The Earth Surface Mineral Dust Source Investigation (EMIT) that will provide methane measurements at finer spatial resolutions than currently available from space.

REMOTE SENSING OF METHANE PLUMES: INSTRUMENT TRADEOFF ANALYSIS FOR DETECTING AND QUANTIFYING LOCAL SOURCES AT GLOBAL SCALE

This paper is under review in:

Jongaramrungruang, S. et al. (2021). “Remote sensing of methane plumes: instrument tradeoff analysis for detecting and quantifying local sources at global scale”. In: *Atmospheric Measurement Techniques*, Under Review.

4.1 Abstract

Methane (CH₄) is the 2nd most important anthropogenic greenhouse gas with a significant impact on radiative forcing, tropospheric air quality, and stratospheric water vapor. Remote-sensing observations enable the detection and quantification of local methane emissions across large geographical areas, which is a critical step for understanding local flux distributions, and subsequently prioritizing mitigation strategies. Obtaining methane column concentration measurements with low noise and minimal surface interference has direct consequences for accurately determining the location and emission rates of methane sources. The quality of retrieved column enhancements depends on the choices of instrument and retrieval parameters. Here, we studied the changes in precision error and bias as a result of different spectral resolutions, instrument optical performance, and detector exposure times by using a realistic instrument noise model. In addition, we formally analyzed the impact of spectrally complex surface albedo features on retrievals using the Iterative Maximum a Posteriori–Differential Optical Absorption Spectroscopy (IMAP-DOAS) algorithm. We built an end-to-end modelling framework that can simulate observed radiances from reflected solar irradiance through a simulated CH₄ plume over several natural and man-made surfaces. Our analysis shows that complex surface features can alias into retrieved methane abundances, explaining the existence of retrieval biases in current airborne methane observations. The impact can be mitigated with higher spectral resolution and a larger polynomial degree to approximate surface albedo variations. Using a spectral resolution of 1.5 nm, an exposure time of 20 ms, and a polynomial degree of 25, a retrieval precision error below 0.007 mole m⁻² or 1.0 % of total atmospheric CH₄ column can be achieved for high albedo cases, while

minimizing the bias due to surface interference such that the noise is uncorrelated among various surfaces. At coarser spectral resolutions, it becomes increasingly harder to separate complex surface albedo features from atmospheric absorption features. Our modelling framework provides the basis for assessing trade-offs for future remote-sensing instruments and algorithmic designs. For instance, we find that improving the spectral resolution beyond 0.2 nm would actually decrease the retrieval precision as detector readout noise will play an increasing role. Our work contributes towards building an enhanced monitoring system that can measure CH₄ concentration fields to determine methane sources accurately and efficiently at scale.

4.2 Introduction

Anthropogenic greenhouse gas emissions have been rising continuously, affecting the global climate and the environment (Stocker et al., 2013). Among the most important anthropogenic emissions are carbon dioxide (CO₂) and methane (CH₄). Due to a much shorter lifetime of CH₄ (≈ 9 years) compared to CO₂ (≈ 500 years), CH₄ has gained attention as target for mitigation efforts to achieve short- and medium-term reductions of global warming (Montzka et al., 2011b; Prather et al., 2012; Shindell et al., 2012). In general, anthropogenic methane emissions are also much more uncertain than those of carbon dioxide, which can often be characterized to within approximately 10% just from budget assumptions (Gurney et al., 2019). For instance, just the question whether or not the leak rate in the natural gas extraction system is 1 or 2% is equivalent to a 100% uncertainty in methane emissions. At the same time, leak rate outliers (Frankenberg et al., 2016; Duren et al., 2019; Cusworth et al., 2021) are often local in nature and easily fixable, representing a win-win scenario if faulty equipment or practices can be readily detected, and then efficiently mitigated. As CH₄ reduction plays a significant role in climate mitigation efforts, one key step in emission reduction is determining where these emissions are coming from. This is underpinned in the 2018 NASA Decadal Survey, which calls out the identification and understanding of CH₄ emissions as one of the top priorities in the efforts to improve future climate projections, and help lead the way in emission reduction (Sciences and Medicine, 2018).

Remote-sensing instruments using absorption spectroscopy have emerged as one promising solution for measuring atmospheric CH₄ concentration over large geographical areas. Space-based CH₄ retrieval techniques from satellite observations such as the SCanning Imaging Absorption SpectroMeter for Atmospheric CHar-tographY (SCIAMACHY, Frankenberg et al., 2005a; Frankenberg et al., 2011) and

the Greenhouse gases Observing SATellite (GOSAT, Parker et al., 2011; Parker et al., 2015; Turner et al., 2015) were dedicated missions with CH₄ as a key target. They used CH₄ absorption features in the 1.6 and 2.3 μm bands to retrieve column CH₄ concentration across the globe. The TROPOspheric Monitoring Instrument (TROPOMI) with a spatial resolution of a few kilometers has also been shown to be capable of identifying regions of high emissions (Gouw et al., 2020; Hu et al., 2018). These satellites, which have been designed by the atmospheric community, have particular sets of goals and instrument specifications that are mostly targeted towards obtaining regional-scale methane distributions with high accuracy and precision. Most of these satellites were designed to measure gradients of methane concentration across hundreds to thousands of kilometers of scale, as this enables surface flux inversions at the global scale. Typically, all of these instruments have one feature in common—they have very high spectral resolution (0.05–0.25 nm) to distinguish individual methane absorption lines from spectrally smooth surface albedo variations. However, due to their coarse spatial resolutions, the measurements are not yet at a level where local sources can be identified, attributed to a specific source type (e.g. compressor station or well pad), and mitigated directly.

One potential solution to fill this scale gap is using an airborne instrument that has much higher spatial resolution such as the Methane Airborne MAPper (MAMAP, Gerilowski et al., 2011) or the next-generation Airborne Visible/Infrared Imaging Spectrometer (AVIRIS-NG, Thorpe et al., 2017). The latter is based on the insight that methane column enhancements at high spatial resolution (a few meters) can be so high that the retrieval of the absorbing feature can be done even with moderate spectral resolution (5–10 nm). If the methane column is expressed similar to the Dobson unit, i.e. as the thickness of a layer of pure gas which would be formed by the total column amount at standard conditions, the layer thickness at current background methane conditions would only be about 1.6 cm. Thus, a pure methane layer of only 1.6 mm would enhance the total column by 10%, which is certainly realistic for measurements of methane point sources at fine spatial resolution.

Bradley et al. (2011) and Thorpe et al. (2014) were among the first to show that moderate resolution instruments can detect methane plumes, even when the strong 2.3 μm methane band is convolved with the AVIRIS (10 nm) or AVIRIS-NG (5 nm) instrument line-shape functions. While individual lines are hard to resolve, the strong methane band in this range causes enough fine-structure in terms of bulk absorptions by a multitude of methane lines within the instrument resolution. Previous

studies by Frankenberg et al. (2016), Duren et al. (2019) and Cusworth et al. (2021) have utilized AVIRIS-NG to conduct field campaigns in California, the Four-Corners region, and the Permian basin where they could create a map of methane enhancements in the area and detected several hundreds of individual methane sources, which followed a heavy-tail flux distribution. The concept of this airborne spectrometer provides a signal of opportunity for local source detection and quantification. However, the instrument was not originally designed for methane detection, and it does not meet the same precision and accuracy requirements as those satellites from the atmospheric community for methane retrieval at a global scale, which require accuracy better than 1%, equivalent to enhancements of about 19 ppb in XCH_4 (or $4 \cdot 10^{17}$ molec cm^{-2} , 0.007 mole m^{-2} or 152 ppm – m). One significant drawback of coarse spectral resolution is the occurrence of retrieval artefacts that often correlate with specific surface features (see Figure 4.1). This can confound the detection and quantification of methane point sources in the analysis and obviate the robust detection of subtle gradients at larger spatial scales (Jongaramrungruang et al., 2021 (in review)). Even though most strong plumes can be observed, the uncertainties in the overall detection and quantification at the regional level can present persistent problems and often involve human judgement to isolate plumes from artefacts. In fact, during each of the California survey, the Four-corners study, and the Permian survey (Duren et al., 2019, Frankenberg et al., 2016, Cusworth et al., 2021), human analysts were involved in a manual process to look through each flight line to classify true emission sources from false positives. Similarly, in previous space-based studies to locate and approximate a large emission such as a blowout event, prior information about the location of the source is usually already known, making it much easier to find a true methane source from space-based measurements over the area after the fact. There are ongoing efforts to develop automated plume detection for existing instruments. Future real-time monitoring systems would greatly benefit from next generation instruments that would reduce retrieval artifacts and provide retrievals with improved accuracy, such that remote-sensing measurements can be analyzed to locate and quantify plumes automatically, at scale. Hence the origination of this study.

If we had the opportunity to design a new instrument that is optimized for methane retrievals at fine spatial resolution (sub 50-m), what would the specifications of this instrument look like? Thorpe et al. (2016) proposed a 1 nm instrument to mitigate the drawbacks of AVIRIS-NG. To fully evaluate optimal performance metrics, we have to consider the tradeoff between spectral and spatial resolutions and concomi-

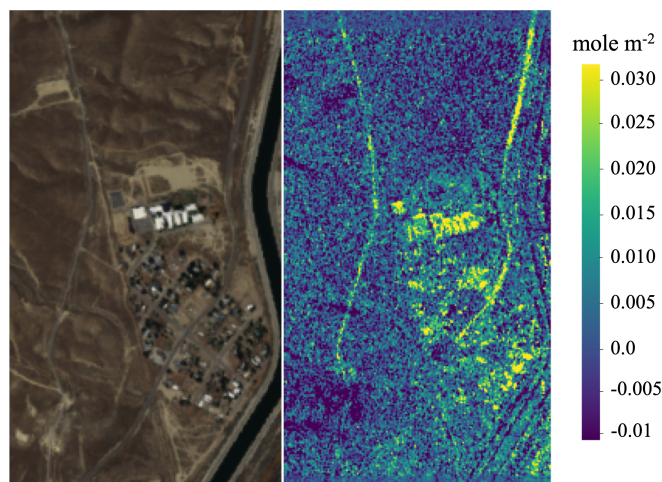


Figure 4.1: Example of systematic outliers from a retrieved AVIRIS-NG scene (right) compared with an RGB image (left).

tant changes in detector noise characteristics. On the one hand, the instrument needs to meet the requirements of the atmospheric community so that it can unambiguously differentiate methane from other confounding factors. On the other hand, the instrument should have adequate integration time to achieve high spatial resolution with sufficient signal-to-noise levels. Here, we investigate this tradeoff and evaluate risks and benefits for methane retrievals at fine resolutions with the purpose of successfully detecting and quantifying local sources in mind. We built an end-to-end modeling framework that can generate reflected solar radiance through a methane plume of known concentration over realistic surfaces, and perform the retrieval from the corresponding observed radiance under a given instrument to output the predicted methane concentration in each column. Our model calculates the noise-equivalent spectral radiance (NESR) as a function of incoming radiance and instrument parameters such as integration time, detector size, quantum efficiency, readout noise, and spectral resolution, rather than prescribing the signal-to-noise ratio (SNR) as an independent variable. By varying the instrument and retrieval parameters, we can derive the associated precision error and bias from the retrieval. We also compare the tradeoff between the two most frequently used fitting windows in the 1.6 and 2.3 μm ranges.

Section 4.3 outlines the background on radiative transfer, followed by data and methodology on the forward model with realistic surface reflectances, instrument

operators, and retrieval setups. Results and discussion are provided in Section 4.4. The final section contains concluding remarks and future steps.

4.3 Data and Methodology

For the sake of simplicity, we ignore the impact of atmospheric scattering, as Rayleigh scattering is negligible in the near-infrared and the impact of aerosols is rather small compared to methane enhancements in the near-field of local sources. While aerosols can cause small systematic biases in the retrieved methane amount, their impact on measuring anomalies caused by methane plumes should be rather small. In addition, the precision error is not strongly affected by neglecting atmospheric scattering, and experience with previous moderate resolution methane mapping has shown that surface interferences are more crucial. In the absence of atmospheric scattering and assuming a Lambertian surface, the reflected radiance as measured by an instrument at the top of the atmosphere in the Nadir direction can be modelled as

$$L_{\lambda} = I_{0,\lambda} \cdot r_{\lambda} \cdot T_{\lambda\uparrow} \cdot T_{\lambda\downarrow} \cdot \frac{\cos(SZA)}{\pi} \quad (4.1)$$

where I_0 stands for the incoming solar irradiance spectrum, $T_{\lambda\downarrow}$ the atmospheric transmission along the photon light-path downwards to the surface, r_{λ} the surface albedo, $T_{\lambda\uparrow}$ the transmission along the light-path on the way up from the surface to the instrument, and SZA the solar zenith angle. Figure 4.2 illustrates a schematic for Equation 4.1. The subscript λ denotes the wavelength dependence of these variables. The multiplication in Equation 4.1 is element-wise for each wavelength in the spectral range of interest.

Incoming Solar Irradiance

We constructed $I_{0,\lambda}$ by multiplying a continuum level spectrum with a high-resolution solar transmission spectrum that includes absorption features in the sun's photosphere, so-called Fraunhofer lines. These absorption features are caused by trace elements in the solar photosphere. The continuum spectrum is obtained from Mef-tah, M. et al. (2018) with 0.2 nm resolution. We fitted a 3rd-order polynomial to this measured spectra in a 1.4 - 2.5 μm range to obtain a smooth continuum spectrum. A disk integrated solar transmission spectrum is obtained from a tabulated line-list compiled by Toon (2015). We interpolated the baseline and transmission spectra to a common 0.01 nm resolution grid, and multiplied them to obtain a high-resolution solar irradiance $I_{0,\lambda}$.

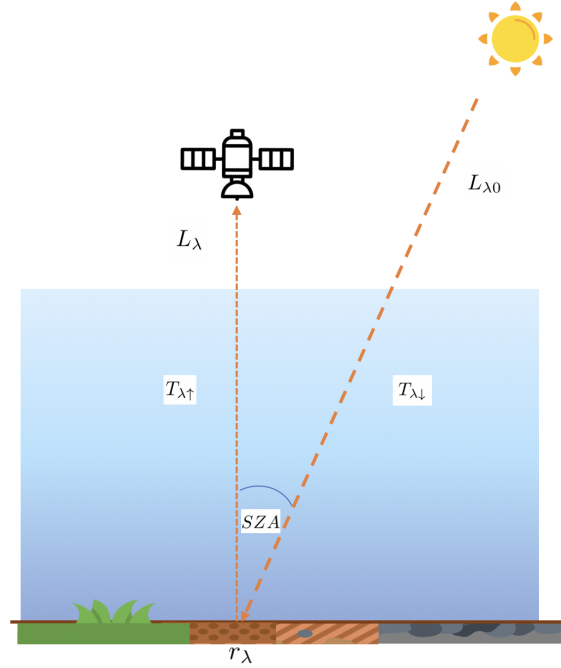


Figure 4.2: A schematic for reflected sunlight from the sun through the atmosphere to a spectrometer in space.

Atmospheric Transmission

The atmospheric transmission can be modelled using the Lambert-Beer Law by dividing the atmosphere into vertical layers, each with constant pressure, temperature and gas number density. We calculate absorption cross-sections for each layer using the HITRAN spectral database (Gordon et al., 2017) and a Voigt lineshape. The transmission then reads

$$T_{\lambda} = \exp \left(- \left(\sum_i \sum_k n_{i,k} \sigma_{i,k(\lambda)} \times AMF_k \right) \right), \quad (4.2)$$

where i denotes the i^{th} gas species, k the k^{th} layer, n the vertical column density (molecules cm^{-2}), and σ the gas absorption cross-section (which is a function of pressure (P) and temperature (T)). The air mass factor (AMF) per layer denotes the ratio of the integrated number concentration along the actual photon light-path and the geometric vertical integration. In the absence of scattering, it is $1/\cos(SZA)$ for the incoming light at SZA , and equal to 1 for the outgoing light as seen in Nadir.

The transmission of the atmosphere is calculated from the background gas concentrations from the top of the atmosphere (TOA) to the surface. In addition, we consider the enhancements due to local gas emissions which we primarily consid-

ered to reside between the atmospheric boundary layer (BL) and the surface. The instrument is assumed to be located at the TOA.

For the background transmission, we divided the atmosphere into 72 layers, and used an atmospheric profile for p and T from the Four-Corners area (lat = 36.8° , lon = -108°). We considered H_2O , CO_2 , and CH_4 in the background. Concentration of H_2O is obtained from the MERRA reanalysis (Rienecker et al., 2011) vertical profile. For simplicity, background CO_2 and CH_4 are set to volume mixing ratios of 400 ppm and 2000 ppb, respectively. For the gas enhancement within the BL, 300 vertical layers are used to model a simulated 3-D methane plume enhancement from Large Eddy Simulation (LES) output. The LES enables a realistic simulation of how methane concentrations from a point source evolve in space and time, as it generates the time-resolved three-dimensional CH_4 distribution in the boundary layer. The full description of the LES model setup for CH_4 plume emanating from a point source can be found in Matheou and Bowman (2016), with the model parameterization and initialization detailed in Jongaramrungruang et al. (2019). We computed the gas absorption cross sections in each layer using an open-source Julia radiative transfer tool that calculates the cross-section efficiently using the HITRAN database and GPU capability (Gordon et al., 2017). A Voigt absorption line shape is used in our study. We note that we used 300 vertical layers in the BL in the full forward model to simulate the observed outgoing spectra, but will use a much smaller number of layers in the retrieval step (more details later).

Surface Reflectance

To analyze the impact of surface spectral features, we compiled a database of different surface albedos from the ECOSTRESS spectral library (Meerdink et al., 2019) to investigate the impact on our traditional retrieval technique that we use from space, in which the surface is typically characterized by a low-order polynomial in wavelength. In fact, many spectroscopic measurement techniques rely on the fact that atmospheric features exhibit sharp absorption features while surfaces are spectrally smooth (Platt and Stutz, 2008). From a physical perspective, this is related to more rapid quenching of an excited state in solids or liquids as well as the suppression of rotational energy levels. At the same time, this separation of high-frequency atmospheric features from low-frequency surface features is at the core of our study, as instruments such as AVIRIS(-NG) have spectral resolutions that can blur the separation between frequencies, allowing surface features to alias

into methane retrievals.

The compiled database contains more than 2000 surfaces over 5 main categories of rock, soil, mineral, photosynthetic and non-photosynthetic vegetation, and man-made construction materials. Examples of these surface albedos near the 2.3 μm CH_4 absorption range are shown in Figure 4.3. The typical spectral resolution of the database is 2 nm, and we resampled all spectra to a common grid, subsequently used with spline interpolation in our high-resolution forward model at 0.01 nm.

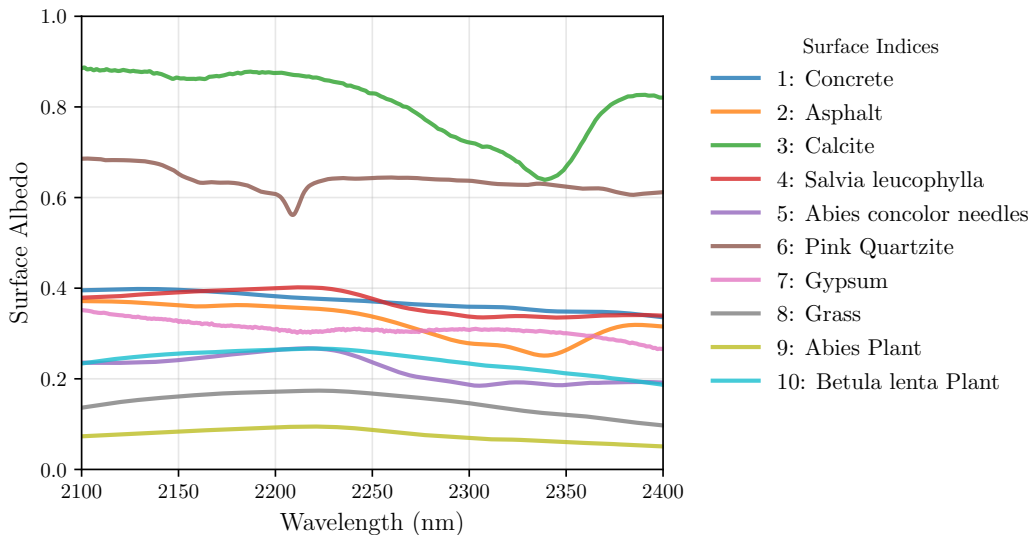


Figure 4.3: Albedo spectral variations near 2.3 μm from distinct surface reflectances in our database.

Based on this database, we can create an arbitrarily diverse set of surfaces underlying the simulated 3-D methane field. For example, a checkerboard-styled tile consisting of 3×10 surfaces can be constructed before we overlay the 3-D plume. A retrieval can then be applied for each pixel across the source to visualize the impact on precision error and bias caused by different surfaces. We also used LANDSAT data (Wulder et al., 2019) to represent a natural distribution of surfaces in the Durango area, Colorado. Although it is a 30-m resolution, we can upsample the surface grids to 5-m each. At each pixel, we matched the measured surface albedo from LANDSAT observations at 0.48, 0.56, 0.65, 0.87, 1.61, and 2.20 μm to the closest possible surface in our database, and queried its full albedo spectra for our simulations.

Instrument Operators

Convolution and Observed Spectra

The actual observed spectrum that is recorded by the instrument is the convolution of the high-resolution incident light L_λ with the instrument line shape, denoted here as instrument kernel. This convolution is performed in the intensity space given by

$$\langle L(\lambda) \rangle = \int_{-\infty}^{\infty} L(\lambda') \phi(\lambda - \lambda') d\lambda' \quad (4.3)$$

where $L(\lambda)$ is the incident spectra on the device and $\langle \rangle$ denotes the convolution with the instrument kernel ϕ . The convolved spectrum can then be interpolated and resampled to the output wavelength grids (λ_{out}) of the instrument, in an observing spectral range of interest. This output spectra is used as the measurement vector in the retrieval process (more details in the retrieval setup section).

The instrument kernel ϕ is modelled using a Gaussian distribution with zero mean and a given Full-Width-Half-Maximum (FWHM). In our experiment, we treated the FWHM as an independent variable that varies between 0.04 and 10.0 nm. The FWHM is a key property of an instrument that determines what spectral variations can be resolved. For instance, if the spectral resolution is coarser than the rotational fine-structure of a vibrational-rotational absorption band, the P and R branches of this band will appear as just two separate broad-band absorption features. The spectral sampling interval (SSI) varied accordingly with FWHM. Here, we use two cases of SSI equal to FWHM/2.5 (near Nyquist sampling in atmospheric sounders) and FWHM/1.0 (critical sampling as in AVIRIS-type imaging spectrometers).

Noise-equivalent Spectral Radiance

Towards designing the optimal instrument, we have to evaluate the trade space of spectral resolution, spatial resolution, and detector characteristics. Previous studies evaluated the trade space between signal-to-noise ratio (SNR) and spectral resolution, treating the SNR as an independent variable when varying the spectral resolution (Thorpe et al., 2016; Cusworth et al., 2019; Ayasse et al., 2019). However, the SNR deteriorates at higher spectral resolution, as fewer photons are being counted by each detector pixel. To evaluate this properly, we start working from an instrument model directly where the noise is a function of incoming radiance, and parameters such as integration time, F number, detector pixel, and the spectral resolution, as described in Strandgren et al. (2020). In this approach, the SNR will be a dependent variable based on our instrument specifications and the actual observed radiance.

The electronic signal measured by each detector pixel can be expressed as (Strandgren et al., 2020):

$$S = \langle L_\lambda \rangle \frac{\pi A_{det}}{4f_{num}^2} \cdot \eta \cdot Q_e \cdot \Delta\lambda \cdot t_{int}, \quad (4.4)$$

where $\langle L_\lambda \rangle$ is our simulated radiance, A_{det} the detector pixel area, f_{num} the instrument's f number, η the optical efficiency of the spectrometer, Q_e the quantum efficiency of the detector, $\Delta\lambda$ the SSI, and t_{int} the integration time.

For the NESR, we consider two dominant noise terms, namely shot noise (proportional to \sqrt{S}) and effective readout noise σ_{ro} :

$$NESR = \sigma_{L_\lambda} = \sqrt{S + \sigma_{ro}^2}. \quad (4.5)$$

For the analyses in this study, we varied FWHM from 0.04 nm to 10.0 nm, integration time from 5 ms to 105 ms, with other default parameter setups as described in Table 4.1, unless stated specifically otherwise.

Table 4.1: A table for default parameter settings in our simulations.

Parameter	Value
Integration time	20 ms
Detector size	30.0 μm
F-number	2.4
Quantum efficiency	0.95
Optical bench efficiency	0.5
Readout noise	100.0

Retrieval Setup

Forward Model

The retrieval forward model is similar to that described earlier in the atmospheric transmission section. The main difference is that we now treat the methane concentration in the boundary layer as elements of the state vector that we want to retrieve, as the methane profile is unknown during the observation. A much smaller number of layers to represent methane enhancements within the boundary layers is used. This is an important consideration when dealing with moderate spectral resolution since the information content is not high enough to discriminate between different layers. Polynomial terms are also used to represent the change in surface reflectance

with wavelength. The forward model can be written mathematically as

$$\vec{y}_\lambda = F(\vec{x}) = \langle L_{\lambda_0} \cdot T_{\lambda\uparrow} \cdot T_{\lambda\downarrow} \rangle \underbrace{\sum_{d=1}^D a_d P^d(\lambda)}_{\approx r_\lambda} \quad (4.6)$$

where \vec{y} is the measurement vector, $P^d(\lambda)$ a Legendre polynomial term at degree d , a_d a coefficient for each $P^d(\lambda)$, and D the number of polynomial degree used in the retrieval. To evaluate the polynomial degree within the fitting range, we converted the wavelength range within the fitting window to span -1 through 1. Here, the state vector \vec{x} consists of the vertical column density (molecules cm^{-2}) of the respective gases in different layers and polynomial coefficients accounting for low-frequency surface features.

In our experiment, we set the number of water vapour and methane concentration layers to be 2 and 10, respectively. We vary the number of polynomial degree, D , to investigate its ability to disentangle the surface spectral variations from the atmospheric features, while simultaneously considering different instrument spectral resolutions. Spectrally smooth surface albedos might only require a few polynomial coefficients while more complex surface features within the 260 nm fitting window can require more than 25 coefficients, as will be shown later.

Optimal Estimation

To solve for the optimal state vector from this nonlinear system, we used the Iterative Maximum a Posteriori–Differential Optical Absorption Spectroscopy (IMAP-DOAS) approach (Frankenberg et al., 2005a). Based on maximizing the a posteriori probability density function as introduced to the atmospheric community by Rodgers (2000), the iterative solution can be written as

$$\vec{x}_{i+1} = \vec{x}_a + (\mathbf{K}_i^T \mathbf{S}_\epsilon^{-1} \mathbf{K}_i + \mathbf{S}_a^{-1})^{-1} \mathbf{K}_i^T \mathbf{S}_\epsilon^{-1} \cdot [\vec{y} - F(\vec{x}_i) + \mathbf{K}_i(\vec{x}_i - \vec{x}_a)] \quad (4.7)$$

where \vec{x}_i is the state vector at the i^{th} iteration, \vec{x}_a a priori state vector, \mathbf{S}_ϵ the measurement error covariance matrix, \mathbf{S}_a a priori covariance matrix, and \mathbf{K}_i the Jacobian of the forward model evaluated at \vec{x}_i . $F(\vec{x}_i)$ stands for a forward model at each \vec{x}_i . When consecutive changes in the reduced χ^2 of the fit drop below a tolerance level of 10^{-3} , we stop iterations. The Jacobian matrix \mathbf{K}_i is computed analytically in each i^{th} iteration using automatic differentiation techniques. The a priori covariance matrix \mathbf{S}_a helps constrain the fit based on the possible range of

concentration (thus \vec{S}_a is a square matrix with a size equal to the length of \vec{x}_i). Here, we use loose prior constraints, thus having no significant impact on the retrieved total columns or posterior errors. The measurement error covariance matrix \mathbf{S}_ϵ is a matrix, in which the diagonal elements are the estimated variances of instrument noise at the observed wavelength grid λ_{out} (thus \mathbf{S}_ϵ is a square matrix with a size equal to the length of λ_{out}). These variances are computed from the instrument noise model outlined earlier.

Error Estimations

The posteriori error estimate $\hat{\mathbf{S}} = (\mathbf{K}^T \mathbf{S}_\epsilon \mathbf{K} + \mathbf{S}_a)^{-1}$ provides the full error covariance matrix of the retrieved state vector \hat{x} . The quantity of interest in our application for CH₄ detection and quantification is the total column concentration of CH₄. To obtain this quantity from our retrieval, we can find the summation of the state vector elements over indices corresponding to CH₄. We can thus define a summation operator \vec{h} of the same size as the state vector, filled with ones where CH₄ state vector elements are located and zeros elsewhere. The summation of the total column is readily derived as $\vec{h}^T \hat{x}$ and the variance of the total column is computed as $\vec{h}^T \hat{\mathbf{S}} \vec{h}$ (Rodgers, 2000). The bias error is obtained as the difference between the best estimated value in the absence of instrument noise and the true CH₄ vertical column enhancement.

LES CH₄ Plumes

The LES is used to generate the time-resolved three-dimensional CH₄ distribution in the boundary layer. This provides a realistic distribution of how methane concentrations from a point source on the ground evolve across the area. The flow in the boundary layer is driven by a constant geostrophic wind in the x direction, influencing the shape of the plume. We conducted LES experiments with a geostrophic wind speed of 4 m s⁻¹ with a range of emission rates from 50 to 5000 kg h⁻¹

To simulate the reflected sunlight over the area of a CH₄ emission source, we use the output from LES that has a realistic 3-D concentration field of CH₄ at a prescribed emission rate and overlay this on top of surface tiles of different albedos. Within each tile, the albedo is chosen from a distinct surface in our database. Figure 4.4 illustrates this conceptual setup.

At each pixel, the high-resolution outgoing reflected radiance can be calculated and subsequently be convolved with the instrument kernel. This yields the simulated

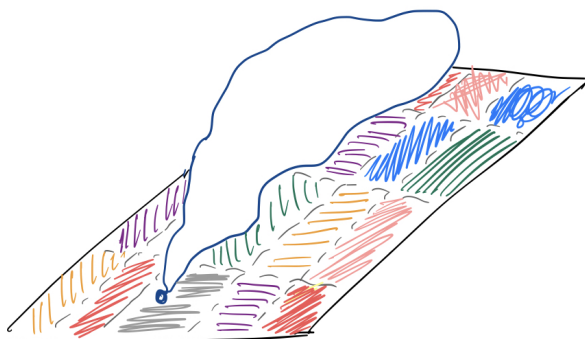


Figure 4.4: A schematic showing the setup for a methane plume over different surface tiles, each of which contains one surface albedo from our database.

observed radiance at each pixel that we implemented as a measurement vector. Accordingly, the pixel radiances are then converted to signal strength in electrons and respective noise levels using our instrument model. The IMAP-DOAS algorithm is applied to retrieve the column CH_4 and provide error estimates. We can vary the instrument parameters as well as the number of polynomial degrees in the retrieval to explore their relationship with the associated errors.

4.4 Results and Discussion

Simulated High-Resolution and Observed Radiance

As a first step towards understanding the effect of the instrument spectral resolution, we simulated high-resolution spectrum $\langle L_\lambda \rangle$ in the $1.6 \mu\text{m}$ and $2.3 \mu\text{m}$ bands and their corresponding Jacobians for instruments with FWHM of 0.2, 1.5, 5.0, and 10.0 nm. This simulation is based on the CH_4 concentration profile near an origin of the methane plume with an emission rate of 200 kg h^{-1} , over a construction concrete (albedo index 1 in Figure 4.3), with simulations shown in Figure 4.5. As the instrument FWHM increases, individual absorption lines are increasingly blurred, and the less high-resolution absorption features are recorded. The Jacobian represents the change in radiance with respect to the changes in gas concentration. Here we show the Jacobian for CH_4 and H_2O close to the ground. For the $1.6 \mu\text{m}$ band, the total radiance is in the range of $20\text{-}30 \text{ mW m}^{-2} \text{ nm}^{-1} \text{ sr}^{-1}$, and we observed the strongest absorption feature between $1.66\text{-}1.67 \mu\text{m}$, covering the Q-branch in the $2\nu^3$ band. On the other hand, for the $2.3 \mu\text{m}$ band, the radiance varies from around 10 to $3 \text{ mW m}^{-2} \text{ nm}^{-1} \text{ sr}^{-1}$ across the band. The CH_4 absorption features are much

stronger and prominent over a wider range from 2.2 to 2.4 μm . To compare the two fitting windows in terms of their effectiveness in CH_4 measurements, we explore errors associated with the CH_4 retrieval using each of these bands in the next section.

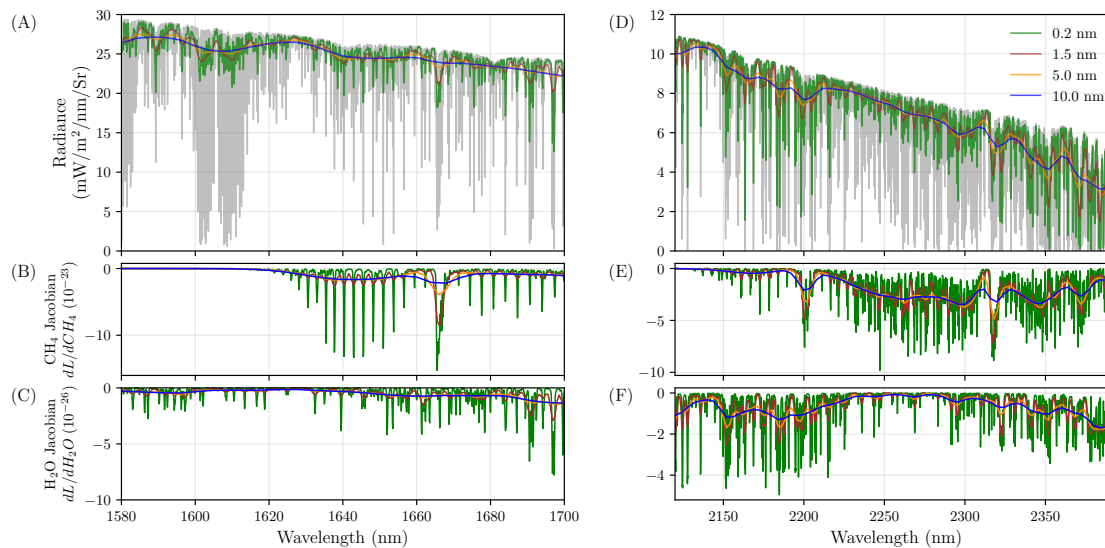


Figure 4.5: Simulated reflected solar radiance through a plume of 200 kg h^{-1} , over a concrete surface as observed by instruments of different FWHM in the two fitting windows of $1.6 \mu\text{m}$ (left) and $2.3 \mu\text{m}$ (right). The grey background is the originally calculated spectra at 0.01 nm .

Comparisons of Two CH_4 Fitting Windows

We investigate the comparison between two different CH_4 fitting windows near 1.6 and $2.3 \mu\text{m}$. At $1.6 \mu\text{m}$, the incoming solar irradiance is higher, which could enhance the signal-to-noise ratio. However, at $2.3 \mu\text{m}$, the CH_4 absorption features are more numerous and prominent over a broader wavelength range, which should increase sensitivity for the CH_4 retrieval. Thus, there is a potential trade-off between the advantages and disadvantages of both retrieval windows. It is not immediately obvious which fitting window would result in a lower precision error. This could also depend on the spectral resolution, as spectral fine-structure changes with increasing FWHM differently in both windows. Understanding this trade-off will help guide the development of future instruments.

The resolve that which band is better suited for minimizing CH_4 retrieval errors also depends on typical surface albedos at 1.6 and $2.3 \mu\text{m}$. We visualized the relative values of surface albedo at 1.6 and $2.3 \mu\text{m}$ across all surfaces in our database colored by their main surface categories in Figure 4.6. Most surfaces lie in the region where

their albedos at 1.6 and 2.3 μm are relatively equal (along the 1:1 line). Only a few surfaces have a much higher albedo at 2.3 μm compared to that at 1.6 μm , while there is a cluster of low-albedo surfaces for which the 1.6 μm albedo is about twice as high as at 2.3 μm . To compare the two fitting windows, we take two extreme surface examples: one with albedo of 0.87 at 1.6 μm and 0.14 at 2.3 μm , and another one with albedo of 0.21 at 1.6 μm and 0.79 at 2.3 μm . We also consider a representative surface with an equal albedo of 0.51 at both 1.6 and 2.3 μm .

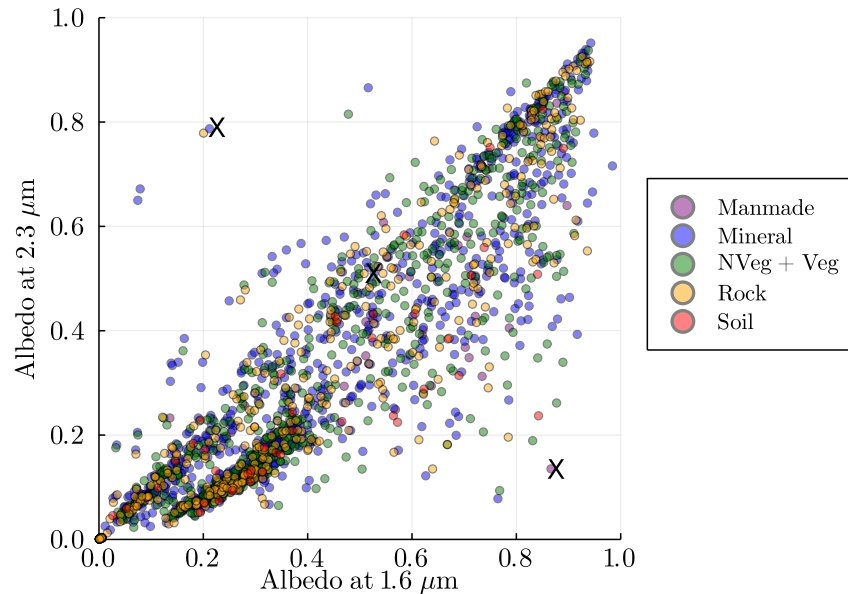


Figure 4.6: Scatter plot showing the relative values of reflectance at 1.6 vs 2.3 μm for different surface types. Each point is a distinct surface, and the color shows the type to which it belongs. Cross marks represent three example surfaces that we used in the comparison analyses.

In Figure 4.7, we compared the precision errors based on the two fitting windows over the three surfaces using a polynomial degree of 25, using fitting windows as displayed in Figure 4.5. In this simulation, only FWHM is varied and an oversampling of 2.5 is used (i.e. $\text{FWHM} = 2.5 \cdot \text{SSI}$). Other instrument parameters are set according to Table 4.1. The corresponding NESR of each detector pixel is then computed using the instrument noise model, enabling us to compute the changing noise levels with instrument resolution. We note that the number of detector pixels used varies considerably in this simulation, as they correspond to the window length (275 nm in the 2.3 μm band) divided by SSI. Thus, FWHM smaller than 0.65 in the 2.3 μm band would require more than 1000 detector pixels, which can be hard to achieve from a detector point-of-view, especially at fast readout rates, as required for high

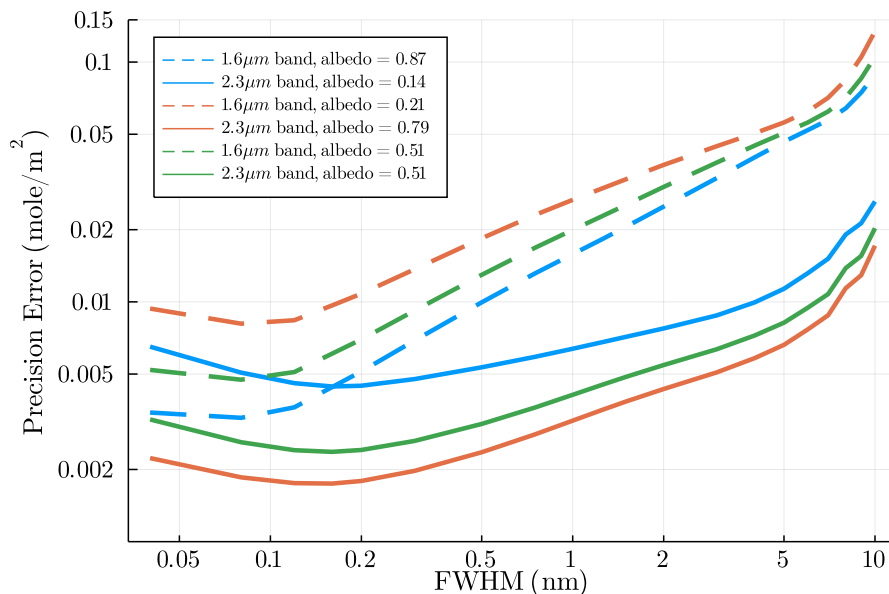


Figure 4.7: A plot showing precision errors from CH_4 retrieval in the $1.6 \mu\text{m}$ band (dotted) and the $2.3 \mu\text{m}$ band (solid) over three distinct surfaces (colored), using instruments with different FWHM.

spatial resolution. This can preclude very fine spectral resolution if a large spectral bandwidth is required, which can be beneficial, especially if it allows additional species to be measured (such as CO_2). In addition, at coarser spectral resolution, the full well capacity of the detector might be reached, which puts an upper limit of maximum SNR values per detector pixels (maximum SNR of 1000 for a full well capacity of 10^6 electrons).

Here, we observe that the precision error is actually not monotonically improving with finer spectral resolution, as the SNR deteriorates in these cases. For the $2.3 \mu\text{m}$ band, the optimum is actually around 0.2 nm , which may appear surprising. For darker surfaces, the precision using a 1 nm resolution can be equal to an instrument with 0.05 nm resolution. Interestingly, the precision errors using the $1.6 \mu\text{m}$ band deteriorate much more with increasing FWHM than using the $2.3 \mu\text{m}$ band. The reason for this is related to the methane band structure in both windows, as can be seen in the Jacobians (see Figure 4.5). In the $1.6 \mu\text{m}$ band, most of the fine-structure in the P and R branches are lost once the FWHM is coarser than the separation of the rotational fine-structure, leaving only the Q-branch spectrally distinct, even at lower spectral resolution. This could also be seen in SCIAMACHY, for which the FWHM in the $1.6 \mu\text{m}$ band was relatively low, namely about 1.3 nm (Frankenberg et al., 2005c). With the loss of spectral fine-structure, the precision deteriorates more

rapidly as low frequency variations in the Jacobians can be confused with surface albedo features, thus not directly constraining methane abundances. The situation in the 2.3 μm band is different as the absorption structures are very different, covering many more methane features that are irregularly spaced. Thus, some unique bulk methane absorption features persist even at spectral resolutions as coarse as 10 nm. In fact, this is the reason methane could be observed with imaging spectrometer at similar resolutions (Thorpe et al., 2014), enabling high spatial-resolution mapping from airborne instruments.

Overall, our retrievals in the 2.3 μm band consistently yield lower precision errors compared to that from the 1.6 μm band. This difference is most highlighted for a surface with a much higher albedo at 2.3 μm compared to 1.6 μm . This is because decrease in solar irradiance at 2.3 μm is now compensated for by increased albedos, resulting in observed radiances to be relatively close to that at 1.6 μm , allowing for the effect of absorption depth and structure to be the sole driving force for a better performance. This effect is still seen for most typical surfaces of equal albedos at both 1.6 and 2.3 μm , where the precision error from the 2.3 μm band is consistently lower than that from the 1.6 μm regions for instruments with any FWHM. The only scenario where the retrieval at 1.6 μm could perform better is under an extreme example where a surface has a much stronger albedo at 1.6 μm compared to at 2.3 μm , and when FWHM is lower than 0.2 nm. These results indicate that the stronger and broader absorption of CH_4 in the 2.3 μm fitting window plays a more dominant role in the retrieval performance compared to the stronger solar irradiance (and sometime higher albedo) in the 1.6 μm case. Since the latter condition for a better performance in the 1.6 μm band is much more unlikely, we focus our following analysis on the 2.3 μm fitting window.

Spectral Fit and Error Analysis with Various Instruments

Here, we evaluate the instrument performance of hypothetical yet realistic spectrometers covering the 2.3 μm range. If we restrict ourselves to the number of spectral pixels in a fast detector, as used for AVIRIS-NG (480 spectral pixels), we can achieve a FWHM of around 1.5 nm, minimizing the precision error under the hard constraint of a limited detector size. It would also still allow for joint retrievals of CO_2 at 2 μm , as envisioned in Strandgren et al. (2020). This resolution allows us to still resolve significantly more spectral fine-structure than current measurements at 5 or 10 nm resolution, which often exhibit retrieval interferences with surface features, as seen in Figure 4.1. Our primary focus here is to quantify the impact of

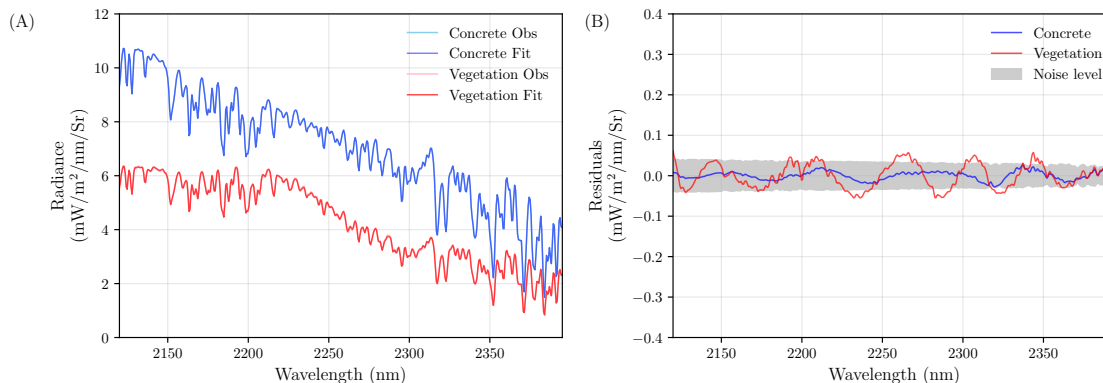


Figure 4.8: (A) The observed spectra through the exact same CH₄ source over two different surfaces, construction concrete and vegetation, as observed by an instrument with FWHM of 1.5 nm, and their best spectral fit. (B) Their associated spectral residuals and an expected 1- σ noise level for the instrument measurement.

spectral resolution on the ability to unequivocally separate surface spectral features from those in the atmosphere.

To demonstrate the impact of surface reflectance on observed spectra, Figure 4.8A shows two reflected spectra through the exact same CH₄ concentration profile as observed by the same instrument with FWHM of 1.5 nm, but over a construction concrete compared to a vegetation surface. Evidently, not only do the observed spectra change in absolute value, but also their spectral variations are different within the fitting window, more complex for vegetation than for concrete. This exemplifies an important role that surface albedo plays in the retrieval, potentially interfering with the methane absorption lines. To further validate this point, Figure 4.8B shows examples of residuals from best spectral fits for each of these two spectra using IMAP-DOAS as described in Section 4.3, with a polynomial degree of 11. The noise level indicates the theoretical 1- σ noise level, expected from the instrument. In panel A, these residuals are hardly visible as they are close to the noise level. Clearly, the fit quality is different between the two surfaces as evidenced by a higher residual for reflected sunlight from the vegetation surface compared to a sample construction concrete. However, differences are subtle and might not be detectable if noise level are high or fewer detector pixels available. In practice, given an observed spectrum, our retrieval needs to differentiate the atmospheric feature from the surface feature in order to obtain the best estimate of methane enhancement with minimal bias and precision error. The performance of the retrieval will be influenced by the observing instrument as well as the representation of surface reflectance in our forward model.

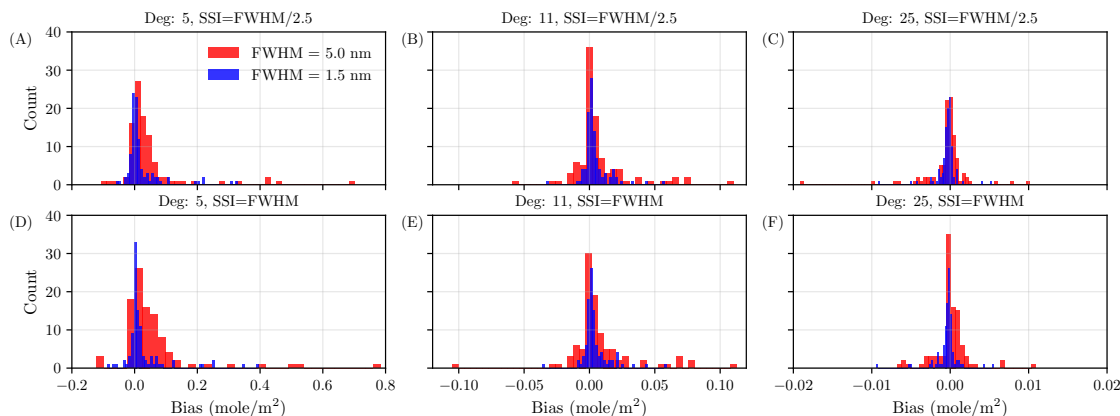


Figure 4.9: Plots showing a range of biases that occur over 100 randomly sampled surfaces when different FWHM, SSI, and polynomial degrees are used.

In this section, we performed the retrieval error analysis for different instrument parameters namely the FWHM and exposure (integration) times. Since the surface albedo is another important factor in the retrieval performance as shown in Figure 4.8, we also explored using different degrees in the polynomial terms in our forward model (see section 4.3), as a large number of polynomial degrees is required to capture the effect of surface albedo spectral variability (e.g. a polynomial degree of 11 still caused subtle yet systematic residuals for vegetation). For a given choice of instrument specification and polynomial degree, the IMAP-DOAS algorithm is performed to predict the column methane concentration, and thereby derive error estimates. We kept the true methane concentration fixed to a given vertical profile near the source emission with a flux rate of 200 kg h^{-1} . First, to illustrate potential bias that could arise from a variety of surfaces in real-world scenarios, we randomly selected 100 surfaces from our database and used each of them as a surface underlying the CH_4 column. By retrieving the observed radiance using different instrument FWHM and different number of polynomial degrees, we analyzed the range of resulting biases for each case. The bias distribution across the 100 surfaces are shown in Figure 4.9. When a polynomial degree of 5 is used in our retrieval, the range of biases observed is $(-0.2, 0.8) \text{ mole m}^{-2}$, compared to just within $(-0.15, 0.15)$ and $(-0.02, 0.02) \text{ mole m}^{-2}$ with a polynomial degree of 11 and 25, respectively. This result suggests that some surfaces interfere strongly with the retrieval, leading to very high biases when a low number of polynomial degrees is used, as this causes a forward model error. This implies that the use of a higher polynomial degree has a significant consequence in minimizing the bias in our retrieval results, especially

when we have no prior information about surfaces in the vicinity of emission sources. A polynomial degree of about 25 seems to capture most, but not all, surface effects. However, an instrument such as AVIRIS(-NG) only has 26 (52) detector pixels covering the entire fitting window, thus not allowing us to use such high polynomial degrees as it would render the problem under-determined. This clearly illustrates the problem in separating surface and atmospheric features at coarse spectral resolutions, as the problem becomes increasingly ill-posed with coarser spectral resolution. This is an integral part in obtaining reliable detection and quantification of local methane sources at a global scale, as is also shown later in Section 4.4. In general, an instrument with smaller FWHM leads to smaller observed biases as expected by its ability to capture more high-frequency CH_4 absorption features. Furthermore, with an SSI of $\text{FWHM}/2.5$, biases using higher polynomial degrees show a smaller range compared to the case with an $\text{SSI}=\text{FWHM}$, as surface features are harder to discern if atmospheric features are not oversampled. In the following analyses, we therefore primarily show the results from the case of $\text{SSI}=\text{FWHM}/2.5$, unless otherwise stated. This also fulfills the Nyquist sampling requirement for typical atmospheric retrievals, which might sometime involve spectral shifts. The impact of spectral shifts is ignored here, but would be another reason for both oversampling and higher spectral resolution.

Next, we investigated how the precision error varies with instrument parameters such as FWHM and the exposure (integration) time. While FWHM governs the shape of the methane Jacobians, the exposure time is an important factor determining potential spatial resolution and SNR. Figure 4.10 shows this relationship using a fixed exposure time of 20 ms with varying polynomial degrees on panel A and with fixed polynomial degree (25) and varying exposure time in panel B. Other parameters are set according to Table 4.1, and the underlying surface is a construction concrete (albedo index 1 in Figure 4.3). If we vary the polynomial degree, the impact on precision is negligible for $\text{FWHM}<0.5$ nm, very small for $\text{FWHM}<1.5$ nm, but diverging for $\text{FWHM}>2$ nm. The reason for this effect is that the polynomial degree determines which spectral variations can be purely attributed to methane and which might be caused by surface features, which eliminates its use to constrain methane. At fine spectral resolution, the methane fit is mainly driven by the atmospheric high frequency structure. Thus, the polynomial degree plays no significant role. At coarser spectral resolution, most atmospheric features are blurred and can be partially confused with the surface, causing a divergence of the precision error with increasing FWHM. A 1.5 nm FWHM still allows us to sample sufficient atmospheric

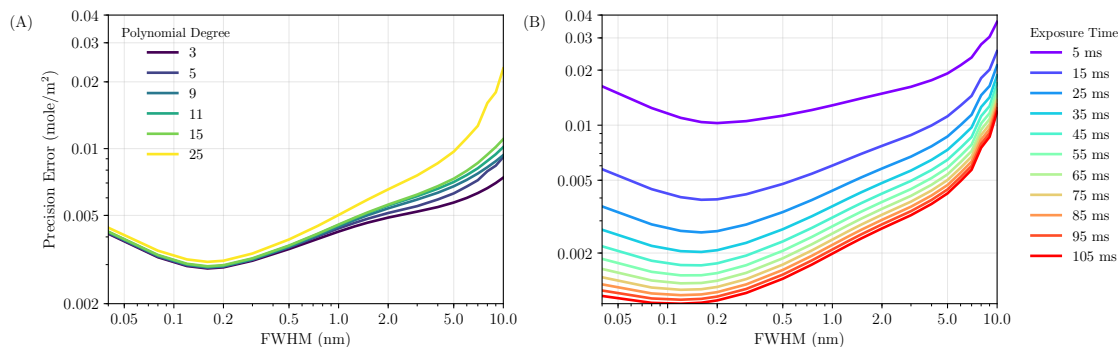


Figure 4.10: (A) Precision error as a function of instrument FWHM for different numbers of polynomial degrees used in the retrieval (with exposure time of 20 ms). (B) Precision error as a function of instrument FWHM for different exposure times (with polynomial degree of 25).

fine-structure to minimize the impact of surface interferences and will achieve sub-% precision error for a wide range of exposure times.

If we vary exposure times, the precision error decreases with the increase of the exposure time as the device can collect more photons resulting in an overall stronger signal. There exists a range of FWHM values that minimizes the precision error for each exposure time. Generally, the range lies between 0.1 - 0.3 nm. At low exposure times, readout noise becomes increasingly important and leads to a larger precision change when exposure times are varied. Thus, it is vital that an appropriate value of FWHM is chosen in order to achieve low precision error while we use a high degree of polynomial such as 25 in our retrieval to simultaneously reduce the bias from surface interferences. It is interesting to note that the FWHM with the best precision moves towards higher FWHM with decreasing exposure times, being a consequence of the increasing role of readout noise at the detector.

For example, using FWHM of 1.5 nm and exposure time of 25 ms, a precision error of 0.007 mole m⁻² can be achieved, which is about 1% of the background total column amount of 0.7 mole m⁻². In low-earth orbit with a satellite speed of 7 km s⁻¹, 25 ms corresponds to a spatial resolution of 175 m. Spacecraft nodding would allow us to slow down the effective ground-speed by about a factor 10, rendering a 1% total column precision for <20 m spatial resolution feasible from space using existing fast-readout SWIR detectors. This would be equivalent to measuring a pure methane layer of only 0.16 mm thickness.

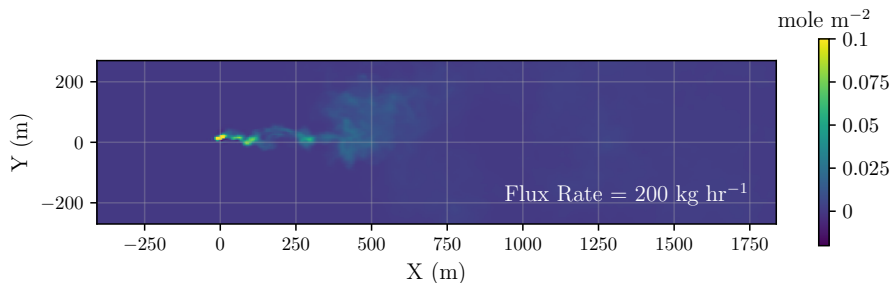


Figure 4.11: A nadir view of a simulated CH_4 plume from the LES with a prescribed flux rate of 200 kg h^{-1} . The background wind speed is 4 m s^{-1} along the x-axis.

2-D Retrieval over Realistic Surfaces

In the previous section, we analyzed the impact of surface interferences and instrument specifications on the quality of the CH_4 retrieval. The choice of parameters such as FWHM, exposure time, and the number of polynomial degrees leads to significantly different precision errors and biases. These errors in each retrieval column ultimately affect the detection and quantification of CH_4 source in 2-D scenes observed over various geographical areas across the globe. In this section, we illustrate how the retrieved CH_4 plume appears using different instruments and retrieval choices.

Occurrence of False Positives and False Negatives

To explore the 2-D pattern of a retrieved methane plume over a variety of realistic surfaces, we overlaid an LES simulated CH_4 plume on top of a checkerboard-styled land consisting of 30 surfaces. We then apply the instrument kernel and IMAP-DOAS algorithm to retrieve column CH_4 pixel by pixel across the 2-D scene. A combination of FWHM of 1.5 and 5.0 nm, with an SSI of FWHM/2.5, and polynomial degrees of 5, 11, 25, and 50 are adopted. A case of SSI=FWHM is also used for a FWHM of 5.0 nm, being equivalent to the AVIRIS-NG instrument. The emission rate of the CH_4 source is equal to 200 kg h^{-1} . The spatial distribution of the true CH_4 distribution is shown in Figure 4.11, showing local enhancements that can exceed 10% of the total background atmospheric column. The corresponding retrievals under different surfaces and instrument scenarios are shown in Figure 4.12. The deviation of predicted CH_4 from the true column value in each pixel is a combination of precision error and bias. In this result, the overall mean enhancement that emerges over each surface type in contrast to the true plume in Figure 4.11 could be interpreted as retrieval bias, while the presence of a speckle-like texture over each

surface can be viewed as the retrieval precision error driven by instrument noise for a given surface albedo (larger for dark surfaces). Meanwhile, the bias is related to systematic shift in the retrieved methane column enhancement from the true value due to surface interference in resolving the methane absorption features. In general, based on the visualization in these 2-D plots, the more the retrieved enhancement scene resemble the true CH₄ concentration map, the better the performance of the instrument and retrieval is. Specifically, when a low polynomial degree of 5 was used in the retrieval, we observed significant retrieval biases (both positive and negative) over various surfaces. Evidently, these biases can act to deceive the true location and enhancement of actual methane plume, especially if the surfaces have elongated shapes like a plume (not like a checkerboard here). As the number of polynomial degrees in the retrieval increases, the level of biases decreases over the scene enabling the actual methane plume enhancement to be better identified. This is also manifested in the reduced χ^2 values which describe how well an observed spectrum was fitted (the smaller, the better). As shown in Figure 4.13, the value of reduced χ^2 drops from 5 to become increasingly closer to 1 when a polynomial degree is changed from 5 to 11, 25, and 50. We note that the 10 surfaces in the bottom row of this checkerboard-styled tile from left to right are the 10 surfaces with their albedo spectral variations shown earlier in Figure 4.3. The Pink Quartzite (6th on the list of these 10 surfaces) is an extreme case where we see an unusually strong variation near 2.2 μm , resulting in a persisting bias even at a polynomial degree of 25. Nevertheless, generally when a polynomial degree of 25 is used, most of the biases across surfaces seem to disappear, but surprisingly complex surfaces such as Quartzite can occur across various natural landscapes and human-made surfaces in cities.

At the same time, using higher polynomial degrees result in higher precision errors as can be seen from the speckle-like texture in the retrieved scene. To illustrate how precision deteriorates as we increase the polynomial degree for a given instrument FWHM, Figure 4.14 shows the rise in precision error when using polynomial degrees of 50, 25, and 11 relative to using the polynomial degree of 5. We can clearly see that precision error deteriorates with a higher polynomial degree, particularly at coarser FWHM. This is consistent with what we observed earlier. Based on this analysis, we found that using an instrument with a FWHM of 1.5 nm would allow for higher polynomial degrees such as 25 to be utilized with a relatively small increase in precision error. For an instrument with a FWHM of 5 nm, using a polynomial degree of 25 or 50 results in a larger precision error increase, underlining the

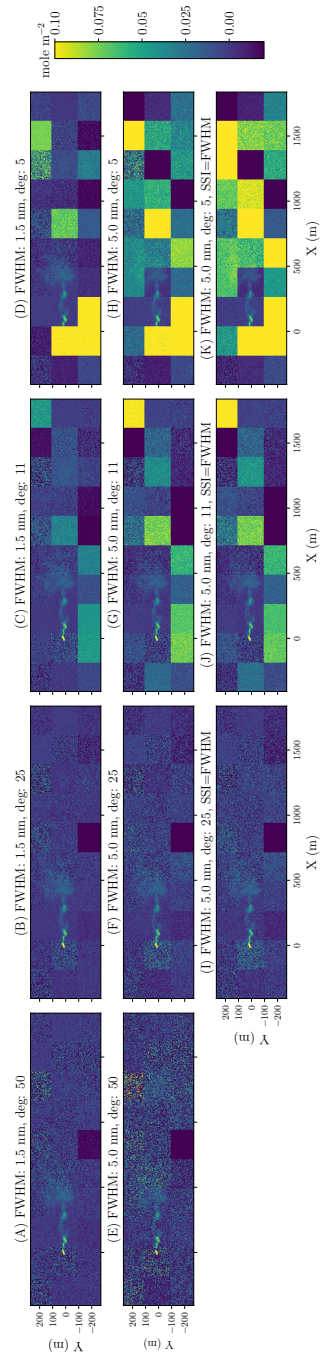


Figure 4.12: Retrieved CH_4 column over 30 different surfaces with varying instrument scenarios. The first row shows the results for an instrument with FWHM of 1.5 nm, while the second row shows the results for an instrument with FWHM of 5.0 nm. Both the first and second rows have $\text{SSI}=\text{FWHM}/2.5$. The third row shows the results for an instrument with FWHM of 5.0 nm and $\text{SSI}=\text{FWHM}$. The biases drop significantly as polynomial degrees increase.

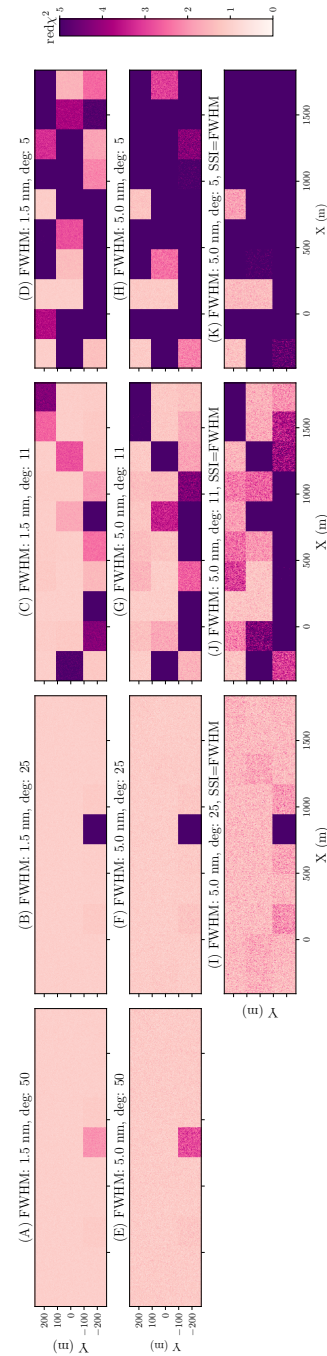


Figure 4.13: A plot showing the values of reduced χ^2 from the retrieval of different instrument FWHM and polynomial degrees. As the polynomial degree becomes higher, the reduced χ^2 decreases, implying a better spectral fit.

potential problems that could occur when complex surface albedo features exist. The main physical reason for the deterioration of precision for low spectral resolution instruments is that a lower degree polynomial in the fitting routine is equivalent to

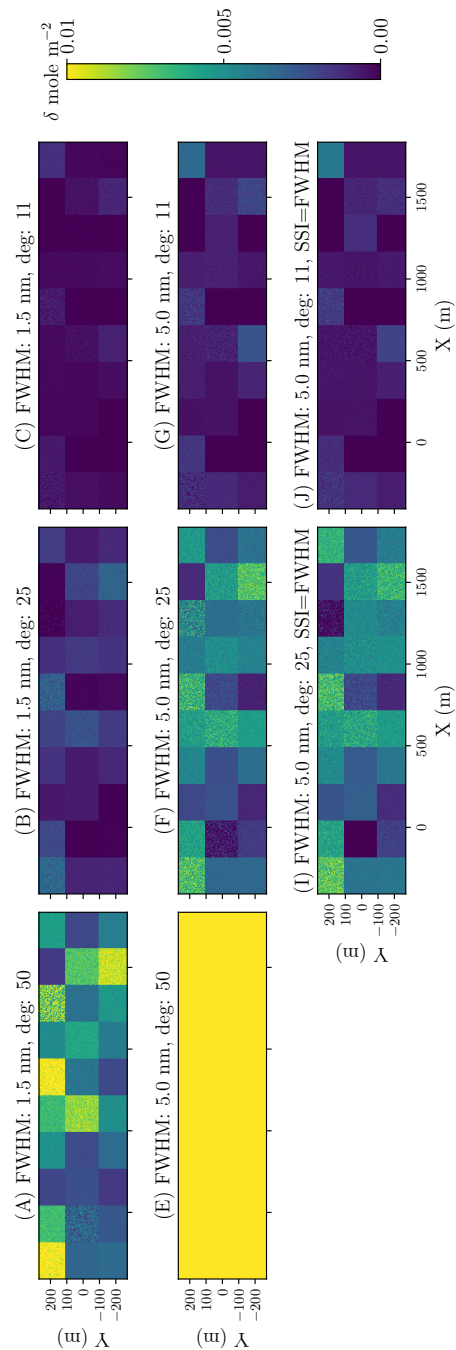


Figure 4.14: The increase in precision errors when the polynomial degrees of 50, 25, and 11 are used as compared to the polynomial degree of 5 case. The increase is computed for a given FWHM and SSI according to each row.

a hard a priori constraint that only spectrally smooth surfaces exist. The retrieval itself then attributes some of the broad-band variations in the methane Jacobian to be only attributable to changes in methane, not surface albedos, thus providing a

tighter constraint on the methane abundances. For higher resolution instruments, most of the information content for methane is located within the fine-structure of the methane absorption lines and less on the broad-band variations, causing a much smaller increase in the precision errors if higher polynomial degrees are used.

These results indicate that a narrow FWHM (such as 1.5 nm) and a high number of polynomial degree (at least 25) are needed to reduce both precision errors and biases due to surface interference. This way we can obtain a higher-quality retrieved scene in order to effectively identify and quantify emission sources over the majority of the surfaces. If low polynomials are used, high biases are likely to occur over certain surface types. These can cause false positives or negatives in the observational systems, complicating the analysis of the locations and the emission rates of the CH₄ sources. This can cause a significant problem for both human analysts as well as AI models (Jongramrungruang et al., 2021 (in review)) that rely on the spatial distribution of observed enhancement to make predictions.

To further show an example over a real-world high emission area, we queried a realistic surface distribution over a well pad in the Durango area, Colorado from LANDSAT. At each location, this dataset provides surface albedos at the wavelengths of 0.48, 0.56, 0.65, 0.87, 1.61, and 2.20 μm . The RGB image of this particular location and its corresponding albedo near 2.2 μm are shown in Figure 4.15. Based on the albedos in the 7 bands available in this LANDSAT scene at each pixel, we found the best matching surface in our high-resolution surface database from the ECOSTRESS spectral library. We used this surface to simulate a semi-realistic CH₄ scene with an emission emerging from the ground in the vicinity of a well pad. The retrieved CH₄ enhancement is shown in Figure 4.16. Once again, when an instrument with FWHM of 5.0 nm is used in conjunction with a low polynomial degree of 5, high biases occur over most surfaces across the area. In particular, oil shale and sandstone are the two surfaces that exhibit strong surface interference

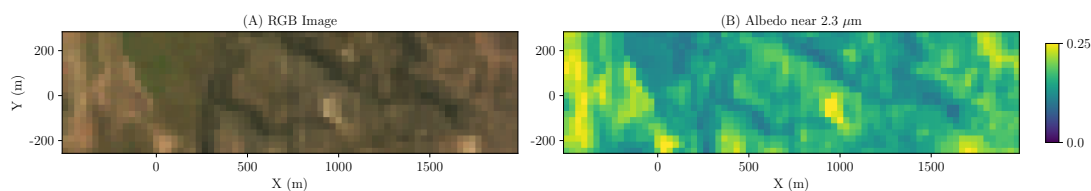


Figure 4.15: RGB and 2.2 μm albedo images of a realistic surface distribution in the Durango area, Colorado from LANDSAT.

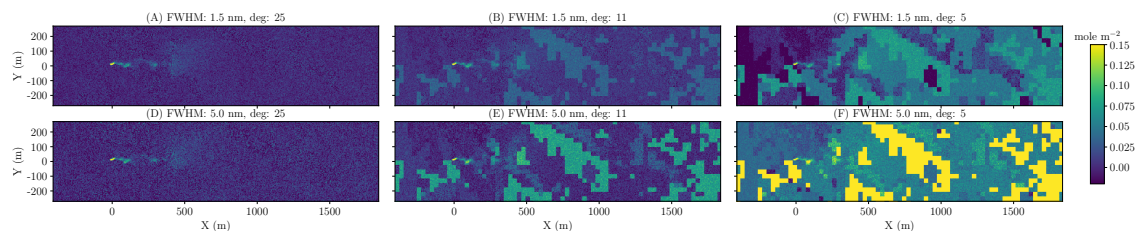


Figure 4.16: Retrieved CH_4 column over a well pad in the Durango area, Colorado with varying instrument FWHM and polynomial degrees in the retrieval. The realistic surface distribution is based on LANDSAT data. The use of the polynomial degree of 25 and FWHM of 1.5 nm can reduce biases and precision error over this scene.

as observed in Figure 4.16(F). Evidently, the resulting bias occurs at a level that dwarfs the true plume enhancement rendering it impossible to identify the location of the emission sources, let alone the ability to obtain an accurate quantification of total emission in the area. However, by using a higher polynomial degree of 25, the biases across surfaces is greatly reduced, albeit with slightly higher noise. Nonetheless, this noise is reduced when FWHM decreases from 5.0 nm to 1.5 nm. We note that this reduction in precision error, when we decrease the instrument with a FWHM from 5.0 to 1.5 nm, could be even more apparent over some other surfaces with lower albedos compared to the ones in this scene. Visually, we can already see that the actual CH_4 plume in terms of its location and strength can be much more easily identified and distinguished from the surface artefacts with the FWHM of 1.5 nm and polynomial degree 25. This finding demonstrates how achieving low bias and precision error in the observation and the retrieval process across diverse surfaces profoundly benefit the detection and quantification of true CH_4 sources. This analysis provides an insight on how future instruments can be designed to enable an effective and accurate CH_4 source detection and quantification across the globe. In the next section, we further illustrate retrieval performance when a local CH_4 plume of various emission rates is observed by an instrument with a higher spatial resolution such as 30 m.

Effect of Spatial Resolutions and Flux Rates

In the previous section, we have shown a 2-D retrieved scene assuming that an observing instrument has a spatial resolution of 5 m. In this section, we repeated the 2-D scene retrieval analysis with a spatial resolution of 30 m by averaging the reflected sunlight through a CH_4 plume simulated at 5 m spatial resolution into 30 m

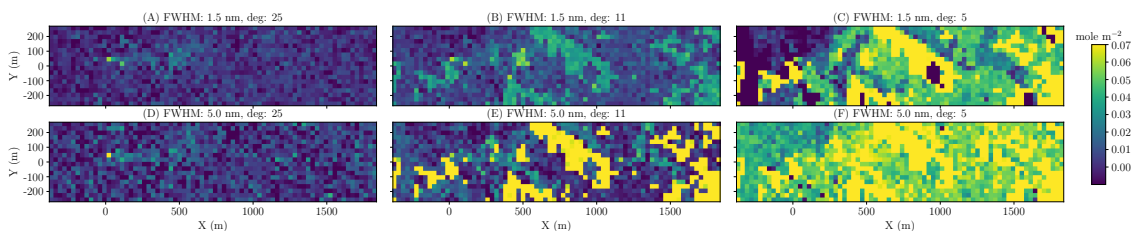


Figure 4.17: A plot similar to Figure 4.16, but at 30m resolution. Retrieved CH_4 column over a well pad in the Durango area, Colorado area with varying instrument FWHM and polynomial degrees in the retrieval. The realistic surface distribution is based on LANDSAT data. The use of the polynomial degree of 25 and FWHM of 1.5 nm can reduce biases and precision errors across the scene.

spatial resolution prior to applying an instrument operator. We present this analysis with this design consideration for the 30-m spatial resolution and the exposure time of 40 ms to evaluate the potential of future spectrometers on-board satellites in the coming years. The 2-D scenes retrieved at 30-m spatial resolution by instruments of different FWHM and polynomial degrees are illustrated in Figure 4.17. The choice of FWHM of 1.5 nm and a polynomial degree of 25 remains very effective in removing surface biases across the scene and the location of CH_4 plume can be distinguished. It is important to note, however, that the retrieved CH_4 column concentration near the source pixels becomes more diluted as the spatial resolution decreases. This is because the local CH_4 plume distribution at an emission rate such as 200 kg hr^{-1} varies greatly on scales of just a few meters. Having demonstrated that an instrument with a FWHM of 1.5 nm and a polynomial degree of 25 can significantly reduce precision error and biases due to surface interference, we use this setup to investigate how the 2-D retrieved scenes look like for sources of different emission rates to understand the lower limit of CH_4 emission rates that can potentially still be detected.

The retrieved scenes for CH_4 emission rates from 50 to 2000 kg h^{-1} are shown in Figure 4.18, and the corresponding scenes showing the ratio of retrieved methane concentration and precision error in each pixel are given in Figure 4.19. The ratio, n , of pixel enhancement to precision error represents a $n-\sigma$ probability event that this pixel enhancement would have randomly happened, purely due to noise, in the absence of a true CH_4 . A ratio value above 4 would imply that there is only a probability of lower than 1 in 15000 that this would happen by chance due to random noise. Thus the ratio of 4 can be a simple and useful metric to imply where actual CH_4 enhancement pixels are. Based on this metric, we found that CH_4 source

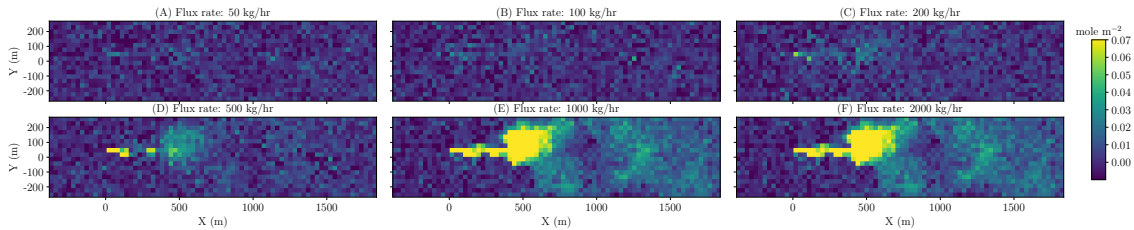


Figure 4.18: Retrieved CH_4 column over a well pad in the Durango area, Colorado area for plumes of various emission rates. The spatial resolution is 30 m, the instrument FWHM is 1.5 nm, and the polynomial degree in the retrieval is 1.5. The realistic surface distribution is based on LANDSAT data. Column enhancement in the vicinity of CH_4 plume is increasingly visible as the source emission rate becomes larger.

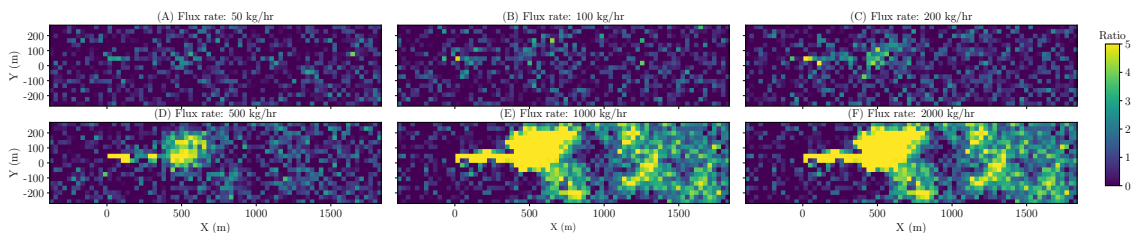


Figure 4.19: Ratio of retrieved CH_4 excess column divided by the posterior precision error, over a simulated scene in the Durango area, Colorado area for plumes of various emission rates. The spatial resolution is 30 m, the instrument FWHM is 1.5 nm, and the polynomial degree in the retrieval is 25. The realistic surface distribution is based on LANDSAT data. Ratios higher than 4 imply a probability of lower than 1 in 15000 that the pixel enhancement happens by random noise.

detection can still be possible for plumes with emission rates as low as approximately $50\text{-}100 \text{ kg h}^{-1}$.

4.5 Conclusion

We built an end-to-end modeling framework that can simulate radiances from reflected sunlight through methane plumes over a variety of surfaces. In this study, we simulated a realistic 3-D CH_4 concentration field from a point source using an LES, and varied the underlying surfaces where the emission occurs using a comprehensive surface albedo database from the ECOSTRESS spectral library consisting of over 2000 surface types. The observed radiances and their noise-equivalent spectral radiance for various instrument configurations are modelled directly as a function of incoming radiance and instrument parameters such as the FWHM of the line-shape function and integration time, without having to prescribe the SNR a priori.

Based on the modelled radiance, we applied the IMAP-DOAS algorithm to retrieve methane column enhancements.

We compared the tradeoff between the two most frequently used fitting windows for CH₄ in the 1.6 and 2.3 μm ranges. Our analysis has shown that despite a higher solar radiance near 1.6 μm , the stronger absorption feature of CH₄ near 2.3 μm leads to a consistently lower precision error for the 2.3 μm fitting band. The rare occasion of a 1.6 μm fitting window outperforming the 2.3 μm retrieval band happens only when both FWHM is lower than 0.2 nm and simultaneously a surface in consideration has a much higher albedo near 1.6 compared to 2.3 μm . For the purpose of building an instrument to detect methane emission accurately at sufficiently fine spatial resolutions across most global surfaces, we believed that the 2.3 μm band can perform better and should be prioritized in most scenarios. We primarily considered the fitting window in the 2120–2395 nm range to study the impact of instrument parameters and retrieval choices on the retrieval bias and precision error.

To highlight the impact of surface interferences, the number of polynomial degrees is varied in the IMAP-DOAS retrieval experiments. This framework allows us to derive the corresponding precision error and bias when different sets of instrument parameters and the number of polynomial degrees are used in the retrieval of CH₄ column concentration. Our analysis shows that the number of polynomial degrees used to represent surface spectral variations in the retrieval algorithm has a significant impact on the bias of the retrieved methane columns causing a positive bias as large as 0.8 mole m⁻² for retrieval with a polynomial degree of 5 compared to 0.2 and only 0.02 mole m⁻² for degrees of 11 and 25, respectively, across the majority of surfaces. Using a higher polynomial degree, however, is found to simultaneously increase precision error for methane retrieval as this relaxes the constraints on possible methane absorption contribution in spectral variations of the observed radiance. This is particularly evident at FWHM greater than 2 nm. Thus, using an instrument with a lower FWHM such as 1.5 nm will allow for a high number of polynomial terms to be used while inducing a smaller deterioration in precision error. For example, we found that an instrument with FWHM of 1.5 nm and the exposure time of 20 ms can achieve a precision error of less than 0.007 mole m⁻² (or less than 1.0% of the total column in the atmosphere) over a typical construction concrete surface with an albedo of 0.35, even when a polynomial degree of 25 is used.

Having low bias in the retrieval is integral to removing correlated surface features in the retrieval enhancement map. These surface features from retrieval errors likely appear as false positives and subsequently cause significant impacts on the detection and quantification of true CH₄ sources. To demonstrate the significance of surface interferences, we used a realistic surface distribution over a well pad from the Durango area, Colorado, as a background surface with an LES methane plume of 200 kg h⁻¹ to create a synthetic emission in a real world environment. Our results illustrated that when an instrument of high FWHM (such as 5 nm) is used with a low polynomial degree (such as 5), a large retrieval bias appears broadly across the 2-D scene. These interferences occur severely over surfaces such as oil shale and sandstone, resulting in difficulties to clearly distinguish a true plume from areas of systematic biases. Nevertheless, by using a lower FWHM value such as 1.5 nm and the polynomial degree of at least 25, we have illustrated the ability to obtain low retrieval bias across the entire scene and to effectively differentiate the source location from the background. We also repeated the 2-D retrieval analysis for 30-m spatial resolution by averaging the radiance per unit area from 5 m² to 30 m², and adjusted the exposure time to 40 ms which could be achievable for future satellites. Again, our results have shown that using FWHM of 1.5 nm and a polynomial degree of 25 plays a crucial role in resolving surface features and removing false positives, ultimately enabling the ability to distinguish the true emission location. In the absence of bias, the ratio of retrieved column enhancement and the retrieval precision error in our retrieved 2-D scenes indicates that it might be possible to detect a CH₄ emission source with a flux rate as low as 50-100 kg h⁻¹.

This study highlights the effect of changing instrument FWHM, exposure times, and the polynomial degree on minimizing retrieval errors. The FWHM and exposure time are intrinsic to how a spectrometer is designed, as opposed to describing a spatial resolution which depends on external factors such as the viewing geometry and the speed of a remote-sensing platform. Further studies will be required to translate how these variables are implemented into an observing system that can achieve specific spatial resolutions of interest. Additional considerations such as the device saturation constraint will also influence the ultimate achievable exposure time for a newly designed instrument. Our end-to-end simulator that includes an instrument model and retrieval can be generalized to study the performance of future instruments with specific engineering requirements.

The findings in this study can inform future satellite instrument designs and the

retrieval algorithm in order to have robust observations capable of separating real plumes from surface interference. Reducing both bias and precision error can have a profound benefit both for manual analysis by humans and for automated plume detection models such as an Artificial Neural Network approach. This will enable the analytic chain to have a higher accuracy and level of confidence detecting and quantifying more subtle methane sources from observed scenes across large geographical areas.

The modelling framework in this work could also be generalized to improve the detection and quantification of CO₂, with minor modifications on a different fitting window and a different magnitude of flux rate in the emission simulations.

Chapter 5

CONCLUSIONS

This thesis presents novel methods to achieve an accurate and automated detection and quantification of methane point source emissions from remote-sensing measurements. It solves the two most significant problems that exist in using retrieved methane column enhancement to locate and quantify individual emission point sources across large geographical areas: wind speed uncertainties and appearances of retrieval interferences from surface spectral variations.

In Chapter 2, we first show that a realistic LES modeling is much more appropriate than simple Gaussian plume assumptions for optimizing flux inversions for individual point sources based on retrieved methane column enhancement distributions. We thus use LES to simulate realistic plume distributions evolving in time and space from a point source of different flux rates under various background wind speeds and surface heat fluxes. This allows us to generate synthetic 2-D airborne observations based on the AVIRIS-NG column averaging kernel and precision estimate to study the relationship between the 2-D plume shape, the flux rates, and the wind speeds. Our analysis shows that the angular width of the plume negatively correlates with the wind speed, allowing us to deduce the wind speed from the plume shape itself. Based on the connection between plume shape and wind speed, together with the integrated methane enhancement (IME) over the plume, we can infer the source flux rate based solely on an observed snapshot of the plume since it provides both the IME and the spatial distribution of the column enhancements. This enables the quantification of the source emission rate directly from a plume image without relying on any ancillary data such as local wind speed measurements. Our error analysis of this method applied on randomly generated snapshots of various flux rates in the range of 10–1000 kg h⁻¹ showed an error of around 30% on average for an individual point-source estimate. We also performed an error analysis for aggregated flux estimates from 30 plumes by using bootstrap sampling, and found the aggregation error estimate to be in the range of less than 10%. This provides a significant improvement from other preexisting approaches that rely on wind data, for which reliable meteorological reanalysis data might not be available at high spatial resolution everywhere. In this chapter, we demonstrate the ability to estimate flux rates of methane point sources based solely on the remotely sensed column

methane enhancement without the need for ground measurements or weather re-analysis data. The results in Chapter 2 provided insights that the morphology of methane plumes, as observed from remote sensing images, contains useful information about the background wind speed during the observations, which, in turn, is a critical component of predicting accurate flux estimates.

In Chapter 3, we go beyond just a simple IME and plume angular width to utilize the full spatial structure of the plume morphology such that emission rates are predicted at even higher accuracy, as well as in a more automated manner. To achieve this, we develop a customized CNN model, named MethaNet, that maps 2-D plume images and their corresponding source emission rates under various wind speed conditions. The training data are derived from realistic plume simulation using LES and realistic retrieval noise from AVIRIS-NG field observations. Our simulated CH₄ images represent a diverse set of realistic plumes of various emission rates between 0-2000 kg h⁻¹ in different landscapes ranging from urban, desert to agriculture areas. The predictions of emission rates by MethaNet on unseen plumes has a mean absolute percentage error of approximately 17 % for plumes with emission rates above 40 kg h⁻¹. For smaller plumes with emission rates under 40 kg h⁻¹, the model appears to be less accurate under a situation where the background noise is higher and spatially correlated. Under such scenarios, systematic background noise can interfere with the small methane enhancements. If we also account for small plumes, the model can still predict with an error of approximately 22 %. This level of performance for quantifying methane emission rate is a state-of-the-art achievement for an approach that does not rely on wind speed information. An independent test on a controlled release experiment data over Victorville, CA, also validates a consistent prediction performance for MethaNet within one standard deviation in real observations. While we trained our CNN model on predicting plume emission rates from observations at a spatial resolution of 5 m from an airborne instrument such as AVIRIS-NG, our general modelling framework can be applicable to observations at different spatial resolution and instrument sensitivity. For a new instrument at different spatial resolution, the model should be retrained using new training data by applying the new instrument column averaging kernel to the LES 3-D output to generate a new dataset of 2-D plume scenes that would be observed under such an instrument. The error characteristics of the new instrument measurements should also be incorporated to inform the choice of noise characteristics in the simulated plume images used in the training process. Our analyses in Chapter 3 also found that high and correlated noise from the retrieval process due to surface interferences

can greatly affect the predictions of smaller methane plumes. This hints to an important aspect, namely the need to develop instruments and methods to minimize and randomize retrieval noise such that a predictive model on retrieved plume images can perform optimally. This crucial problem is at the heart of the study in Chapter 4.

In Chapter 4, we perform a comprehensive instrument trade-off analysis to study the level of retrieval precision errors and biases that are incurred from using different instrument spectral resolutions, optical performance and detector exposure times, as well as different numbers of polynomial degrees to capture the surface spectral variations in the retrieval process. We build an end-to-end modeling framework that can simulate radiances from reflected sunlight through methane plumes over a variety of surfaces. The observed radiances and their noise-equivalent spectral radiance for various instrument configurations are modelled directly as a function of incoming radiance and instrument parameters such as the FWHM of the lineshape function and integration time, without having to prescribe the SNR a priori. Based on the modelled radiance, we apply the IMAP-DOAS algorithm to retrieve methane column enhancements and derive the resulting precision errors and biases. Using this model, we arrive at various important findings. First, we compare the tradeoff between the two most frequently used fitting windows for CH₄ in the 1.6 and 2.3 μm ranges and show that the 2.3 μm band can perform better and should be prioritized in most scenarios. Second, we find that very high biases occur when a low number of polynomial degrees such as 5 is used, whereas the use of a higher polynomial degree such as 25 has a significant consequence in minimizing the bias in our retrieval results, especially when we have no prior information about surfaces in the vicinity of emission sources. Third, using a higher polynomial degree is found to simultaneously increase precision error for methane retrieval, particularly at FWHM of greater than 2 nm. Thus, using an instrument with a lower FWHM such as 1.5 nm will allow for a high number of polynomial terms to be used while inducing a smaller deterioration in precision error. For example, we find that an instrument with FWHM of 1.5 nm and the exposure time of 20 ms can achieve a precision error of less than 0.007 mole m⁻² (or less than 1.0% of the total column in the atmosphere) over a typical construction concrete surface with an albedo of 0.35, even when a polynomial degree of 25 is used. To demonstrate the significance of our findings towards differentiating actual methane plumes from false positives, we create a synthetic emission in a real world environment by using a realistic surface distribution over a well pad from the Durango area, Colorado as a background surface

with an LES methane plume of 200 kg h^{-1} . By using a lower FWHM value such as 1.5 nm and the polynomial degree of at least 25, we illustrated the ability to obtain low retrieval bias across most surfaces and to effectively differentiate the source location from the background. This highlights the effect of changing instrument FWHM, exposure times and the polynomial degree on minimizing retrieval errors. The findings in this chapter can inform future satellite instrument designs and the retrieval algorithm in order to have robust observations capable of separating real plume enhancements from surface interferences. The methods we have developed in Chapter 2, 3, and 4 can also be generalized to CO_2 emissions such as those from power plants with minor modifications on a different fitting window, a change in the instrument column averaging kernel used to simulate total column enhancement, and a different range of flux rates in the emission simulations.

Together, these results provide a framework for accurately and effectively identifying and quantifying CH_4 point sources based on remote-sensing observations which will become increasingly available across the globe. A path towards the future of a global monitoring system with accurate and automated methane emissions detection and quantification is made open, and that future is not far away.

BIBLIOGRAPHY

- Ayasse, A. K. et al. (2019). “Methane Mapping with Future Satellite Imaging Spectrometers”. In: *Remote Sensing* 11.24. ISSN: 2072-4292. DOI: 10.3390/rs11243054. URL: <https://www.mdpi.com/2072-4292/11/24/3054>.
- Benjamin, S. G. et al. (2016). “A North American hourly assimilation and model forecast cycle: The rapid refresh”. In: *Monthly Weather Review* 144.4, pp. 1669–1694. ISSN: 15200493. DOI: 10.1175/MWR-D-15-0242.1.
- Bergamaschi, P. et al. (2013). “Atmospheric CH₄ in the first decade of the 21st century: Inverse modeling analysis using SCIAMACHY satellite retrievals and NOAA surface measurements”. In: *Journal of Geophysical Research* 118.13. ISSN: 21698996. DOI: 10.1002/jgrd.50480.
- Bousquet, P. et al. (2011). “Source attribution of the changes in atmospheric methane for 2006–2008”. In: *Atmospheric Chemistry and Physics* 11.8, pp. 3689–3700. ISSN: 16807316. DOI: 10.5194/acp-11-3689-2011.
- Bovensmann, H. et al. (2010). “A remote sensing technique for global monitoring of power plant CO₂ emissions from space and related applications”. In: *Atmospheric Measurement Techniques* 3.4, pp. 781–811. ISSN: 18671381. DOI: 10.5194/amt-3-781-2010.
- Bradley, E. S. et al. (2011). “Detection of marine methane emissions with AVIRIS band ratios”. In: *Geophysical Research Letters* 38.10.
- Brandt, A. R. et al. (2014). “Methane leaks from North American natural gas systems”. In: *Science* 343.6172, pp. 733–735. ISSN: 10959203. DOI: 10.1126/science.1247045.
- Briggs, G. (1973). “Diffusion estimation for small emissions”. In: *Atmospheric turbulence and diffusion laboratory, National Oceanic and Atmospheric Administration ATDL* contr.
- Cambaliza, M. O. et al. (2014). “Assessment of uncertainties of an aircraft-based mass balance approach for quantifying urban greenhouse gas emissions”. In: *Atmospheric Chemistry and Physics* 14.17, pp. 9029–9050. ISSN: 16807324. DOI: 10.5194/acp-14-9029-2014.
- Cambaliza, M. O. et al. (2015). “Quantification and source apportionment of the methane emission flux from the city of Indianapolis”. In: *Elementa* 3, pp. 1–18. ISSN: 23251026. DOI: 10.12952/journal.elementa.000037.
- Collins, M. et al. (2013). “Long-term climate change: Projections, commitments and irreversibility”. In: *Climate Change 2013: The Physical Science Basis. Contribution of Working Group I to the Fifth Assessment Report of the Intergovernmental Panel on Climate Change*. Ed. by T. F. Stocker et al. Cambridge, UK: Cambridge University Press, pp. 1029–1136. DOI: 10.1017/CB09781107415324.024.

- Conley, S. et al. (2016). “Methane emissions from the 2015 Aliso Canyon blowout in Los Angeles, CA”. In: *Science* 351.6279, pp. 1317–1320. ISSN: 10959203. DOI: 10.1126/science.aaf2348.
- Cusworth, D. H. et al. (2019). “Potential of next-generation imaging spectrometers to detect and quantify methane point sources from space”. In: *Atmospheric Measurement Techniques* 12.10, pp. 5655–5668. ISSN: 18678548. DOI: 10.5194/amt-12-5655-2019.
- Cusworth, D. H. et al. (2021). “Intermittency of Large Methane Emitters in the Permian Basin”. In: *Environmental Science & Technology Letters* 0.0, null. DOI: 10.1021/acs.estlett.1c00173. eprint: <https://doi.org/10.1021/acs.estlett.1c00173>. URL: <https://doi.org/10.1021/acs.estlett.1c00173>.
- Dlugokencky, E. (2021). “Trends in atmospheric methane”. In: *NOAA/GML (gml.noaa.gov/ccgg/trends_ch4/)*.
- Duren, R. M. et al. (2019). “California’s methane super-emitters”. In: *Nature* 575.7781, pp. 180–184. ISSN: 14764687. DOI: 10.1038/s41586-019-1720-3. URL: <http://dx.doi.org/10.1038/s41586-019-1720-3>.
- Frankenberg, C. et al. (2005a). “Assessing methane emissions from global spaceborne observations”. In: *Science* 308.5724, pp. 1010–1014. ISSN: 00368075. DOI: 10.1126/science.1106644.
- Frankenberg, C. et al. (2005b). “Iterative maximum a posteriori (IMAP)-DOAS for retrieval of strongly absorbing trace gases: Model studies for CH₄ and CO₂ retrieval from near infrared spectra of SCIAMACHY onboard ENVISAT”. In: *Atmospheric Chemistry and Physics* 5.1, pp. 9–22. DOI: 10.5194/acp-5-9-2005. URL: <https://acp.copernicus.org/articles/5/9/2005/>.
- (2005c). “Retrieval of CO from SCIAMACHY onboard ENVISAT: detection of strongly polluted areas and seasonal patterns in global CO abundances”. In: *Atmospheric Chemistry and Physics*. ISSN: 1680-7324. DOI: 10.5194/acp-5-1639-2005.
- Frankenberg, C et al. (2011). “Global column-averaged methane mixing ratios from 2003 to 2009 as derived from SCIAMACHY: Trends and variability”. In: *Journal of Geophysical Research* 116.4. ISSN: 01480227. DOI: 10.1029/2010JD014849.
- Frankenberg, C. et al. (2016). “Airborne methane remote measurements reveal heavy-tail flux distribution in Four Corners region”. In: *Proceedings of the National Academy of Sciences* 113.35, pp. 9734–9739. ISSN: 0027-8424. DOI: 10.1073/pnas.1605617113. URL: <http://www.pnas.org/lookup/doi/10.1073/pnas.1605617113>.
- Gerilowski, K et al. (2011). “MAMAP—a new spectrometer system for column-averaged methane and carbon dioxide observations from aircraft: instrument description and performance analysis”. In: *Atmospheric Measurement Techniques* 4.2, pp. 215–243.

- Gordon, I. E. et al. (2017). “The HITRAN2016 molecular spectroscopic database”. In: *Journal of Quantitative Spectroscopy and Radiative Transfer* 203, pp. 3–69.
- Gordon, M. et al. (2015). “Determining air pollutant emission rates based on mass balance using airborne measurement data over the Alberta oil sands operations”. In: *Atmospheric Measurement Techniques* 8.9, pp. 3745–3765. ISSN: 18678548. DOI: 10.5194/amt-8-3745-2015.
- Gorelick, N. et al. (2016). “Methane emissions from the 2015 Aliso Canyon blowout in Los Angeles, CA”. In: *Atmospheric Measurement Techniques* 16.10, pp. 5673–5686. ISSN: 18678548. DOI: 10.1126/science.aaf2348. URL: <http://dx.doi.org/10.1038/s41586-019-0912-1><http://dx.doi.org/10.1038/s41598-020-57678-4><http://dx.doi.org/10.1038/s41586-019-1720-3>[http://www.atmos-meas-tech.net/4/1735/2011/http://file//localhost\(null\)papers3://publication/uuid/F1B187DB-BCF1-4ED9-9F1](http://www.atmos-meas-tech.net/4/1735/2011/http://file//localhost(null)papers3://publication/uuid/F1B187DB-BCF1-4ED9-9F1).
- Gouw, J. A. de et al. (2020). “Daily Satellite Observations of Methane from Oil and Gas Production Regions in the United States”. In: *Scientific Reports* 10.1, pp. 1–10. ISSN: 20452322. DOI: 10.1038/s41598-020-57678-4. URL: <http://dx.doi.org/10.1038/s41598-020-57678-4>.
- Gurney, K. R. et al. (2019). “The Hestia fossil fuel CO₂ emissions data product for the Los Angeles megacity (Hestia-LA)”. In: *Earth System Science Data* 11.3, pp. 1309–1335. DOI: 10.5194/essd-11-1309-2019. URL: <https://essd.copernicus.org/articles/11/1309/2019/>.
- Hamlin, L. et al. (2011). “Imaging spectrometer science measurements for terrestrial ecology: AVIRIS and new developments”. In: *IEEE Aerospace Conference Proceedings*, pp. 1–7. ISSN: 1095323X. DOI: 10.1109/AERO.2011.5747395.
- He, K. et al. (2016). “Deep residual learning for image recognition”. In: *Proceedings of the IEEE Computer Society Conference on Computer Vision and Pattern Recognition 2016-Decem*, pp. 770–778. ISSN: 10636919. DOI: 10.1109/CVPR.2016.90. arXiv: 1512.03385.
- Houweling, S. et al. (2017). “Global inverse modeling of CH₄ sources and sinks : an overview of methods”. In: pp. 235–256. DOI: 10.5194/acp-17-235-2017.
- Hsu, Y. K. et al. (2010). “Methane emissions inventory verification in southern California”. In: *Atmospheric Environment* 44.1, pp. 1–7. ISSN: 13522310. DOI: 10.1016/j.atmosenv.2009.10.002. URL: <http://dx.doi.org/10.1016/j.atmosenv.2009.10.002>.
- Hu, H. et al. (2018). “Toward Global Mapping of Methane With TROPOMI: First Results and Intersatellite Comparison to GOSAT”. In: *Geophysical Research Letters* 45.8, pp. 3682–3689. ISSN: 19448007. DOI: 10.1002/2018GL077259.

- Hulley, G. C. et al. (2016). “High spatial resolution imaging of methane and other trace gases with the airborne Hyperspectral Thermal Emission Spectrometer (HyTES)”. In: *Atmospheric Measurement Techniques Discussions* 2016.5, pp. 1–32. ISSN: 18678548. DOI: 10.5194/amt-9-2393-2016. URL: <http://www.atmos-meas-tech-discuss.net/amt-2016-8/amt-2016-8.pdfpapers3://publication/uuid/684D8035-FF12-4494-A860-1DB30125DD76><http://www.atmos-meas-tech-discuss.net/amt-2016-8/papers3://publication/doi/10.5194/amt-2016-8>.
- Jacob, D. et al. (2016). “Satellite observations of atmospheric methane and their value for quantifying methane emissions”. In: *Atmospheric Chemistry and Physics* 16.22. ISSN: 16807324. DOI: 10.5194/acp-16-14371-2016.
- Jongaramrungruang, S. et al. (2019). “Towards accurate methane point-source quantification from high-resolution 2-D plume imagery”. In: *Atmospheric Measurement Techniques* 12.12. ISSN: 18678548. DOI: 10.5194/amt-12-6667-2019.
- Kort, E. A. et al. (2016). “Fugitive emissions from the Bakken shale illustrate role of shale production in global ethane shift”. In: *Geophysical Research Letters* 43.9, pp. 4617–4623. ISSN: 19448007. DOI: 10.1002/2016GL068703.
- Kort, E. A. and C. Frankenberg (2014). “Anomaly Viewed From Space”. In: *Geophysical Research Letters*, pp. 6898–6903. DOI: 10.1002/2014GL061503. Received.
- Kort, E. A. et al. (2008). “Emissions of CH₄ and N₂O over the United States and Canada based on a receptor-oriented modeling framework and COBRA-NA atmospheric observations”. In: *Geophysical Research Letters* 35.18, pp. 1–5. ISSN: 00948276. DOI: 10.1029/2008GL034031.
- Krings, T et al. (2013). “Quantification of methane emission rates from coal mine ventilation shafts using airborne remote sensing data”. In: *Atmospheric Measurement Techniques* 6.1, pp. 151–166. URL: [http://www.atmos-meas-tech.net/6/151/2013/http://file//localhost\(null\)papers3://publication/doi/10.5194/amt-6-151-2013](http://www.atmos-meas-tech.net/6/151/2013/http://file//localhost(null)papers3://publication/doi/10.5194/amt-6-151-2013).
- Krizhevsky, B. A. et al. (2012). “ImageNet Classification with Deep Convolutional Neural Networks”. In: *Communications of the ACM* 60.6, pp. 84–90.
- Kumar, S. et al. (2020). “Deep remote sensing methods for methane detection in overhead hyperspectral imagery”. In: *Proceedings - 2020 IEEE Winter Conference on Applications of Computer Vision, WACV 2020*, pp. 1765–1774. DOI: 10.1109/WACV45572.2020.9093600.
- Kuze, A. et al. (2009). “Thermal and near infrared sensor for carbon observation Fourier-transform spectrometer on the Greenhouse Gases Observing Satellite for greenhouse gases monitoring”. In: *Applied Optics* 48.35, pp. 6716–6733. ISSN: 15394522. DOI: 10.1364/AO.48.006716.

- Lavoie, T. N. et al. (2015). “Aircraft-Based Measurements of Point Source Methane Emissions in the Barnett Shale Basin”. In: *Environmental Science and Technology* 49.13, pp. 7904–7913. ISSN: 15205851. DOI: 10.1021/acs.est.5b00410.
- Matheou, G. and K. W. Bowman (2016). “A recycling method for the large-eddy simulation of plumes in the atmospheric boundary layer”. In: *Environmental Fluid Mechanics* 16.1, pp. 69–85. ISSN: 15731510. DOI: 10.1007/s10652-015-9413-4.
- Matheou, G. et al. (2014). “Large-Eddy Simulation of Stratified Turbulence. Part II: Application of the Stretched-Vortex Model to the Atmospheric Boundary Layer”. In: *Journal of the Atmospheric Sciences* 71.12, pp. 4439–4460. ISSN: 0022-4928. DOI: 10.1175/JAS-D-13-0306.1. URL: <http://journals.ametsoc.org/doi/abs/10.1175/JAS-D-13-0306.1>.
- Meerdink, S. K. et al. (2019). “The ECOSTRESS spectral library version 1.0”. In: *Remote Sensing of Environment* 230, p. 111196. ISSN: 0034-4257. DOI: <https://doi.org/10.1016/j.rse.2019.05.015>. URL: <https://www.sciencedirect.com/science/article/pii/S0034425719302081>.
- Meftah, M. et al. (2018). “SOLAR-ISS: A new reference spectrum based on SOLAR/SOLSPEC observations”. In: *A&A* 611, A1. DOI: 10.1051/0004-6361/201731316. URL: <https://doi.org/10.1051/0004-6361/201731316>.
- Montzka, S. A. et al. (2011a). “Non-CO₂ greenhouse gases and climate change”. In: ISSN: 00280836. DOI: 10.1038/nature10322.
- Montzka, S. A. et al. (2011b). “Small Interannual Variability of”. In: *Science* 331.January, pp. 67–69.
- Nassar, R. et al. (2017). “Quantifying CO₂ Emissions From Individual Power Plants From Space”. In: *Geophysical Research Letters* 44.19, pp. 10,045–10,053. ISSN: 19448007. DOI: 10.1002/2017GL074702.
- Nisbet, E. G. et al. (2019). “Very Strong Atmospheric Methane Growth in the 4 Years 2014–2017: Implications for the Paris Agreement”. In: *Global Biogeochemical Cycles* 33.3, pp. 318–342. DOI: <https://doi.org/10.1029/2018GB006009>. eprint: <https://agupubs.onlinelibrary.wiley.com/doi/pdf/10.1029/2018GB006009>. URL: <https://agupubs.onlinelibrary.wiley.com/doi/abs/10.1029/2018GB006009>.
- Pan, H. et al. (2020). “Computationally efficient wildfire detection method using a deep convolutional network pruned via fourier analysis”. In: *Sensors (Switzerland)* 20.10. ISSN: 14248220. DOI: 10.3390/s20102891.
- Parker, R. J. et al. (2015). “Assessing 5 years of GOSAT Proxy XCH₄ data and associated uncertainties”. In: *Atmospheric Measurement Techniques* 8.11, pp. 4785–4801. ISSN: 18678548. DOI: 10.5194/amt-8-4785-2015.

- Parker, R. et al. (2011). “Methane observations from the Greenhouse Gases Observing SATellite: Comparison to ground-based TCCON data and model calculations”. In: *Geophysical Research Letters* 38.15, p. L15807. URL: <http://dx.doi.org/10.1029/2011GL047871>[http://file://localhost\(null\)papers3://publication/uuid/825B7A52-ADA2-433B-B3AC-E5018E410E8B](http://file://localhost(null)papers3://publication/uuid/825B7A52-ADA2-433B-B3AC-E5018E410E8B).
- Pasquill, F (1961). “THE METEOROLOGICAL MAGAZINE”. In: *The Meteorological Magazine* 90.1063, pp. 33–49. ISSN: 0027-0644. DOI: 10.1175/1520-0493(1920)48<219e:tmm>2.0.co;2.
- Platt, U. and J. Stutz (2008). “Differential absorption spectroscopy”. In: *Differential Optical Absorption Spectroscopy*. Springer, pp. 135–174.
- Prather, M. J. et al. (2012). “Reactive greenhouse gas scenarios: Systematic exploration of uncertainties and the role of atmospheric chemistry”. In: *Geophysical Research Letters*. ISSN: 00948276. DOI: 10.1029/2012GL051440.
- Rayner, P. J. et al. (2014). “Constraining regional greenhouse gas emissions using geostationary concentration measurements : a theoretical study”. In: 2003, pp. 3285–3293. DOI: 10.5194/amt-7-3285-2014.
- Rienecker, M. M. et al. (2011). “MERRA: NASA’s Modern-Era Retrospective Analysis for Research and Applications”. In: *Journal of Climate* 24(14), pp. 3624–3648.
- Rigby, M. et al. (2017). “Role of atmospheric oxidation in recent methane growth”. In: *Proceedings of the National Academy of Sciences of the United States of America* 114.21, pp. 5373–5377. ISSN: 10916490. DOI: 10.1073/pnas.1616426114.
- Rodgers, C. D. (2000). *Inverse Methods for Atmospheric Sounding*. WORLD SCIENTIFIC. DOI: 10.1142/3171. eprint: <https://www.worldscientific.com/doi/pdf/10.1142/3171>. URL: <https://www.worldscientific.com/doi/abs/10.1142/3171>.
- Saunio, M. et al. (2016). “The global methane budget 2000-2012”. In: *Earth System Science Data* 8.2. ISSN: 18663516. DOI: 10.5194/essd-8-697-2016.
- Saunio, M. et al. (2020). “The global methane budget 2000-2017”. In: *Earth System Science Data*. ISSN: 18663516. DOI: 10.5194/essd-12-1561-2020.
- Schwandner, F. M. et al. (2017). “carbon dioxide sources”. In: *Science* 358.6360, p. 6360. DOI: 10.1126/science.aam5782.
- Sciences, E. National Academies of and Medicine (2018). “Thriving on Our Changing Planet: A Decadal Strategy for Earth Observation from Space.” In: *The National Academies Press*. DOI: 10.17226/24938.
- Shindell, D. et al. (2012). “Simultaneously mitigating near-term climate change and improving human health and food security”. In: *Science* 335.6065, pp. 183–189. ISSN: 10959203. DOI: 10.1126/science.1210026.

- Simonyan, K. and A. Zisserman (2015). “Very deep convolutional networks for large-scale image recognition”. In: *3rd International Conference on Learning Representations, ICLR 2015 - Conference Track Proceedings*, pp. 1–14. arXiv: 1409.1556.
- Stocker, T. et al. (2013). “Climate Change 2013: The Physical Science Basis. Contribution of Working Group I to the Fifth Assessment Report of the Intergovernmental Panel on Climate Change”. In: 1–30. DOI: 10.1017/CB09781107415324.004. URL: www.climatechange2013.org.
- Strandgren, J. et al. (2020). “Towards spaceborne monitoring of localized CO₂ emissions: an instrument concept and first performance assessment”. In: *Atmospheric Measurement Techniques* 13.6, pp. 2887–2904. DOI: 10.5194/amt-13-2887-2020. URL: <https://amt.copernicus.org/articles/13/2887/2020/>.
- Sutton, O. (1931). “A Theory of Eddy Diffusion the Atmosphere.” In: *Proceedings of the Royal Society A* 215.1915, pp. 143–165.
- Szegedy, C. et al. (2014). “Rethinking the Inception Architecture for Computer Vision”. In: *CoRR* abs/1512.00567. arXiv: arXiv:1512.00567v3.
- Thompson, D. et al. (2015). “Real-time remote detection and measurement for airborne imaging spectroscopy: A case study with methane”. In: *Atmospheric Measurement Techniques* 8.10. ISSN: 18678548. DOI: 10.5194/amt-8-4383-2015.
- Thorpe, A. K. et al. (2014). “Retrieval techniques for airborne imaging of methane concentrations using high spatial and moderate spectral resolution: Application to AVIRIS”. In: *Atmospheric Measurement Techniques* 7.2, pp. 491–506. ISSN: 18671381. DOI: 10.5194/amt-7-491-2014.
- Thorpe, A. et al. (2016). “The Airborne Methane Plume Spectrometer (AMPS): Quantitative imaging of methane plumes in real time”. In: *IEEE Aerospace Conference Proceedings*. Vol. 2016-June. ISBN: 9781467376761. DOI: 10.1109/AERO.2016.7500756.
- Thorpe, A. K. et al. (2017). “Airborne DOAS retrievals of methane, carbon dioxide, and water vapor concentrations at high spatial resolution: Application to AVIRIS-NG”. In: *Atmospheric Measurement Techniques* 10.10, pp. 3833–3850. ISSN: 18678548. DOI: 10.5194/amt-10-3833-2017.
- Toon, G. C. (2015). *Solar Line List for the TCCON 2014 Data Release*. en. DOI: 10.14291/TCCON.GGG2014.SOLAR.R0/1221658. URL: <https://data.caltech.edu/records/251>.
- Tratt, D. M. et al. (2014). “Airborne visualization and quantification of discrete methane sources in the environment”. In: *Remote Sensing of Environment* 154.1, pp. 74–88. ISSN: 00344257. DOI: 10.1016/j.rse.2014.08.011. URL: <http://dx.doi.org/10.1016/j.rse.2014.08.011>.

- Turner, A. J. et al. (2015). “Estimating global and North American methane emissions with high spatial resolution using GOSAT satellite data”. In: *Atmospheric Chemistry and Physics* 15.12, pp. 7049–7069. ISSN: 16807324. DOI: 10.5194/acp-15-7049-2015.
- Turner, A. J. et al. (2017). “Ambiguity in the causes for decadal trends in atmospheric methane and hydroxyl”. In: 114.21, pp. 5367–5372. DOI: 10.1073/pnas.1616020114.
- Turner, A. J. et al. (2019). “Interpreting contemporary trends in atmospheric methane”. In: *Proceedings of the National Academy of Sciences of the United States of America* 116.8, pp. 2805–2813. ISSN: 10916490. DOI: 10.1073/pnas.1814297116.
- Varon, D. J. et al. (2018). “Quantifying methane point sources from fine-scale satellite observations of atmospheric methane plumes”. In: *Atmospheric Measurement Techniques* 11.10, pp. 5673–5686. ISSN: 18678548. DOI: 10.5194/amt-11-5673-2018.
- Wang, J. et al. (2020). “Machine vision for natural gas methane emissions detection using an infrared camera”. In: *Applied Energy* 257. September 2019, p. 113998. ISSN: 03062619. DOI: 10.1016/j.apenergy.2019.113998. URL: <https://doi.org/10.1016/j.apenergy.2019.113998>.
- Wulder, M. A. et al. (2019). “Current status of Landsat program, science, and applications”. In: *Remote Sensing of Environment* 225, pp. 127–147. ISSN: 0034-4257. DOI: <https://doi.org/10.1016/j.rse.2019.02.015>. URL: <https://www.sciencedirect.com/science/article/pii/S0034425719300707>.